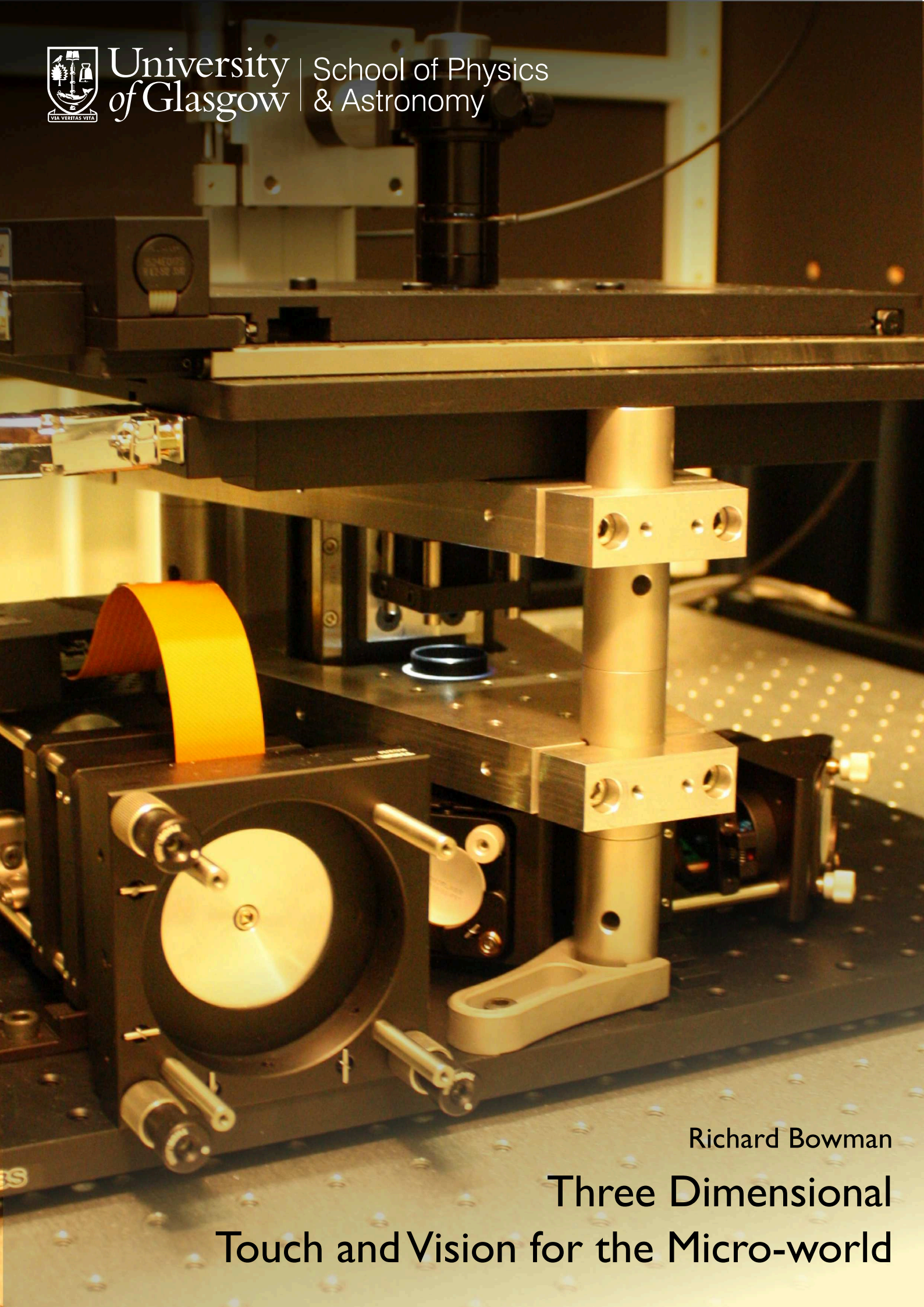




University of Glasgow | School of Physics & Astronomy



Richard Bowman

Three Dimensional Touch and Vision for the Micro-world



University
of Glasgow | School of Physics
& Astronomy

Three dimensional touch and vision for the micro-world

Richard W. Bowman

Thesis submitted in fulfilment of the
requirements for the degree of Ph.D.

School of Physics and Astronomy
University of Glasgow
G12 8QQ, UK

October 12, 2012

Acknowledgements

This thesis would not have come into being were it not for the help and support of many wonderful people. Firstly I would like to thank my supervisor, Miles Padgett, for years of sage advice, knowing when to let me keep playing, and teaching me how to check my H-index. I'd also like to thank my second supervisor at the Institute of Photonics, Amanda Wright, for her guidance and support, and for introducing me to biology. The members of the Optics group past and present, have taught me much, endured many enthusiastic but silly questions, and made our corner of the basement a very fun place indeed. Thanks go to Johannes for talking physics whilst running up hills, Jonathan for teaching me never to forget the Jaffa cakes, Martin for many enjoyable arguments, Graham for giving me my first balldriver, Maria for excellent cake, Arran for introducing us to ThorLabs, and Mike for admitting that a great many things aren't his field.

There are a few students and postdocs with whom I have worked particularly closely, and who have contributed to the work set out in the forthcoming chapters. Graham Gibson has taught me a great deal about how to build robust, stable optomechanics, and has assisted in the building of many of the experimental set-ups used during my PhD. His ability to take my designs from Blu-Tac prototype to nicely machined product has been invaluable when transferring technology outside of our lab. Graham was also involved along with me in the development and transfer of camera particle tracking software to Elliot Scientific. Daryl Preece passed the torch (and, indeed, the laser) to me at the end of his PhD, and worked together with me on the initial, 2D

implementation of closed-loop control described in Chapter 3. Finally, the force-feedback interface described in Chapter 7 was developed in collaboration with Cecile Pacoret, then a PhD candidate at CEA-LIST, Paris. Full details of the extent of collaborative work are given in the acknowledgements section of each of these chapters.

Other than the contributions outlined above, this thesis is my own work. Much of the work herein has been published in journal articles with multiple authors. While my co-authors provided valuable help and advice in carrying out the experiments and writing the paper, I was responsible for performing the experiments and the written material in this dissertation is entirely my own.

Finally, there are many people outside of the Optics group to whom I owe a debt of gratitude. My parents have encouraged and inspired my scientific endeavours ever since they bought me my first Lego set, and their steadfast support means the world to me. My friends in Glasgow and further afield have endured a great many hours of me talking shop, and somehow always managed to appear interested. Last but certainly not least, there is Kerrie. Listening ear, friendly biologist and chief proofreader, you have been invaluable to the completion of this dissertation, and your love and understanding have kept me smiling throughout.



Abstract

The ability to observe at tiny length scales has enabled key advances across the physical and life sciences. Much of what we know about the structure of cells and tissues comes from experiments on the micron length scale, enabled by new microscopy techniques. Modern manufacturing is increasingly concerned with materials that are structured on the nanometre scale, and devices which have ever-smaller features. Manipulating and measuring microscopic objects is a problem common to fields as diverse as microfabrication and cell biology, and it is these challenges that my doctoral studies have addressed.

Tiny sizes mean tiny forces; so small that the light from a laser can be used to propel objects. Optical tweezers, a technique pioneered some two and a half decades ago, exploit light's momentum to trap and manipulate objects. Now an established tool, single particles can be trapped and tracked to measure forces on a molecular scale, and this work is responsible for much of our current knowledge of motor proteins. This thesis describes advances in the holographic technology used to control multiple optical traps (and hence many trapped particles), as well as a new microscopy technique which enables fast 3D position measurement of many particles using a camera. Together, these improvements have enabled a number of experiments performed by myself and other members of the Glasgow Optics group. This is an important step towards using microscopic tools to work with nanometric objects, which would allow one to map out tiny structures on cell surfaces or assemble devices piece by piece.

Optical traps act as Hookean springs. Thus, if we measure the displace-

ment of a trapped object, we can find the force exerted by the optical trap. The custom stereomicroscope described in Chapter 2 generates two images of the sample from different viewpoints. 2D tracking of particles in each of the stereo images gives 3D positions for each particle. This takes less than 200 μs per image pair, and yields an accuracy of around 2 nm over a 10 μm axial range. The principal motivation for stereoscopic particle tracking is the ability to work with multiple particles—each object can be tracked simultaneously in 3D as they are manipulated by the optical tweezers. Aside from accurate particle tracking, the images can also be relayed to the operator via a stereoscopic display, allowing perception of objects' 3D positions.

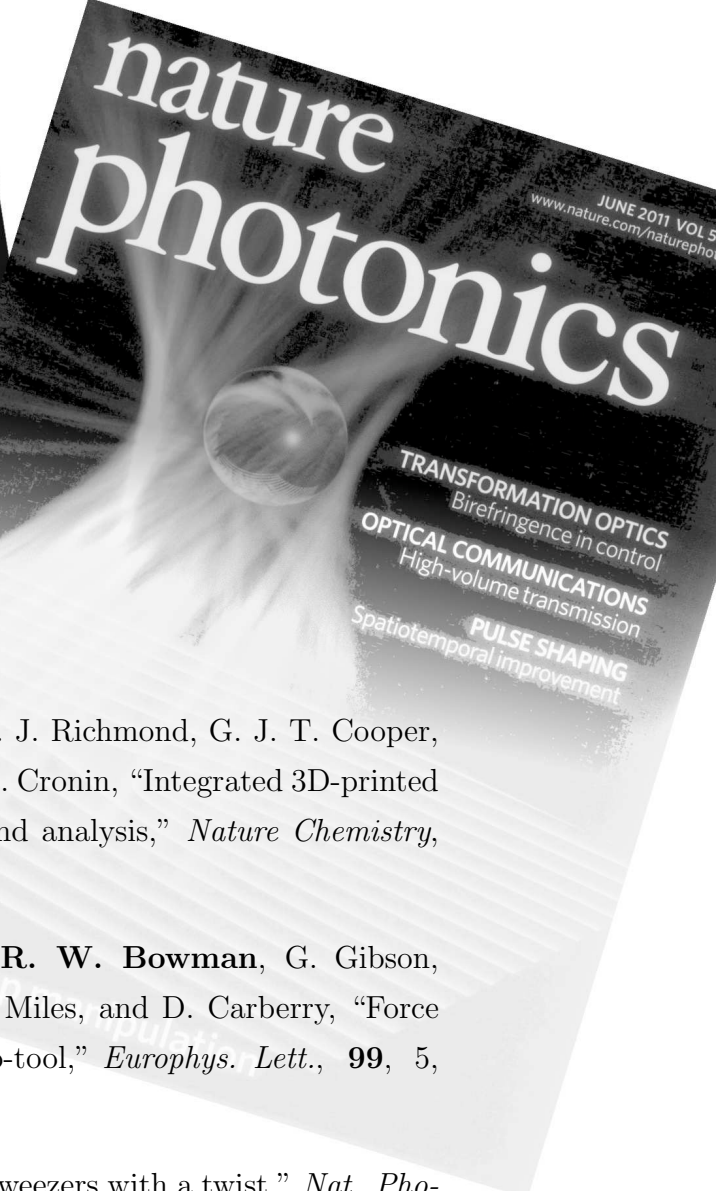
Holographic Optical Tweezers (HOT) use a reconfigurable diffractive optical element, a Spatial Light Modulator (SLM), to dynamically reshape the laser beam. This can steer, defocus or split the laser beam to produce multiple optical traps in arbitrary 3D positions. The graphics card acceleration described in Chapter 3 speeds up the rate at which we can control an SLM by several orders of magnitude. Faster control makes it possible to react to a particle's Brownian motion, and create a stiffer optical trap by dynamically updating the trap position to exert maximum force on the trapped object. I have used closed-loop control to reduce the axial and lateral Brownian fluctuations of a particle in an optical trap. Using a dual-beam trap (which has a greater working distance and field of view, at the expense of very low axial stiffness) I have decreased the range of axial motion from around 1 μm to 50 nm in Chapter 6. This increase in stiffness of over 300 times means the residual Brownian motion is not dissimilar to the fluctuations one finds in single-beam optical traps. This makes counterpropagating traps an interesting and viable option for manipulating extended objects such as micro-tools and biological samples.

Active feedback is one method by which the “stiffness” of an optical trap, or ensemble of traps, might be altered. However, it is also possible to use a structured light field to tune this property. Chapter 5 puts forward changes to the beam shape as a candidate for tailoring the stiffness of an optical trap.

By shaping the light field of the optical trap using an SLM, I have increased the axial stiffness of an optical trap such that, instead of being much weaker in the axial direction, the trap becomes nearly isotropic. Engineering light fields with SLMs is a very powerful technique, and Chapter 4 also describes its use to cancel out imperfections in the optical system. In fact, it was possible to use the SLM as a wavefront sensor to recover the pattern that, when displayed on the SLM, would cancel out the aberrations and restore the optical traps to optimal performance.

Sophisticated manipulation technologies are only useful if they can be effectively controlled, and consequently I have developed a number of improved interfaces to gain more control over the trapped particles. Chapter 7 describes a tactile interface, which restores the sensation of touch when dealing with the counterintuitive dynamics of the micro-world. I have also developed a custom multi-touch interface using an Apple iPad (described in the same chapter). This gives full control of multiple particles in 3D, and is simple and convenient enough to be used while adjusting the microscope or operating other equipment at the same time.

Overall, this work describes a number of technologies which have been enhanced to enable fast, 3D trapping and tracking of beads and multi-part probes. By creating simple, reliable systems and coupling them to an intuitive interface, I have endeavoured to produce developments which are of use to the non specialist as well as to experts in optical tweezers—a number of which are now available commercially (Section 8.7). These technologies form the basis of a toolkit for working with multi-part probes in optical tweezers, and they should bear fruit in the coming years as a new form of scanning-probe microscopy emerges.



Publications

- M. D. Symes, P. J. Kitson, J. Yan, C. J. Richmond, G. J. T. Cooper, **R. W. Bowman**, T. Vilbrandt, and L. Cronin, “Integrated 3D-printed reactionware for chemical synthesis and analysis,” *Nature Chemistry*, **4**, 5, 349–354, 2012.
- D. Phillips, S. Simpson, J. Grieve, **R. W. Bowman**, G. Gibson, M. Padgett, J. Rarity, S. Hanna, M. Miles, and D. Carberry, “Force sensing with a shaped dielectric micro-tool,” *Europhys. Lett.*, **99**, 5, 58004, 2012.
- M. Padgett and **R. W. Bowman**, “Tweezers with a twist,” *Nat. Photon.*, **5**, 6, 343–348, 2011.
- **R. W. Bowman**, N. Muller, X. Zambrana-Puyalto, O. Jedrkiewicz, P. Di Trapani, and M. J. Padgett, “Efficient generation of bessel beam arrays by means of an slm,” *Eur. Phys. J. – Special Topics*, **199**, 1, 159–166, 2011.
- **R. W. Bowman**, V. D’Ambrosio, E. Rubino, O. Jedrkiewicz, P. Di Trapani, and M. J. Padgett, “Optimisation of a low cost SLM for diffraction efficiency and ghost order suppression,” *Eur. Phys. J. – Special Topics*, **199**, 1, 149–158, 2011.
- **R. W. Bowman**, G. Thalhammer, A. Jesacher, G. Gibson, M. Ritsch-Marte, and M. J. Padgett, “Position clamping in a counterpropagating holographic optical trap,” *Opt. Express*, **19**, 10, 9915–9922, 2011.

- **R. W. Bowman**, G. Gibson, D. Carberry, L. Picco, M. Miles, and M. J. Padgett, “iTweezers: optical micromanipulation controlled by an Apple iPad,” *J. Optics*, **13**, 4, 044002, 2011.
- **R. W. Bowman**, D. Preece, G. Gibson, and M. J. Padgett, “Stereoscopic particle tracking for 3D touch, vision and closed-loop control in optical tweezers.” *J. Opt. A*, **13**, 4, 044003, 2011.
- M. Dienerowitz, G. M. Gibson, **R. W. Bowman**, and M. J. Padgett, “Holographic aberration correction: optimising the stiffness of an optical trap deep in the sample,” *Opt. Express*, **19**, 24 589–24 595, 2011.
- D. B. Phillips, J. A. Grieve, S. N. Olof, S. J. Kocher, **R. W. Bowman**, M. J. Padgett, M. J. Miles, and D. M. Carberry, “Surface imaging using holographic optical tweezers,” *Nanotechnol.*, **22**, 285503, 2011.
- D. B. Phillips, D. M. Carberry, S. H. Simpson, H. Schaefer, M. Steinhart, **R. W. Bowman**, G. M. Gibson, M. J. Padgett, S. Hanna, and M. J. Miles, “Optimizing the optical trapping stiffness of holographically trapped microrods using high-speed video tracking,” *J. Optics*, **13**, 4, 044023, 2011.
- D. B. Phillips, S. H. Simpson, J. A. Grieve, G. M. Gibson, **R. W. Bowman**, M. J. Padgett, M. J. Miles, and D. M. Carberry, “Position clamping of optically trapped microscopic non-spherical probes,” *Opt. Express*, **19**, 20 622–20 627, 2011.
- **R. W. Bowman**, A. J. Wright, and M. J. Padgett, “An SLM-based Shack–Hartmann wavefront sensor for aberration correction in optical tweezers,” *J. Optics*, **12**, 12, 124004, 2010.
- **R. W. Bowman**, G. Gibson, and M. Padgett, “Particle tracking stereomicroscopy in optical tweezers: Control of trap shape,” *Opt. Express*, **18**, 11, 11 785–11 790, 2010.

- **R. W. Bowman** and D. F. Buscher, “Low-cost capacitive sensing for precision alignment of mirrors,” *Meas. Sci. Technol.*, **21**, 5, 055201, 2010.
- C. Alpmann, **R. W. Bowman**, M. Woerdemann, M. J. Padgett, and C. Denz, “Mathieu beams as versatile light moulds for 3D micro particle assemblies,” *Opt. Express*, **18**, 25, 26 084–26 091, 2010.
- D. M. Carberry, S. H. Simpson, J. A. Grieve, Y. Wang, H. Schafer, M. Steinhart, **R. W. Bowman**, G. Gibson, M. J. Padgett, S. Hanna, and M. J. Miles, “Calibration of optically trapped nanotools,” *Nanotechnol.*, **21**, 17, 2010.
- A. Curran, A. M. Yao, G. Gibson, **R. W. Bowman**, J. Cooper, and M. J. Padgett, “Real time characterization of hydrodynamics in optically trapped networks of micro-particles,” *J. Biophotonics*, **3**, 4, 244–251, 2010.
- D. Preece, **R. W. Bowman**, A. Linnenberger, G. Gibson, S. Serati, and M. Padgett, “Increasing trap stiffness with position clamping in holographic optical tweezers,” *Opt. Express*, **17**, 25, 22 718–22 725, 2009. **Joint 1st authors**
- V. R. Daria, C. Stricker, **R. W. Bowman**, S. Redman, and H.-A. Bachor, “Arbitrary multisite two-photon excitation in four dimensions,” *Appl. Phys. Lett.*, **95**, 9, 093701, 2009.
- C. Pacoret, **R. W. Bowman**, G. Gibson, S. Haliyo, D. Carberry, A. Bergander, S. Regnier, and M. Padgett, “Touching the microworld with force-feedback optical tweezers,” *Opt. Express*, **17**, 12, 10 259–10 264, 2009. **Joint 1st authors**
- D. Preece, E. Yao, G. Gibson, **R. W. Bowman**, J. Leach, and M. Padgett, “A spatial light phase modulator with an effective resolution of 4 mega-pixels,” *J. Mod. Opt.*, **55**, 18, 2945–2951, 2008.

- D. Preece, S. Keen, E. Botvinick, **R. W. Bowman**, M. Padgett, and J. Leach, “Independent polarisation control of multiple optical traps,” *Opt. Express*, **16**, 20, 15 897–15 902, 2008.
- A. Bowman, E. Crawford, G. Alexander, and **R. W. Bowman**, “rpanel: Simple interactive controls for r functions using the tcltk package,” *J. Stat. Soft.*, **17**, 9, 2007.

Contents

1	Introduction	1
1.1	Optical forces	3
1.1.1	Non-conservative forces	6
1.1.2	Rayleigh scattering: very small particles	7
1.1.3	Mie scattering: intermediate sized particles	9
1.2	System designs for optical tweezers	9
1.2.1	Dual traps	10
1.2.2	Time-shared traps	11
1.2.3	Holographic optical tweezers	12
1.2.4	Laser sources	16
1.2.5	Objective lenses and beam shape	18
1.3	Counterpropagating optical traps	18
1.4	Force and position measurement	20
1.4.1	Laser position detection	21
1.4.2	Video particle tracking	24
1.4.3	Particle dynamics and calibration	28
1.5	Optically Actuated Tools	30
1.6	Discussion	32
2	Stereoscopic 3D particle tracking	34
2.1	Optical system	37
2.2	Image analysis	39
2.3	3D vision	42

<i>CONTENTS</i>	xi
2.4 Particle tracking accuracy	43
2.5 Discussion	45
3 Fast holographic control	49
3.1 GPU hologram calculation	51
3.2 Modelling a particle in a closed-loop trap	54
3.3 Experimental setup	57
3.4 Results	57
3.5 Discussion	61
4 Aberration correction	64
4.1 Hologram Design	66
4.2 Optical System	67
4.3 Results	68
4.4 Discussion	73
5 Trap shaping	75
5.1 Axial and lateral stiffness	76
5.2 Experimental results	79
5.3 Discussion	80
6 Counterpropagating holographic traps	83
6.1 Method	85
6.1.1 Optical System	85
6.1.2 Control Logic	86
6.2 Results	88
6.3 Discussion	90
7 Interface technology	93
7.1 Force feedback remote handling	94
7.1.1 Experimental configuration	97
7.1.2 Force feedback in 2D	100
7.1.3 Force feedback in 3D	101

7.2	Multi-touch micromanipulation	103
7.2.1	Implementation	104
7.2.2	Interactive hologram demo	105
7.2.3	Further interface improvements	106
7.3	Discussion	108
8	Conclusions	111
8.1	Stereoscopic tracking	112
8.2	Fast control	114
8.3	Aberration correction	116
8.4	Trap shaping	117
8.5	Counterpropagating traps	118
8.6	Interface technology	119
8.7	Commercialisation	120
8.8	Optically actuated tools	124
8.9	Conclusion	125



List of Figures

1.1	Illustration of an optical trap being used to measure the force exerted by a kinesin molecule walking along a microtubule. . .	2
1.2	A simple model of the gradient force resulting from a laser beam being focused through a small glass sphere. ►	4
1.3	An illustration of the “scattering force” due to a partially reflective particle in an optical trap. Some of the incident light is reflected, causing a force normally in the same direction as the incident light.	5
1.4	Beads circulating in a ring-shaped Laguerre-Gaussian laser beam.	7
1.5	Trap strength as a function of particle size, using Mie theory, ray optics and Rayleigh scattering.	8
1.6	The optical system for a single-beam gradient trap.	10
1.7	Beam steering and multiplexing techniques for movable and/or multiple optical traps.	11
1.8	Holograms displayed on an SLM can be used to shift the optical trap laterally (by emulating a prism), axially (by displaying a lens), or any combination of the two.	13
1.9	The Gerchberg-Saxton algorithm is an efficient way of producing optimised holograms for complicated patterns.	15
1.10	The optical absorption curve for water, overlaid with some common laser wavelengths.	17

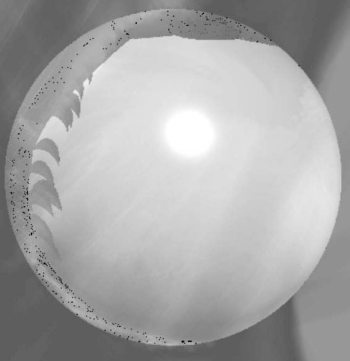
1.11	Different configurations for forming counterpropagating optical traps.	19
1.12	Quadrant photodiodes are an extremely sensitive way of measuring the position of a trapped object, by looking at the deflection of the beam.	22
1.13	Quadrant photodiodes can be used to measure axial displacement by exploiting the change in divergence of the beam.	23
1.14	A typical image of a 2 μm silica bead in an optical tweezers system and some methods of tracking it.	25
1.15	An x - z slice through the light scattered by a glass bead in a high-NA, bright field microscope.	26
1.16	A typical power spectrum, measured by video particle tracking. The mean squared displacement (right), shows the same information in the time domain.	29
1.17	An illustration of an optically actuated micro tool.	31
2.1	An illustration of stereoscopic imaging.	36
2.2	Outline of the imaging system used to produce stereo images.	38
2.3	Images of a 2 μm bead at different depths, before and after processing with a symmetry transform. ►	41
2.4	Frames from a red-blue anaglyphic video, showing a cube of 2 μm beads being tumbled in 3D using holographic optical tweezers. ►	43
2.5	Measures of particle tracking accuracy, as a fixed 3 μm bead is stepped axially.	44
2.6	Power Spectral Density of a 5 μm silica bead's position fluctuations in an optical trap.	45
3.1	Flowcharts of the hologram calculation algorithm, showing the memory required to calculate a hologram $w \times h$ pixels in size with N spots.	53
3.2	Experimental set-up and control flowchart for servocontrol.	58

3.3	Measured response time of a BNS XY series SLM.	59
3.4	Variance and PSD of a trapped bead's motion for different feedback gains.	60
3.5	Three 5 μm beads in optical traps showing variance and PSD of their motion with and without feedback.	61
3.6	Scatterplots of a 5 μm silica bead's position fluctuations with and without position clamping.	62
4.1	Schematic of the SLM-based Shack-Hartmann sensor.	66
4.2	The optical system used in the experiment.	67
4.3	Images of the Shack-Hartmann array reflected from a coverglass-air interface.	68
4.4	Images of the Shack-Hartmann array when a helical phase term is added to the SLM.	69
4.5	Images of the focal spot before and after correction.	70
4.6	Point spread function before and after aberration correction.	71
4.7	Scatterplots of an 800nm silica bead trapped in the laser focus with and without the correction applied.	71
4.8	Recovered Zernike coefficients when individual Zernike modes are deliberately added to the system, and signal-to-noise ratio for different severities of aberration.	72
5.1	Placing different apertures in the back focal plane of the microscope objective can change the trap properties.	77
5.2	Stiffness of an optical trap for a 5 μm silica bead created with various apertures at the back focal plane of the microscope objective.	78
5.3	Stiffness of an optical trap with various apertures, for (a) a 2 μm silica particle, (b) a 3 μm silica particle, (c) a 5 μm polystyrene particle.	79
5.4	Position histograms for three beads trapped with different apertures, showing different axial stiffnesses.	80

5.5	An optically trapped paddle wheel, fabricated by two photon polymerisation and driven using the scattering force	81
6.1	Schematic of the trapping and imaging system for creating counterpropagating optical traps with a single objective	84
6.2	The sample cell and optical system used to implement closed loop control in the “macro-tweezers” geometry.	87
6.3	A scatterplot and power spectra of the motion of a 10 μm silica particle in the trap with and without feedback.	88
6.4	Response of a 10 μm bead to a square-wave control signal, with and without feedback. ►	90
6.5	Three 10 μm beads simultaneously clamped in 3D, with scatterplots of their position.	91
7.1	Scaling factors between the microworld and the macroworld and the distortion of dynamic parameters which follows by dimensional analysis.	94
7.2	Schematic of the control system for force feedback in optical tweezers.	96
7.3	Initial optical set-up used for force feedback control, using a second camera where the trap is always centred in the image.	98
7.4	Example tasks performed with the haptic interface, showing the forces experienced by the user. ►	99
7.5	Left and right stereo images of a 5 μm bead rolled up the surface of an oil droplet. ►	101
7.6	Measured force and position data as a 3 μm silica bead was pressed against the coverslip.	102
7.7	The iTweezers interface as shown to the user. ►	104
7.8	Screenshots of the interface being used to generate holograms on the iPad GPU, downloadable from the iTunes store as “iHologram”.	106

7.9	A task used to assess the effectiveness of vibrotactile feedback in iTweezers.	107
8.1	The stereoscopic imaging system, packaged to fit a Zeiss inverted microscope, along with an improved, 3D printed mount.	113
8.2	Piezoelectric nanomanipulators developed by Kelindiek Nanotechnik GmbH along with the tablet interface I developed, based on iTweezers. ►	120
8.3	The “Cube”, a portable optical tweezers instrument which incorporates many of the techniques described in this thesis. . .	122
8.4	A microscopic tool, fabricated using two-photon polymerisation, imaged on the Cube tweezers system.	125

► denotes figures that have associated videos, which are included on the disc enclosed with this thesis. Where possible, PDF hyperlinks to published videos have been included in figure captions, along with a reference to the journal article.



Chapter 1

Introduction

Light is often used to transfer energy to microscopic systems, whether it is exciting a fluorophore or changing the conformational state of a photoactivated molecule. However, the momentum of light can also play an important role in experiments across the physical and life sciences. Optical tweezers exploit this to perform very sensitive force measurements and delicate manipulations. Over the four decades since Ashkin's seminal paper [1], optical micromanipulation has developed from qualitative physics experiments to provide precise tools that can be used to manipulate and measure forces and displacements on the single-molecule level.

Working at micron length scales introduces us to many challenges, not least of which is the very different nature of forces. Macroscopic motion is governed by inertia and gravity, whereas the microscopic world is ruled by viscosity and Brownian motion [4, 5]. This is the result of scaling laws; mass decreases linearly with volume, but drag is more closely related to area [6].

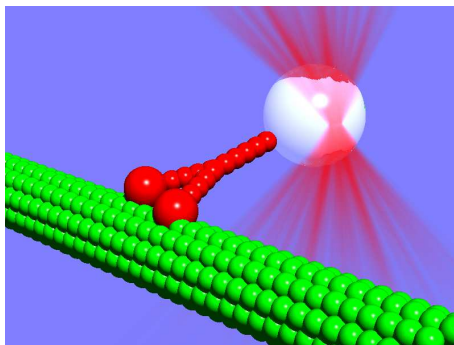


Figure 1.1: Illustration of an optical trap being used to measure the force exerted by a kinesin molecule walking along a microtubule, as done in [2,3].

Both forces decrease as we move to smaller length scales, but inertial forces decrease more quickly. Manipulation of objects small enough to inhabit a microscope slide consequently requires very little force, so even the momentum carried by a laser beam is enough to move them.

The simplest model of an optical trap is a spring, where a trapped particle feels a force pulling it back towards the trap centre. This force increases linearly with its distance from the equilibrium point. This enables optical tweezers to make sensitive force measurements, detecting forces 1000 times smaller than those accessible with Atomic Force Microscopes (AFMs). Instead of a mechanical cantilever, the spring in optical tweezers is made of light. An optical spring confers two main benefits: firstly, it is several orders of magnitude softer than an AFM cantilever, and secondly there is no requirement to have mechanical access to the sample, meaning that closed sample cells can be used. This soft spring has enabled groundbreaking experiments on single molecules, such as measuring the step sizes and forces exerted by single molecular motors such as kinesins [2] and myosins [3]. The elasticity and hence conformational properties of DNA have also been probed with this technique [7].

Optical tweezers are formed with a focused laser beam, which is deflected by the particle [8]. It is this deflection of the light that gives rise to the forces applied to trapped objects, which can range in size from a few

nanometres [9,10] to tens or hundreds of microns [11]. A microscope objective is usually used to focus the laser beam onto the sample, and thus optical tweezers are generally combined with optical microscopy (tweezers systems are often based around a high-magnification microscope). This introductory chapter describes the optical systems used, the forces exerted, and some of the applications of optical tweezers.

My doctoral work has comprised a number of improvements to the technology of optical tweezers, most significantly the position and force measurement technique described in Chapter 2 and faster control of the optical traps as set out in Chapter 3. While these techniques are applicable to many measurement and manipulation experiments, I have developed them in the context of working with optically actuated micro-tools as described in Section 1.5, using holographic optical tweezers.

1.1 Optical forces

Precise modelling of the forces and torques exerted by optical tweezers is most often done using Generalised Lorentz-Mie theory, however the simple ray-optical model (strictly valid only for the largest particles used in optical tweezers) [12] provides an excellent qualitative insight into the physics underlying optical tweezers. Fundamentally, optical tweezers function because of the momentum of light. As light passes through a trapped particle, its direction, and hence its momentum, is changed by the particle. This means that the light exerts a force on the particle, which (for particles that are stably trapped) acts to move it back towards the laser focus. The simple ray-optical model of light focused through a sphere tells us that the light's direction is unchanged when the sphere is precisely at the laser focus, as illustrated in Figure 1.2. When the bead is laterally displaced from the focus, it deflects the laser beam in the same direction, resulting in a force that draws it back to the optical axis. Similarly, when the bead is displaced axially it changes the divergence of the laser beam. As we must sum over the whole beam to

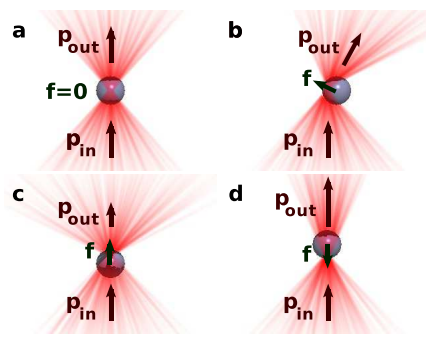


Figure 1.2: A simple model of the gradient force resulting from a laser beam being focused through a small glass sphere. As the sphere is displaced from the focal point, it bends the light, changing its momentum. This in turn exerts a force on the particle. The laser is propagating upwards in each figure. Video on enclosed disc.

find its momentum, a beam with lower divergence will have a higher overall momentum than a beam with high divergence. Thus, if the particle moves behind the focus (and decreases the divergence of the light exiting the trap), it has increased the momentum of the light in the axial direction and hence feels a force pushing it back towards the focus [13]. Borrowing a term from Rayleigh scattering theory, this force is often referred to as the “gradient” force as it moves the particle up the intensity gradient, towards the point of maximum intensity (the laser focus).

To complete our qualitative picture of the forces, we must take into account that the bead will not perfectly refract the light; some of it will be absorbed and some reflected. This results in a small but significant force pushing the particle in the direction of propagation of the laser beam, often referred to as the “scattering” force, illustrated in Figure 1.3. For this reason, the equilibrium position of beads in a trap does not place the centre of the particle on the centre of the focus, rather the particle sits behind this position (i.e. further along the direction of propagation of the laser). This is also the reason we need to use a tightly focused beam for a single-beam trap: were it not for the axial restoring force, the particle would be moved

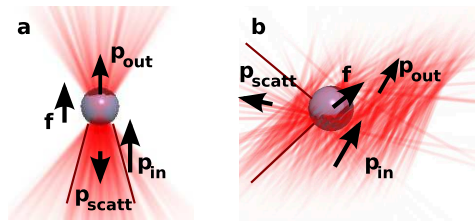


Figure 1.3: An illustration of the “scattering force” due to a partially reflective particle in an optical trap. Some of the incident light is reflected, causing a force normally in the same direction as the incident light. This displaces the equilibrium position of a bead in an optical trap axially, so it is held slightly behind the focus (left). Extended optical traps, such as line traps (right), can cause particles to move along the bright region due to the scattering force.

onto the beam axis then simply pushed along the direction of propagation of the laser. In fact, our qualitative model can go further, demonstrating that the maximum force we can exert pulling a particle against the direction of propagation is limited by the divergence of the light entering the particle. The maximum possible axial momentum the light can have on exiting the particle is reached when the beam is fully collimated, i.e. the angle of the cone of light is close to zero. If we use a more weakly focused beam, it has a higher axial momentum before entering the particle. Even if the particle fully collimates the light, the axial momentum cannot increase by a large amount, and consequently we can reach only very small axial forces. The point where the gradient force can overcome the scattering force to create a stable trap in 3D varies depending on the size and type of particle being trapped, but it is typically at a high Numerical Aperture (NA), usually greater than one when working in water. It is worth noting that this corresponds to a cone angle much higher than that depicted in Figure 1.2, often exceeding 130° .

Shaping the beam used to generate the optical traps allows some of these forces to be tuned: for example, ring-shaped beams [14, 15] can increase axial stiffness by effectively increasing the divergence of the beam before

the particle (if we block out the centre portion of the beam, more of the light is propagating at higher angles to the optical axis, and hence its axial momentum is lower). Laguerre-Gaussian beams focus to a ring-shaped spot, which can also increase the axial stiffness of an optical trap by concentrating more of the light at the edges of the particle. Shaping the beam to change the trap's stiffness is discussed further in Chapter 5.

1.1.1 Non-conservative forces

The gradient force corresponds to a ready-made “potential”, that of the intensity of the laser beam. Even in the case of larger particles, what we refer to as the gradient force will not transfer energy to a particle provided we look over a time interval where it starts and finishes in the same place. However, the scattering force is non-conservative, meaning that it can transfer energy. For example, if a particle is pushed along the beam axis in the centre of the optical trap but then moves towards the edge of the beam (where the scattering force is weaker) and then moves in the opposite direction back to its starting point, the scattering force will have done work on the particle [16, 17]. This means that it is not strictly correct to define a potential for an optical trap where the scattering force is not zero. However, in most situations where optical traps are currently used, the non-conservative effects are sufficiently small not to have a great effect on force measurement [18]. One notable exception is when the trapping potential is extended, so the scattering force can be used to push particles along paths, often referred to as “optical guiding” [19, 20]. An excellent demonstration of non-conservative forces is that of particles circulating around a ring-shaped trap as shown in Figure 1.4, which has been used to study both the angular momentum of light and the colloidal dynamics of such a system [21, 22]. Optical tweezers were also instrumental in the experimental verification of the fluctuation theorem [23, 24], another non-equilibrium effect observed in small systems.

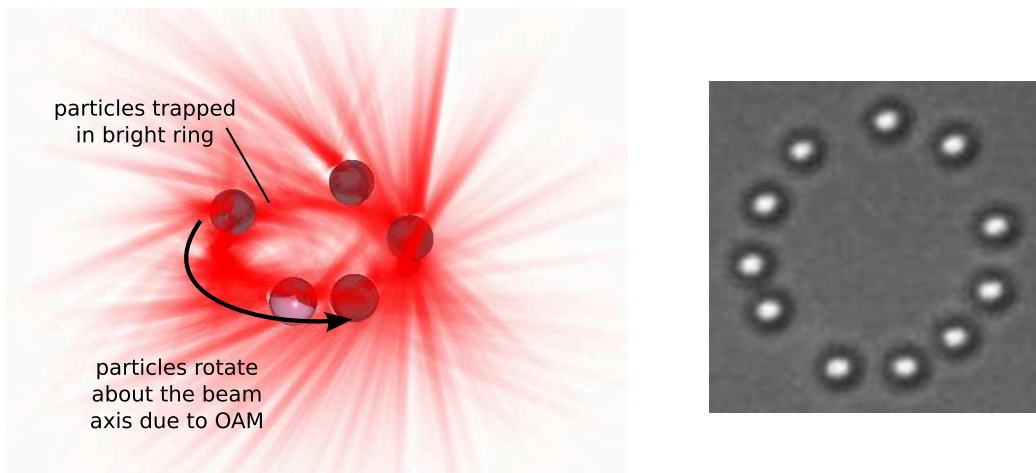


Figure 1.4: Beads circulating in a ring-shaped Laguerre-Gaussian laser beam, as used in the works by O’Neil [21] and Roichman [22] amongst others.

1.1.2 Rayleigh scattering: very small particles

For particles which are very much smaller than a wavelength of light, we can model their interaction with the electromagnetic field of the laser beam as a single induced dipole. This is the origin of the terms “gradient force” and “scattering force”, as the equations separate quite neatly into the two different forces. Placing a polarisable particle in an electric field will induce dipole moments throughout the particle, but in the case of a very small particle it is acceptable to model this as a single point dipole at the centre of the particle. As the electric field of the light is oscillating, the particle’s dipole moment also oscillates, and thus it re-radiates (or “scatters”) some of the light. This scattered light goes in all directions and not just the direction of the incident light, so its average momentum is zero as the different directions cancel out. This means the difference in momentum between incident and scattered light pushes it in the direction of the incident light, the “scattering force”. However, there is another effect at play—the interaction of an electric dipole with a gradient in the electric field. This acts to pull the particle towards the point of maximum intensity, the laser focus. The size of the induced dipole, and hence the magnitude of both gradient and scattering

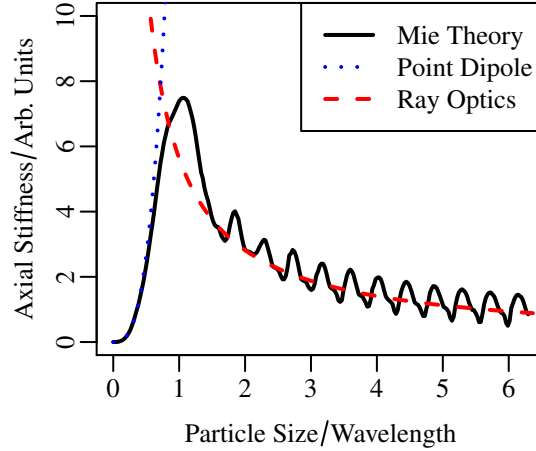


Figure 1.5: Trap strength as a function of particle size, using Mie theory, ray optics and Rayleigh scattering. Rayleigh scattering, where the particle is modelled as a point dipole, is valid for particle sizes much less than a wavelength and predicts stiffness varies as radius cubed. Ray optics is the opposite case, where stiffness is inversely proportional to radius, and is valid in the limit of large particles. Mie theory (and the various extensions to it) is an exact solution to Maxwell’s equations for the scattering of a plane wave by a sphere, and encompasses coherent effects such as resonances in addition to being valid for all particle sizes. Curves are reproduced from [26].

forces, depends not only on laser power but also on particle size. It increases very sharply with particle radius a , being proportional to volume, i.e. a^3 , for very small particles [9]. This is illustrated in Figure 1.5, where the cubic curve matches the exact Mie theory curve for particles much less than a wavelength in size. This model is sufficient for very small dielectric particles, however it is also possible to trap metal nanoparticles. In this case, plasmonic effects can lead to resonances and other effects not explained by a simple dipole model [25].

1.1.3 Mie scattering: intermediate sized particles

Ray-optical modelling of the forces is valid for particles much bigger than a wavelength of light (around $10\ \mu\text{m}$ or larger), however most particles used are smaller than this. Too small for ray optics and too large for approximation by a single dipole, these intermediate-sized particles are most often dealt with using a generalisation of Mie theory [13,26–29]. This is an analytic solution of Maxwell’s equations for a plane wave interacting with a dielectric sphere. It is often combined with T-matrix formalism (which uses a matrix to represent the relationship between input and output light fields) to make estimates of trap potentials and stiffness values for micron-sized particles [30,31]. Non-spherical particles, however, require more computationally demanding modelling such as finite-element simulations that solve Maxwell’s equations numerically [32].

1.2 System designs for optical tweezers

The single-beam gradient trap is a basic design pattern which has been refined and extended in many ways, however most systems have many elements in common. The essential feature of single beam optical tweezers is a high-NA objective lens, to create a small focal volume which is tightly localised in three dimensions. Modern microscopes generally produce an image at infinity, which means that we use a tube lens to bring the image into focus on the camera. This also means that projecting an optical trap is as simple as coupling a collimated laser beam into the back aperture of the objective, as shown in Figure 1.6.

Additional optics are typically needed to adjust the width of the laser beam, and to align it both in the sample and on the back aperture. If the spacing between each pair of lenses is equal to the sum of the focal lengths, tilting the beam in the Fourier plane shown in Figure 1.7 translates the focus in the sample without changing the direction of the cone of light entering the focal point, a condition known as “telecentric imaging”. This is necessary

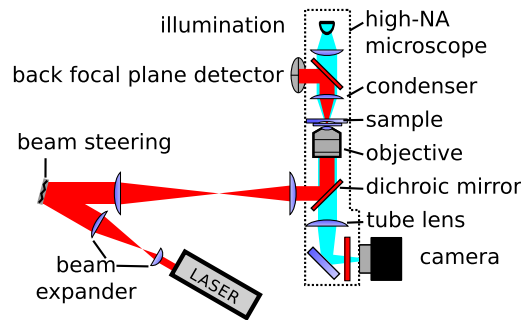


Figure 1.6: The optical system for a single-beam gradient trap. A laser beam is expanded with a telescope and then focused by a high-NA microscope. The location of beam steering optics and detection optics for back focal plane interferometry are shown. Fold mirrors and beamsplitters are omitted for clarity, but usually the system is arranged such that the microscope is vertical (often a commercial inverted microscope is used). The remainder of the optics can then be laid out on an optical breadboard.

for the trap properties (stiffness, etc.) to remain constant as the trap is moved around the sample, which is particularly important when making force measurements. Figure 1.7 shows a number of methods of moving an optical trap, ranging from a steerable mirror (for a single movable optical trap) to a Spatial Light Modulator (SLM) which can create multiple traps at arbitrary positions in 3D [33]. Besides their cost, the simpler beam steering designs (such as a single mirror or two mirrors and beamsplitters) are often favoured when forces are to be measured using an interferometric approach, which is complicated by the use of SLMs or Acousto-Optic Deflectors (AODs).

1.2.1 Dual traps

The simplest method for creating two optical traps is to divide and recombine the laser beam with two polarising beamsplitters, as shown in Figure 1.7. This gives rise to two orthogonally polarised traps which can be independently steered. However, any drift due to the laser will be common to both and this has been used to cancel out drift from sensitive force

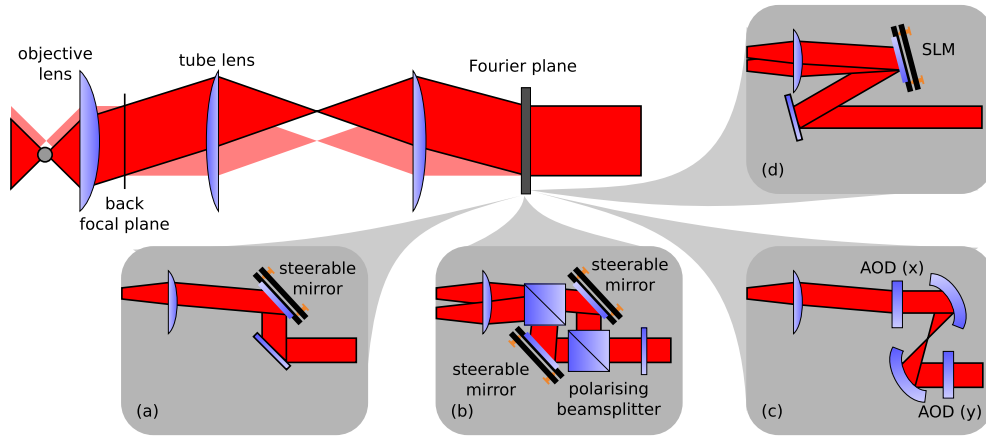


Figure 1.7: Beam steering and multiplexing techniques for movable and/or multiple optical traps: (a) steerable mirror in Fourier plane, (b) polarising beamsplitters and two steerable mirrors, (c) Acousto-Optic Deflectors (AODs) and (d) Spatial Light Modulator (SLM).

measurements [34, 35]. Such set-ups have been used to make sensitive measurements of biomolecules such as DNA [34], as well as to explore physical concepts in bistable traps [36].

1.2.2 Time-shared traps

When more than two optical traps are required, splitting and recombining the laser with beamsplitters becomes cumbersome and inefficient. A common way around this problem is to use either a scanning mirror or a pair of Acousto-Optic Deflectors (AODs) to move the trapping laser between a number of trap sites very rapidly [37]. If the laser is scanned much faster than the characteristic “corner frequency” of the optical traps¹ (i.e. the particles do not have time to diffuse away from the trap positions while the laser is elsewhere), the fluctuations are averaged out and the system behaves as if there were multiple traps. Multiple traps created in this way do not

¹The corner frequency ω_c is the nominal maximum frequency at which the particle responds to the trap—motion above this frequency is effectively free diffusion. This is discussed further in Section 1.4.3.

interfere with each other (as only one trap is present at any given instant), however they can only be scanned in 2D. More recently, multiple AODs have been used to create a scanning lens, allowing the focus to be shifted axially. This opens a number of exciting possibilities for 3D imaging, however its low optical efficiency means that this technique will need further development before it can become a viable optical trapping system [38].

1.2.3 Holographic optical tweezers

Holographic Optical Tweezers (HOT) use a computer-controlled optical element to modify the phase of a laser beam [33, 39, 40]. This allows great flexibility both in the number of traps created and in the shape of each trap. By using a Spatial Light Modulator (SLM) [41] to insert a hologram corresponding to the interference of several plane waves into the Fourier plane, a single beam can be multiplexed into multiple beams that produce an array of traps. However, the SLM also allows the beams to be defocused and hence the traps can be moved in three dimensions [42]. In fact, one can do much more than change the focus—it is possible to re-shape the beam to alter the trap characteristics (Chapter 5) or correct for aberrations (Chapter 4).

By tilting the laser beam in the Fourier plane, i.e. the back focal plane of the objective, it is possible to move the focal spot laterally. One way of achieving this would be to use a prism, however this is not easy to reconfigure. Alternatively, we can use a re-programmable liquid crystal display or Spatial Light Modulator (SLM) to modify the phase of the laser beam in the same way that a prism does, as shown in Figure 1.8. The phase shift from a prism is proportional to the thickness of the prism, however a phase shift of one full wavelength is equivalent to no phase shift at all. This means we can “wrap” the phase back to zero again, hence the periodic jumps from black (no phase shift) to white (one wavelength of retardation) in Figure 1.8.

It is also possible to display a virtual lens on the hologram, again having phase jumps every time the phase delay reaches a full wavelength. To shift the trap to an arbitrary position in 3D, we can combine the two phase shifts

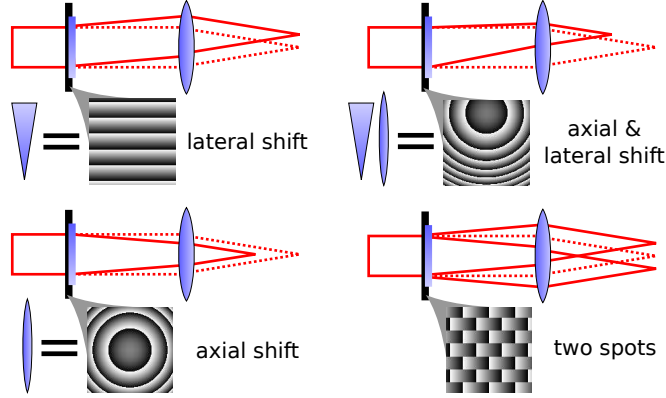


Figure 1.8: Holograms displayed on an SLM can be used to shift the optical trap laterally (by emulating a prism), axially (by displaying a lens), or any combination of the two. It is also possible to create multiple spots by displaying the interference pattern between the beams required to generate each individual spot.

simply by adding them, as shown in Figure 1.8. The phase shift required to move a trap to position x, y, z as a function of u and v , the vertical and horizontal positions on the hologram, is simply:

$$\phi_{xyz}(u, v) = \left(\frac{ku}{f}\right)x + \left(\frac{kv}{f}\right)y + \left(\frac{k(u^2 + v^2)}{2f^2}\right)z \quad \text{mod } 2\pi$$

where $k = 2\pi/\lambda$ is the wavenumber, f is the focal length of the Fourier transform lens after the SLM. The three terms correspond to shifts in the x , y and z directions respectively.

The simplest method of creating multiple spots is to calculate the hologram $\phi_i(u, v)$ for each spot, and then to sum the light fields resulting from this [43]. To do this, we represent each light field as a complex number having a uniform amplitude and a phase given by the hologram, such that the final hologram is:

$$\phi_{\text{total}} = \arg\left(\sum_i A_i \exp(i\phi_i)\right) \quad (1.1)$$

where \sum_i denotes a sum over all the spots i , A_i sets the amplitude and phase of each spot, and $\arg()$ denotes taking the phase of a complex number.

However, in general this method produces more than just the desired spots: we only modulate the phase of the laser beam and not the amplitude, which means there is too much light on some parts of the hologram. This surplus light shows up as “ghost orders”, extra spots that are produced but were not intentionally in the hologram. Ghost orders are a particular problem in highly symmetric arrays of traps, especially if all the amplitudes A_i are identical (i.e. the spots all have the same phase).

By using iterative algorithms, it is possible to create highly efficient, uniform arrays of spots. These algorithms generally optimise the relative phase ($\arg(A_i)$) of the light fields which are summed to create the final hologram [44, 45]. The most effective algorithms are iterative Fourier transform algorithms, the first example of which was used by Gerchberg and Saxton [46] to analyse X ray diffraction patterns. Such algorithms iteratively transform between the spot pattern actually produced by the hologram and the hologram itself, replacing the intensity in each plane but preserving the phase as shown in Figure 1.9. By repeatedly optimising the intensities in the two planes, very good results can be obtained quickly—despite having nearly a million degrees of freedom, convergence is often reached in ten or twenty iterations.

There are many generalisations of the basic G–S algorithm [47, 48] which make it converge faster, or reduce its tendency to get stuck in local minima. DiLeonardo *et al.* implemented a version which does not use Fourier transforms, but calculates the intensity and phase of the spots directly [45]. For the specific case of optical tweezers, this can be more efficient and also allows the use of spots which are not in the focal plane of the sample.

A simpler approach (though it is less effective for large, regular arrays) is to randomise the phase of each spot, corresponding to adding a random constant to each of the ϕ_i terms in the sum. Adding artificial noise to the trap positions in a large array can decrease the symmetry enough to significantly improve the quality of the array. The traps need only be jittered by a few hundred nanometres in order to realise this improvement, and this degree of

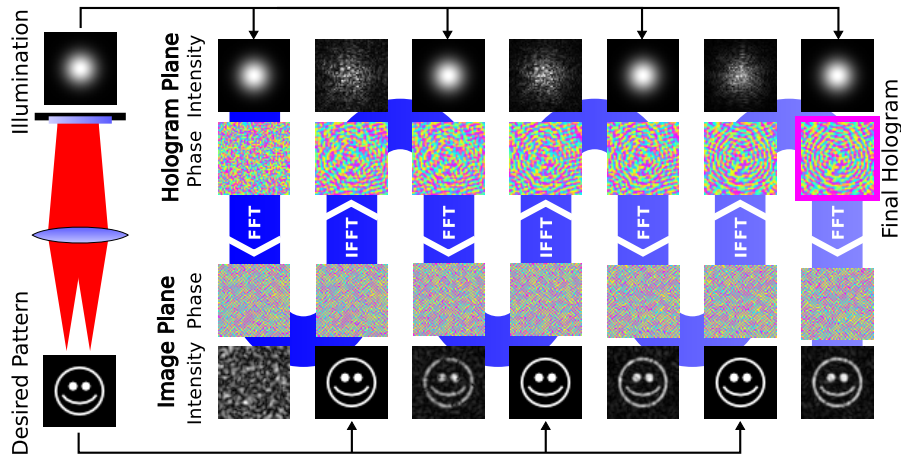


Figure 1.9: The Gerchberg-Saxton algorithm is an efficient way of producing optimised holograms for complicated patterns. Fast Fourier Transforms (FFTs) are used to transform repeatedly between the hologram plane and the target plane. In each plane, the intensity is replaced either with the target intensity or with the known illumination pattern, and the algorithm converges to a stable solution after surprisingly few iterations.

asymmetry is insignificant for many applications of trap arrays [49].

One can reduce the appearance of ghost orders near the spots of interest even further by deliberately decreasing the efficiency of certain points on the SLM (either analytically or with an iterative algorithm), thus modulating both intensity and phase [50, 51]. This does, however, entail a decrease in the intensity of the desired spots as a necessary consequence of the removal of the ghost orders. It is also possible to go some way towards correcting for imperfections in the SLM with software: Persson *et al.* have compensated for the response time of the liquid crystal layer [52] and crosstalk between adjacent pixels [53].

Simple algorithms are often favoured not just because they are easier to implement, but because they require less calculation time. When manipulating particles, it is useful to be able to update the hologram as fast as the SLM can display it, usually around 60 Hz. However, even with a relatively fast multi-core CPU (for example a quad core 3 GHz Pentium 4), holograms

can only be calculated at the required resolution around ten times per second and this has been a serious limitation on holographic tweezers in the past. However, the use of consumer graphics cards has enabled much faster hologram generation as described in Chapter 3. This allows the tweezers system to react on the timescale of the particle's Brownian motion, which enables active feedback to increase the effective stiffness of a trap [54,55]. As modern graphics cards have increased in power it has even been possible to implement iterative algorithms in real time [56], though with higher latency than the simple algorithms used for active feedback.

In addition to creating multiple focused spots and moving them around, SLMs allow very general modifications to be made to the light beam. As such they have been used to generate optical traps carrying orbital angular momentum, dubbed "optical spanners" [57,58] and create extended line and ring traps [59,60]. This ability to modify the shape of the focal spot in 3D is used to trade off axial and lateral stiffness in a trap in Chapter 5. Focal spot engineering with SLMs has also been used in microscopy, for example providing edge enhancement [61] or 3D tracking [62].

1.2.4 Laser sources

One of the fundamental requirements of an optical tweezers system is the laser, which is often the most expensive component of any trapping set-up. The wavelength of laser used is important for biological experiments, as absorption of the laser causes heating and other effects and can lead to damage of the sample, or "opticutition" [63]. This is of particular relevance when live cells are to be trapped directly, and a number of studies on various organisms [64,65] have suggested that damage is minimised by using near-infrared wavelengths, although it is important to check cell viability for the particular cells and laser system used in any new experiment. The two most frequently used wavelengths are 1064 nm and around 820 nm. These coincide with local minima in the optical absorption spectrum of water, as well as corresponding to commercially available laser technologies. The water absorption curve is

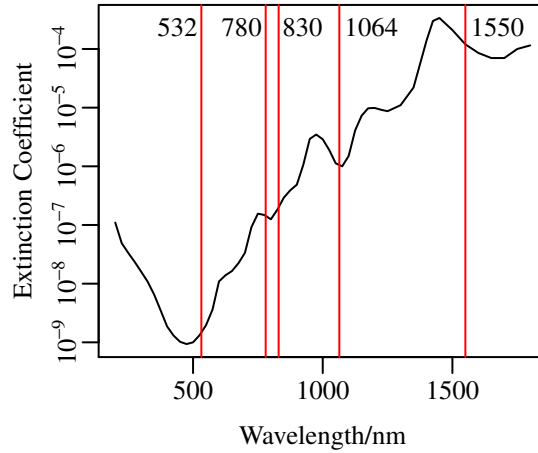


Figure 1.10: The optical absorption curve for water, overlaid with some common laser wavelengths. Green (532nm) light is typically avoided when biological specimens are to be used, leaving the regions around 800nm (tunable Ti:Sapphire lasers or diodes at 780nm or 830nm) and 1064nm (Nd:YAG) as the most convenient wavelengths. Data taken from [66,67].

shown in Figure 1.10 along with some common laser wavelengths. The former wavelength is that of Nd:YAG lasers, available as “turn-key” Diode Pumped Solid State (DPSS) lasers which require no set-up other than switching them on and adjusting the power level. Commercial Titanium:Sapphire lasers are also available, with wavelengths between about 780 nm and 830 nm. These lasers are more complicated (as they are frequently supplied with the option to tune the output wavelength or produce short pulses), however they are available in reliable, commercial systems.

Pointing stability, i.e. the drift of a laser’s output beam over time, is another parameter in an optical tweezers system which has an effect on force measurement. Combined with the stability of the rest of the optical system, it sets an upper bound on the length of experiments which can be performed before drift (either of the laser or of the microscope optics) degrades the accuracy of force or position measurements. Typically, drift starts to become noticeable after tens of seconds [68,69]. It is possible, however, to alleviate

drift by taking differential measurements between two traps [34]. Power stability should also be taken into consideration, as variation in the laser power will lead to a corresponding change in the stiffness of the optical trap.

1.2.5 Objective lenses and beam shape

Single-beam optical traps require a high numerical aperture (NA) in order for the trap to be stable in three dimensions. Combined with the small size of objects usually trapped, this leads to the use of high-magnification, high-NA objectives, typically $100\times$ or $60\times$ with an NA of at least 1.2. These objectives are usually designed for fluorescence microscopy, and are usually oil- or water-immersion. The use of water-immersion objectives minimises spherical aberration, which is another limiting factor for 3D trapping; too much spherical aberration can degrade the trap's axial stiffness to the point where it is no longer stable in the axial direction [70], particularly for small or highly scattering particles [10]. Changing the refractive index of the immersion oil is one way of alleviating this problem for oil-immersion objectives, which has been used to good effect with nanoparticles [10, 71]. Other aberrations induced by misalignments or imperfections in the system, or by heterogeneities in the sample, can give rise to a mis-shapen focus leading to different stiffnesses in different directions or even the failure to trap particles altogether. To address this problem, a number of adaptive optics approaches have been taken, including the technique described in Chapter 4. Aberrations can be cancelled out using the same SLM which steers the beam in holographic optical tweezers [72–74].

1.3 Counterpropagating optical traps

Some years before demonstrating the single-beam gradient trap now referred to as “optical tweezers”, Ashkin demonstrated the stable trapping of particles between the foci of two counterpropagating beams, at much lower NA [1]. This sidesteps the issue of particles being pushed out the back of the trap

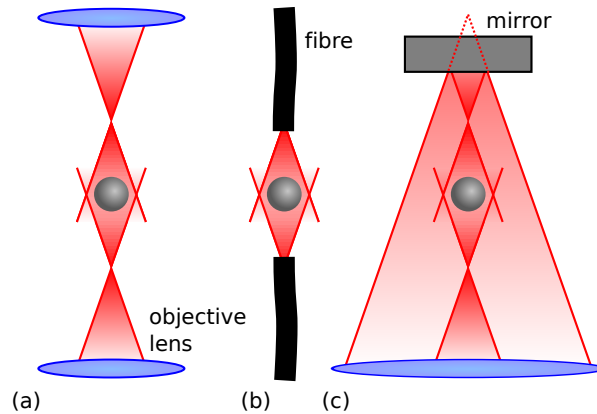


Figure 1.11: Different configurations for forming counterpropagating optical traps: (a) two opposing objective lenses, (b) two fibres, and (c) a single objective lens and a mirror, using an SLM to create two foci displaced from each other axially.

by radiation pressure, as the scattering forces from the two beams cancel out when the particle is central. The particle is trapped laterally by the same mechanisms as in a single-beam trap, however axial trapping is provided by a combination of gradient and scattering forces. Most usually, the foci of the two beams are displaced to put them outside of the particle as shown in Figure 1.11, such that when it moves towards one focus the scattering force from that trap is higher and pushes it back towards the centre. This approach frees us from the constraints of high-NA objective lenses and allows a much larger field of view. This also isolates the trapped object from the high light intensity at the laser foci. It is worth noting that the intensity at the focus of a low-NA lens is already much reduced from the peak intensity at a high-NA focus.

Counterpropagating traps can be formed using two opposing objective lenses and still leave sufficient clearance for large sample cells [75] or even a side-looking microscope or spectroscopy system [76]. It is also possible to form a counterpropagating trap without any lenses, simply by using two optical fibres. The tips of the fibres replace the foci of the two beams in

the lens-based system, and objects are stably trapped between them. Dual fibre optical traps have been used to hold and deform biological cells [77]. This deformation allows the mechanical properties of the cell to be probed, and this has been investigated in the context of some medical conditions, most notably cancer [78]. The two-fibre geometry does not use a microscope objective, and thus it is more flexible in that it can be integrated with a microfluidic chip [78], which has been used to allow a much higher throughput of cells than is attainable with microscope-based optical tweezers.

More recently, counterpropagating optical traps have been realised with a single objective lens [79, 80]. By using a low-NA lens in a holographic optical tweezers system, it is possible to create foci over an extended axial range. A mirror placed behind the sample can reflect some of these foci back into the sample. Thus, any beam which would focus behind the mirror actually focuses inside the sample, but is propagating in the opposite direction. This enables a single objective to produce multiple counterpropagating traps, which can be freely moved in 3D. This approach is arguably more convenient than the dual objective geometry, and has the advantage of being able to alter the focal planes of each beam individually. In contrast, most dual objective systems alter the balance of intensity in upper and lower beams, which consequently changes the equilibrium trapping position. However, in both cases the axial stiffness can be very low, and the active feedback described in Chapter 6 can be used to dramatically increase the accuracy with which particles are placed in z [81, 82].

1.4 Force and position measurement

As discussed in Section 1.1, an optical trap exerts a force on the trapped object which is modelled well (for small separations) by a Hookean spring, i.e. the force is linearly proportional to the displacement. Thus, we can measure forces by measuring the displacement of a bead and multiplying by a spring constant to find the force. Particles can typically be tracked with resolu-

tion better than a few nanometres, and spring constants are usually around $1 \mu\text{Nm}^{-1}$. Brownian motion sets a fundamental limit on the accuracy of forces which can be measured, but typically tens to hundreds of femtoNewtons can be attained if data is averaged over a few seconds. The experimental hardware used to measure forces and displacements falls into two categories: laser-based detection and video camera systems.

1.4.1 Laser position detection

When a trapped object is displaced from the laser focus, it alters the distribution of light leaving the trap. In the case of a sphere, this results in a change in direction of the light which causes a translation of the intensity pattern in the back focal plane of the condenser lens, as illustrated in Figure 1.12. The shift of the pattern is usually measured with a position sensitive detector (PSD) or a quadrant photodiode (QPD) as shown in Figure 1.12 [83, 84]. A PSD returns the coordinates of the centre-of-mass of the light hitting its active surface, while a QPD simply returns the total intensity hitting each of the four quadrants of the detector. In the latter case, the shift of the pattern is given by the difference between the two halves of the detector, as shown in Figure 1.12. This method of detection has been reported with precision down to 0.1 \AA [85], with bandwidths of up to 1 MHz. However, it does require relatively precise alignment and calibration of the relationship between detector signal and distance. Looking at the forward scattered laser light gives the displacement of the particle relative to the laser focus, which means it will be relatively insensitive to drift in the laser beam's direction. However, if the focus does shift and the measurement depends on the particle's absolute position in the sample (e.g. a long molecule is fixed at one end to the slide and at the other end to a trapped bead), then drift in the laser's direction will look like a change in the particle's displacement, even if the particle stays in the same place.

Extending this technique to multiple particles requires separating out the light which has passed through each optical trap. This is most often done

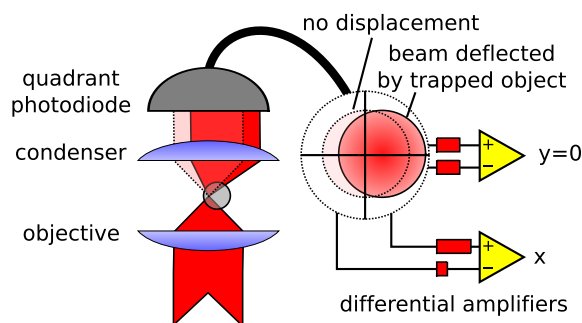


Figure 1.12: Quadrant photodiodes are an extremely sensitive way of measuring the position of a trapped object, by looking at the deflection of the beam. As the beam is bent, it is displaced in the back focal plane of the condenser. The two halves of the QPD are therefore illuminated differently, and the difference between the two halves is proportional to the particle’s displacement.

using a polarising beamsplitter, where the two traps have orthogonal polarisations [34]. However, care must be taken to avoid crosstalk between the two traps when using laser-based position detection [86]. It is also possible to use a dichroic mirror in combination with separate “detection lasers” of different wavelengths, however these detection lasers must be precisely aligned with each optical trap and so very high pointing stability is required in all the lasers used to keep the system accurate over a long period of time. In the case of time-shared optical traps using an acousto-optic modulator or a scanning mirror, it is possible to separate the particles by precisely timing the readout of the detector [37, 87, 88]. This has also been used to track several particles in a line-shaped optical trap, made by rapidly scanning a single trap back and forth [89].

Axial tracking is also possible using a quadrant photodiode or PSD, by looking at the divergence of the light [85, 90]. Axial displacement of the particle will make the light more or less divergent and, if it is arranged to slightly overfill the detector (or the condenser has a lower NA than the objective), this will change the total intensity incident on the detector as

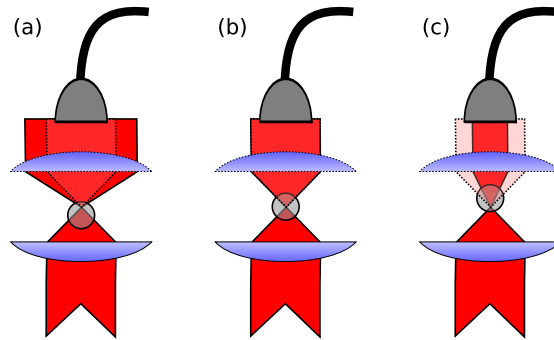


Figure 1.13: Quadrant photodiodes can be used to measure axial displacement by exploiting the change in divergence of the beam. If the detector is overfilled, an increase in divergence (due to the trapped particle moving closer to the microscope objective) will cause the signal to decrease. Similarly, if the particle moves away from the microscope objective, more light is concentrated onto the photodiode and the signal increases.

shown in Figure 1.13. The relationship between intensity and axial position is also approximately linear over the optical trap.

Calibration of the relationship between displacement and detector signal is generally carried out using a precision stage [90]. A particle identical to those used for force measurement is fixed to the microscope coverslip and moved in steps of a known size, and the resulting signal is recorded. This relationship is dependent on the size and composition of the particle, and the refractive index of the medium. It must therefore be repeated for each particle size and material used. The range over which such a detection scheme is linear is around the same as the region over which the optical trap has a linear force-distance relationship.

By collecting all of the light which has passed through the particle, it is in theory possible to extract the force on the particle with no calibration, by simply considering the change in momentum of the light. This has been done using counterpropagating traps with relatively low numerical aperture [91]. However, it is rarely possible to reach this level of efficiency when using a high-NA trapping objective even with oil immersion condensers, and so

empirical calibration remains the norm. Also, the force extracted is the total force on the sample: if other objects distort the beam, this will introduce artefacts.

1.4.2 Video particle tracking

Position measurement using a laser is precise and provides very high bandwidth. However it is often challenging to align and calibrate such systems, and extending them to multiple particles is difficult. It is possible to precisely locate particles in a video image, often to an accuracy of around one hundredth of a pixel [92] corresponding to a few nanometres. Particle tracking microscopy is often used to make measurements of flow or viscosity in Particle Imaging Velocimetry (PIV), where tracer particles are added to a system and their trajectories are analysed [93]. Often these particles are the same glass or plastic micro-beads used in optical tweezers experiments, imaged using either bright-field or fluorescence microscopy. PIV can be performed with a camera operating at standard video frame rates, a few tens of Hertz. In optical tweezers, it is often necessary to observe the motion of a trapped object at high speed, with a bandwidth of thousands of Hertz, as the motion of a trapped particle averages to zero over times on the order of a few tens of milliseconds. Early camera-based optical tweezers experiments increased the viscosity of the trapping medium to slow down phenomena of interest [94], however this is no longer necessary [95]. Relatively inexpensive CMOS cameras now meet this requirement, attaining frame rates of several kHz [68, 96] up to tens of kHz for more sophisticated cameras [97]. This is generally achieved by reading out only a subset of the pixels on the sensor chip, which decreases the time required to acquire an image and transfer it to a computer.

Tracking optically trapped particles requires relatively simple image analysis, which can now be performed on-the-fly using a typical desktop computer. When a small spherical object is slightly behind the focal plane of the microscope, it appears as a bright spot surrounded by a dark ring under

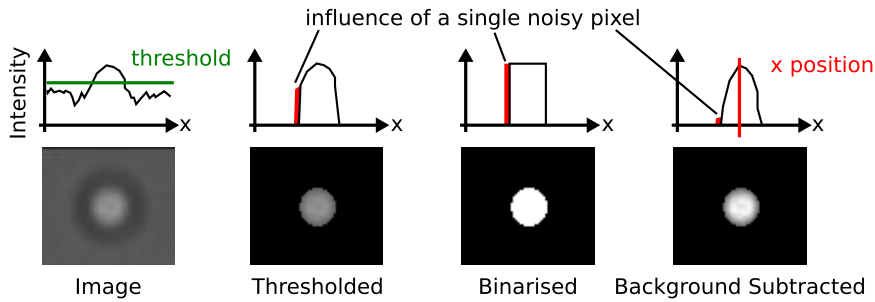


Figure 1.14: A typical image of a $2\ \mu\text{m}$ silica bead in an optical tweezers system and some methods of tracking it. The distributions of intensity are shown beside each image. The centre of mass works by finding the mean x and y position of the intensity, which can locate the particle to $1/100$ of a pixel. From left to right, the images are unprocessed, thresholded (i.e. pixels set to black if they are below a threshold), binarised (as before, but set to white if they are above the threshold) and background subtracted (a constant is subtracted from the image and negative pixels are clipped to zero). The last scheme is less susceptible to camera noise and exhibits less discretisation than the threshold approaches.

bright-field illumination. After removing the background with a threshold function, simple centre-of-mass algorithms can track particles in 2D with a precision of a few nm and a bandwidth of several kHz [68, 96]. Figure 1.14 shows a typical image of a $2\ \mu\text{m}$ bead in an optical trap, and the image after a threshold function has been applied. The “centre of mass” algorithm then operates on the background subtracted image to find the centre of the particle, by considering the mean position of the intensity in the image. This is a very efficient calculation to perform, as it requires just three summations over the pixels in an image, which can be done simultaneously. If the intensity of the pixel at position (x, y) is $I_{x,y}$, we evaluate $S_I = \sum_x \sum_y I_{x,y}$, $S_x = \sum_x \sum_y x \times I_{x,y}$ and $S_y = \sum_x \sum_y y \times I_{x,y}$. The position is then given as $(S_x/S_I, S_y/S_I)$. This is analogous to calculating the mean of a dataset, where the points are weighted by their intensities. A slightly more subtle point is the difference between background subtraction and thresholding: the former

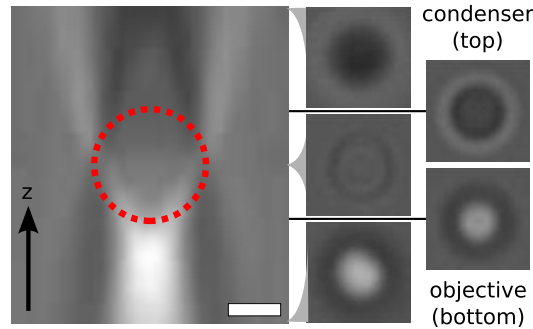


Figure 1.15: An x - z slice through the light scattered by a glass bead in a high-NA, bright field microscope. The beads position is shown, together with camera images from various depths. Scale bar is $1\ \mu\text{m}$.

subtracts a constant from the image such that the background is zero, while the latter sets pixels to zero if they are below a given value but leaves other pixels either unchanged or set to their maximum value. The latter approach means that pixels which are close to the threshold value can flicker on and off, which can cause noise on the position signal in some cases.

A well-designed particle tracking algorithm can attain a resolution of order $1/100$ pixel, or typically about $1\ \text{nm}$ [98]. Tracking particles with sub-pixel accuracy enables camera-based systems to make force measurements which approach the thermal limit on accuracy set by Brownian motion [68]. More sophisticated analysis of images allows particles to be tracked over a larger axial range (for example, the symmetry based algorithm described in Chapter 2. Image analysis can even recover particles' axial positions [99], by exploiting the fact that a bead's appearance on the camera varies with its depth, as illustrated in Figure 1.15. Axial measurements require calibration for each different bead and medium used (as changes in refractive index, etc. will change the appearance of the bead), and so a closed-loop piezo stage is usually required for calibration, as with laser-based detection schemes.

Digital Holographic Microscopy (DHM) has been used for particle tracking in the context of optical tweezers [100]. DHM also uses sophisticated image analysis to recover 3D position information, this time from an image

taken using coherent light. It is possible to fit to an analytic model based on generalised Lorentz-Mie theory to the image of a particle. This approach recovers 3D position as well as size and refractive index, however this is particularly demanding and only approaches video rates when accelerated with Graphics Processing Unit technology [101]. Using coherent light in imaging carries with it the inherent problem of speckle; any light scattered from outside of the focal plane (for example dust on lenses or out-of-focus objects in the sample) will interfere with the image. This can cause degradation of image quality, requiring careful calibration and removal of the noisy background image.

Detailed image analysis will become faster as computer power increases, but at the present time stereoscopic particle tracking as described in Chapter 2 and other techniques based on a modified imaging system [62] have the advantage of giving 3D information with only relatively simple image analysis. Stereoscopic imaging produces two images of the sample from different viewpoints, then uses parallax to find depth information. Once the pixel size of the camera and angle between the viewpoints are known, there is no need for further calibration and thus this technique is relatively robust to changes in trapped objects, etc. Typically, bright-field illumination is used to maximise the available light, but instead of illuminating on axis, two off axis sources are used. This produces a double image, where the two images of a particle converge when it is in focus. After using either colour [102] or a Fourier filter [15] to separate the two images, particle tracking can be performed on each, and the particle's 3D position extracted with an accuracy of nanometres [55].

Image analysis with a camera can also measure other properties, for example the distortion of objects held in an "optical stretcher" [77]. This is one case where it is difficult to reduce the optical signal to something which can easily be picked up by a photodiode, and thus camera tracking is by far the easiest option. Cameras can be used to track heterogeneous objects such as cells [98], which will provide a distorted signal when measured using

back-focal-plane interferometry.

1.4.3 Particle dynamics and calibration

Any particle immersed in a fluid is constantly bombarded by the atoms or molecules of the medium, as they undergo random thermal motion. This gives rise to Brownian motion, or diffusion, of the particle [4, 103, 104]. By analysing this random motion, it is possible to learn both about the optical trap and about the medium in which the trapped object is immersed. This is essential if we are to make force measurements, as we relate the force F to the displacement of the particle x using the stiffness of the optical trap κ :

$$F = \kappa x$$

The simplest approach to this comes from thermodynamics; the equipartition theorem tells us that, on average, the energy stored in each degree of freedom in a system is $k_B T/2$, where k_B is Boltzmann's constant and T is the temperature. The energy stored in a linear spring (such as our optical trap) is $\kappa x^2/2$. Thus, by averaging over many measurements of the bead's position we can find $\langle x^2 \rangle$ (where the $\langle \rangle$ denote averaging over time), and calculate the stiffness:

$$\kappa = k_B T / \langle x^2 \rangle$$

At the small length scales of optical tweezers, the mass of a trapped object is insignificant compared to viscous drag effects and the motion is overdamped, i.e. the particle will not keep moving due to inertia, but will stop once it is no longer being pushed along. Neglecting inertia allows us to describe its motion with a simple equation:

$$\gamma \dot{x} + \kappa x = \zeta$$

where x is the position of the bead and \dot{x} its velocity, γ is a friction coefficient (proportional to the viscosity of the fluid) and ζ is a fluctuating force term, representing the random collisions of molecules with the trapped particle.

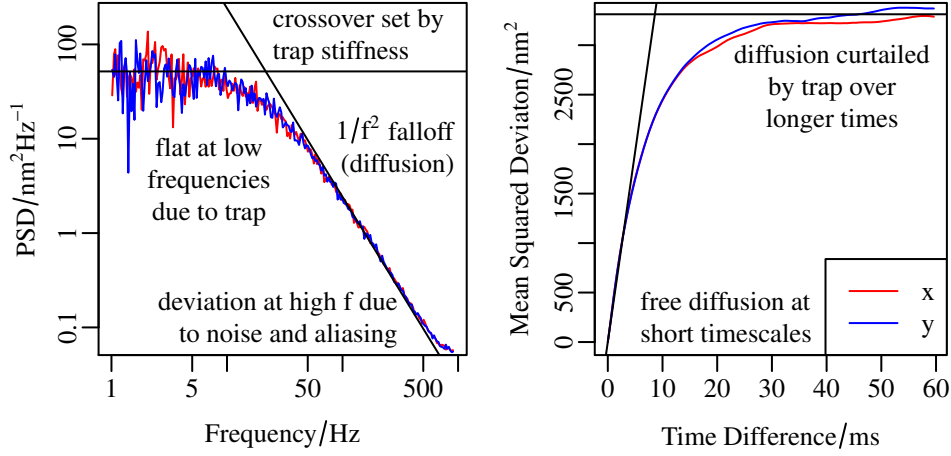


Figure 1.16: A typical power spectrum, measured by video particle tracking. It has the characteristic Lorentzian shape, with a plateau at low frequency (as the particle’s diffusion is curtailed by the trap) and a tail proportional to ω^{-2} (corresponding to free diffusion over short timescales). The crossover between the two regions is determined by the ratio of trap strength to fluid viscosity. The mean squared displacement (right), shows the same information in the time domain.

An untrapped particle follows a random walk, where the distance travelled after a time t is proportional to the square root of t . Trapped particles also move in this way, but after a short time the trap acts to pull the particle back towards the centre, and limits the distance travelled. This is most often visualised by plotting the Power Spectral Density (PSD) of the particle’s position fluctuations, which has a characteristic Lorentzian shape shown in Figure 1.16 and described by the equation:

$$\text{PSD} = \frac{2k_B T / \pi \gamma}{\omega_c^2 + \omega^2}$$

where $\omega_c = \kappa / \gamma$ is the “corner frequency” [105]. This is described more fully in Chapter 3.

Analysis of the power spectrum allows the trap stiffness κ to be determined in some situations where the simple equipartition expression is unreli-

able. One can determine other properties of the system, such as viscosity and even viscoelastic moduli, by further analysing the motion of a trapped object as described by its PSD [106–108]. Equivalently, this analysis can use the Mean Squared Displacement (MSD) or the autocorrelation function, which represent the same information in the time domain. It is also possible to probe viscoelastic properties by actively driving the bead’s motion (through moving the trap [109] or the use of spinning, birefringent particles [110]) and observing the bead’s response, which can achieve a higher signal-to-noise ratio in some circumstances.

1.5 Optically Actuated Tools

Optical tweezers usually employ micron-sized dielectric spheres to couple optical forces to the specimen being probed. This has worked very well for experiments with biopolymers [111], however the radius of curvature limits the usefulness of such spheres for techniques such as contact imaging. This can, of course, be improved by the use of smaller spherical probes [85, 112], though more of the trapping laser will then hit the sample. This intensely focused light can damage sensitive specimens, and conversely the sample will distort the laser beam, which can lead to errors in force or position measurement. An alternative approach is the use of tools, extended structures which feature sharp tips that interact with the sample and larger structures which can be manipulated with the laser beam.

Micron-sized dielectric spheres are the most convenient objects to hold in optical traps, and can be conveniently tracked by a variety of methods. It is little surprise, then, that most optically actuated tools incorporate micron sized “handles” for the trapping laser to manipulate. The other essential ingredient for a tool or probe is the part that interacts with the object we are investigating. As the size of the tip strongly affects the resolution of our sensing, be it contact imaging or probing for molecular interactions, the minimum feature size attainable is a key parameter when considering how to

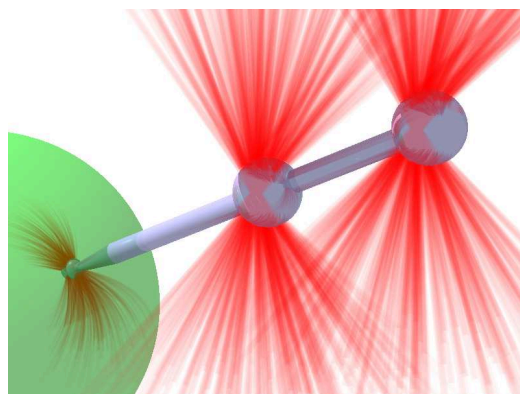


Figure 1.17: An illustration of an optically actuated micro tool, with two handles and a sharp tip, probing the surface of an object.

make such tools. The simplest design for a probe consists of two handles and a sharp tip, arranged such that they are collinear as shown in Figure 1.17. Such a probe can be said to have five useful degrees of freedom, as rotation about its symmetry axis is both hard to effect and difficult to detect. Probes of this sort have many of the advantages discussed, in that they allow the use of a tip much sharper than the trapping handles, and they remove the trap sites from the object being probed, but any deviation from cylindrical symmetry introduces error into the reconstructed position of the tip, through unaccounted-for rotation. To escape some of these limitations, one might add a third trapping handle to the tool. At the expense of increasing the complexity of its fabrication, this provides access to all six degrees of freedom and increases the possibilities for shaping the optical spring that holds it in place.

Much of the prior work on tools has used counterpropagating, low-NA traps [75, 113] and has not yet demonstrated precise tracking and force measurement. Many of the techniques described in the coming chapters have been developed in the context of the “Optical AFM” project, which aims to use optically actuated tools to probe tiny forces and structures, combining some of the advantages of Atomic Force Microscopy (AFM) and optical tweezers. I have worked closely with colleagues at the University of Bristol,

where much of the work on probe development and calibration has taken place, to apply the techniques in this thesis (particularly Chapters 2 and 3) to micro-tools. Over the last few years, we have worked with probes assembled from rods and spheres [114, 115], individual micro-rods [116], naturally occurring structures [117] and tools made using two-photon polymerisation.

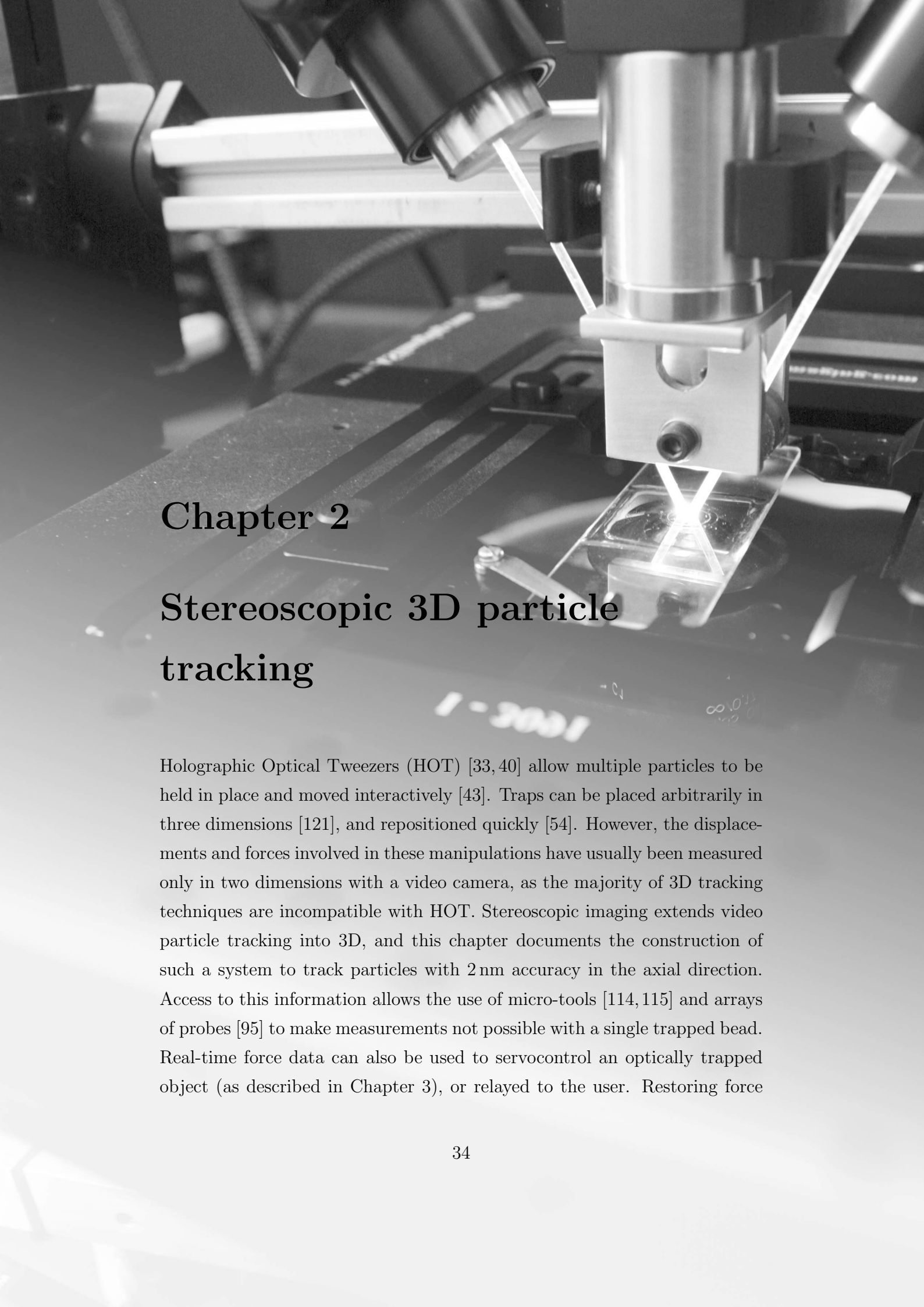
Key to understanding the requirements of working with micro tools are the extra degrees of freedom afforded by such objects. Whereas a spherical bead has three useful degrees of freedom, a rigid, non-spherical tool has six: its orientation becomes important. As the object rotates, the probe tip will usually move. Thus, measuring the position of the probe is no longer sufficient to find the interaction point. Similarly, forces applied to the probe will not just show up as a displacement from its equilibrium position, but as a rotation from its equilibrium orientation. Understanding the motion of such tools and how best to calibrate them has been the subject of experimental [115, 118] and theoretical [119, 120] investigation at Bristol. An important point arising from this is that the motion of such tools is no longer trivially separable into x , y and z components. This means that measuring the axial, as well as lateral, position of the probe is important. Chapter 2 aims to address this problem in a way which permits simultaneous monitoring of multiple points. This allows us to follow the motion of several trapping handles (which, being micron-sized, are easy to track) and then recover the motion of the tip (a much harder object to track directly). The motion of the tip, and the force passing through it, allows us to produce contact images of soft objects, and measure femtoNewton forces without illuminating the specimen with intense laser light.

1.6 Discussion

Optical trapping is now a well-developed technique, able to manipulate micron-sized objects such as beads and cells. It is capable of applying and measuring forces from tens of picoNewtons down to femtoNewtons, on multiple particles

simultaneously. This has been used to break new ground in research into the properties of biological molecules such as DNA and molecular motors like kinesins and myosins. As the technique continues to develop, the potential for its use in biological and biophysical experiments as well as its availability to non specialists is continually increasing.

In the following chapters, I will describe the developments I have made in this technique during my doctoral studies, as well as some of their applications. The technological advances include speeding up hologram generation with a GPU and fast 3D tracking in a stereomicroscope. These are important steps in the development of optically actuated micro-tools. The impact of these technologies on counterpropagating traps is also investigated in Chapter 6, where I show they can increase the stiffness of a low-NA trap to values normally only found in high-NA, single beam tweezers.



Chapter 2

Stereoscopic 3D particle tracking

Holographic Optical Tweezers (HOT) [33, 40] allow multiple particles to be held in place and moved interactively [43]. Traps can be placed arbitrarily in three dimensions [121], and repositioned quickly [54]. However, the displacements and forces involved in these manipulations have usually been measured only in two dimensions with a video camera, as the majority of 3D tracking techniques are incompatible with HOT. Stereoscopic imaging extends video particle tracking into 3D, and this chapter documents the construction of such a system to track particles with 2 nm accuracy in the axial direction. Access to this information allows the use of micro-tools [114, 115] and arrays of probes [95] to make measurements not possible with a single trapped bead. Real-time force data can also be used to servocontrol an optically trapped object (as described in Chapter 3), or relayed to the user. Restoring force

perception in this way (described in more detail in Chapter 7) increases dexterity for fine manipulation tasks, and enables the operator to qualitatively investigate a sample prior to quantitative measurements.

Measurement of the axial displacement of a single particle can be performed by looking at the interference pattern formed by the laser light transmitted through the sample, often termed Back Focal Plane interferometry (BFP interferometry) [83–85]. This approach has achieved excellent accuracy (sub-nanometre in some cases) and bandwidth (up to tens or hundreds of kHz), but requires considerable effort to track more than two particles [89]. In order to track multiple particles using BFP interferometry, it is necessary to separate the light from each optical trap after it has passed through the sample. For two traps this can be done using a polarising beamsplitter, and for more time-shared traps it is possible to demultiplex the signal to recover positions for each trap [37, 88, 89]. However, holographically controlled traps have the same polarisation and are not time-shared, which precludes either of these techniques. Fluorescent beads also allow measurement of axial position by monitoring the intensity of fluorescence excited by the trapping laser (in a two-photon process) [122], or by an evanescent wave from the coverglass [123]. Both these fluorescence techniques achieve an axial accuracy of around 10 nm, but as fluorescence is measured with a single photodetector they are again unsuitable for use with multiple traps. The latter technique is further restricted to measurements close to the microscope coverglass by the exponentially decaying evanescent field.

Stereomicroscopy was the first technique to allow perception of depth in microscopes. Just as in normal vision, each eye of the microscopist is presented with a view of the sample from a slightly different angle. This means that the difference in an object's lateral position in the two images varies linearly with depth, as shown in Figure 2.1. This is one of the ways the human brain judges distance (for most people, this is the primary method). We can replicate this very simply in a computer vision system, by tracking an object's two dimensional position in each image, then finding the difference in

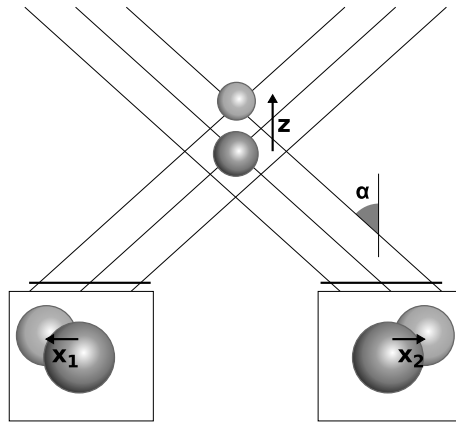


Figure 2.1: An illustration of stereoscopic imaging. Each eye is presented with a view in which the x position of an object varies with its z position. By tracking in x and y in both images, we can recover z .

x position between the images and multiplying by a scaling factor to recover the axial position.

The combination of intuitive depth perception for the operator and quantitative measurement of axial displacement afforded by stereomicroscopy is an excellent match to the 3D manipulation capabilities of holographic optical tweezers. As the particle need only be tracked in 2D in each image, 3D position information can be extracted at up to several kHz. This makes it possible to enhance trap stiffness in 3D with feedback control, as described in Chapter 3. This is particularly useful in the axial direction, where trap stiffness is usually lower. Forces can also be relayed to the operator in real time (Chapter 7), which is an important step towards creating an intuitive and transparent way of interacting with micron-sized objects.

Some other video-based techniques allow measurement of axial position, however this is at the expense of relatively demanding image analysis which limits the speed to tens of frames per second [124, 125]. Digital holographic microscopy is a promising technique for three dimensional microscopy [126], where coherent light is used instead of the normal white light illumination to allow better resolution and/or numerical refocusing of the image after it has

been acquired. This can be used to generate a stack of axial sections of the sample from a single acquired image, which in turn allows 3D information to be recovered. This technique has been applied to optical tweezers in recent years, by illuminating the sample with a collimated laser beam [124]. This in-line holography requires a very simple optical set-up, yet yields a wealth of information such as particle size and refractive index contrast when images are analysed by fitting to generalised Lorentz-Mie theory predictions for light scattered from a spherical particle. However, this analysis currently does not exceed tens of frames per second even when accelerated with Graphics Processor Unit (GPU) technology [124]. It is possible to use less exact methods to recover position information faster, such as numerical Rayleigh-Sommerfeld back-propagation [101] or analysing a recovered x - z plane [127]. While this is an excellent way of tracking multiple particles at tens of frames per second, it is still not yet fast enough to track a few particles at kHz rates.

2.1 Optical system

Axial resolution in a stereoscopic imaging system depends on the angle between the viewpoints. If we can track a particle with a resolution of δ in 2D, the resolution in z is $\delta/\tan\alpha$, where α is the angle between each viewpoint and the optical axis. The set-up described in this chapter consequently has a relatively large separation angle of 72° , i.e. $\alpha \approx 36^\circ$. Bright-field imaging with this separation angle requires illumination with an extremely high Numerical Aperture (NA), which is achieved using two 1.5mm acrylic optical fibres placed directly above the sample [15]. The fibres are illuminated with a pair of high intensity white LEDs, and a drop of water is used to more efficiently couple the light from the fibres into the glass microscope slide. This structured illumination is much more efficient than trying to fill the aperture of a high-NA condenser, only to discard most of the light.

Dam *et. al.* also used structured illumination to generate stereoscopic images [102, 128]. However, their system (based around lower-NA counter-

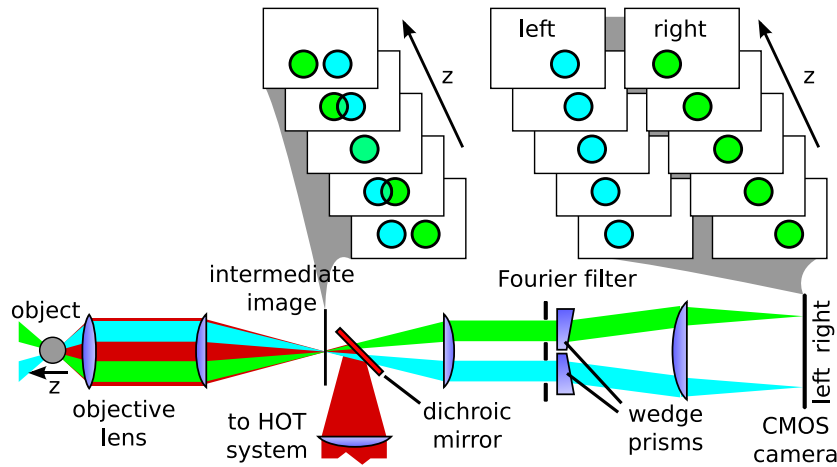


Figure 2.2: Outline of the imaging system used to produce stereo images. $4f$ imaging is used to image the sample, and again to re-image the sample. The Fourier filter separates the images viewing the sample from the left and the right.

propagating optical traps) used different colours for the two viewpoints. This enabled them to separate the light using a colour camera. My system does not use different colours or polarisations to distinguish the two views of the sample, to ensure that differences between the two viewpoints are not due to colour or polarisation anisotropies in the sample. Instead, the light from each fibre is separated in the Fourier plane of the sample, i.e. the image plane of the microscope's back aperture. A pair of apertures in this plane regularise the point spread function of the fibre-illuminated image, and behind each aperture there is a wedge prism (Comar 01-JW-25). The two beams are deviated by 1° in opposite directions, producing two separate images on the CMOS camera, as illustrated in Figure 2.2.

Separating the images optically preserves the benefits of traditional stereomicroscopy, for example it is possible to make use of other imaging modes (e.g. fluorescence). It also provides very good optical efficiency, as the only additional components are lenses and prisms which have small losses. This allows the use of short exposure times and hence frame rates of up to 1 kHz on

the Prosilica GC640M CMOS camera. With a more sensitive camera (EoSens 1362CL, Mikrotron, Germany), it is possible to track at over 10 kHz [97]. The field of view is 30 μm across, limited by the size of the sensor in the camera. The apertures in the Fourier plane are 1 mm in diameter, which sets the NA of each view at 0.3. This gives a diffraction-limited resolution of $\lambda/(2NA) \approx 900$ nm, compared to 220 nm for the full NA of the objective. Particles are visible over an axial range of 10 μm , and a displacement of one pixel on the camera corresponds to 150 nm in the sample. Distortion of the image between the two views of the sample should show up as non-flatness, i.e. if a bead is raster scanned over the XY plane it should appear to have different equilibrium axial positions as a function of lateral position. Performing this experiment gives a flatness of field of around 100 nm. This drops to better than 20 nm if we allow for slight misalignment of the SLM with respect to the imaging optics (by fitting a 3×3 transformation matrix which relates the coordinates used to generate holograms for the SLM and coordinates measured on the camera, where the off-diagonal terms were less than 1%).

The holographic optical tweezers system uses a Boulder Nonlinear Systems XY Series SLM imaged onto the back aperture of the objective (Zeiss Achroplan 100x, NA 1.2) similar to [15], controlled using the high-speed OpenGL software described in Chapter 3. The SLM is illuminated with an expanded 670 nm laser beam (Roithner LaserTechnik) with a maximum power of 300 mW.

2.2 Image analysis

3D tracking in a stereoscopic system can be accomplished by tracking an object's 2D position in both images. High speed cameras and desktop computers can now acquire and process images at several kHz [68]. Stereo video tracking as described in this chapter can provide on-the-fly 3D tracking data at 1 kHz, making it suitable for use in force feedback [129] and other

closed-loop systems [54]. However, most objects of interest in optical tweezers change their appearance as they move through the focus, particularly in bright-field imaging. This means that the usual approach of applying a threshold and finding the centre of mass of a bright particle (see Chapter 1) will not work if we are to track particles on both sides of the focal plane.

Often we are concerned with tracking symmetric objects, such as microspheres. Despite changes in their appearance as they go from one side of the focal plane to the other, the image is always symmetric (provided the system is reasonably well aligned). It is possible to track symmetric objects quite simply without a template, using a simple mathematical transform, referred to here as the “symmetry transform” [130]. This is a 1D operation, applied to each row (or to each column) of an image. For a row of pixels $p(x)$, the symmetry transform is:

$$S(x) = \int_{x'=-a}^a p(x-x') p(x+x') dx' \quad (2.1)$$

where a is generally chosen such that $x \pm x'$ does not fall outside of the available image data. $p(x)$ should have a constant subtracted from it such that its mean is zero.

Applying this transformation to each row yields an image with bright regions where the input image had a centre of symmetry. This is illustrated in Figure 2.3 for images of a $2\ \mu\text{m}$ bead at different depths. The position of the maximum in the marginal distribution (i.e. the sum of each column in the transformed image) gives the x position of the particle. A similar analysis is performed for y , operating on each column of the image. The position of the maximum is estimated with sub-pixel accuracy by numerically taking the first derivative, smoothing the derivative with a local linear regression [131], and performing linear interpolation to find the zero crossing. This approach is equivalent to fitting a quadratic to the peak. All these operations are linear and require no iteration, which means that finding the maximum is not computationally demanding.

This transform’s main advantage is that it has no parameters to set other than the search area and it requires no templates. This makes it robust to

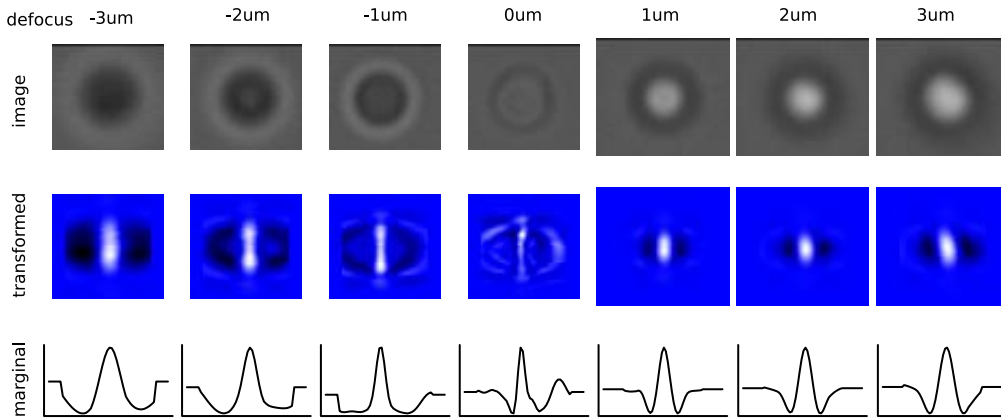


Figure 2.3: Images of a $2\ \mu\text{m}$ bead at different depths, before and after processing with a symmetry transform. The marginal distributions show a clear maximum for all depths. The transform, i.e. equation (2.1), is only evaluated over the central 40 pixels, hence the edges of the processed images and marginal distributions are fixed at zero. Video on enclosed disc.

changes in the system (such as differently-sized objects or a different refractive index of the bead) and obviates the need for sensor calibration routines or template images. The only parameter not already required for 2D tracking on a camera is the convergence angle of the beams, and the trap's force-distance relationship can be calibrated using the equipartition theorem [68] or the relaxation time [132]. The scaling from pixels to microns can be determined from geometric optics, or by using a calibration slide. This is independent of the stereo separation angle, as the microscope performs telecentric imaging (i.e. lateral distances are not distorted, as in an orthographic projection). It is also necessary to determine the position of the left and right views of the sample on the camera, however this only gives rise to a constant offset in position.

As the transform is performed independently on each row of the image, it is extremely efficient. A modern desktop PC (Intel Core i7 2.8Ghz) can perform several such transforms simultaneously in around $150\ \mu\text{s}$, on 60×60 pixel regions of interest. In practice, the speed is limited by the camera

frame rate to around 1 kHz. However, the particle tracking routine (including fetching the region of interest, processing the image and fitting the peak) was performed in less than 200 μ s. The 1D transform could be easily parallelised to take advantage of the processing power of a Graphics Processing Unit (GPU), which can outperform the CPU by an order of magnitude. However, in that case the movement of image data to the graphics card would have to be managed carefully to avoid this becoming the new bottleneck.

2.3 3D vision

The stereo imaging system produces two real images from left and right viewpoints. This allows us to give depth perception to the user through the use of a stereoscopic display (Zalman ZM-M220W). For simplicity and to maximise light efficiency, the images are taken from the same CMOS camera used for force measurement. This can be done using the multicast capability of the GigE Vision compatible camera (Prosilica GC640M), which relays the images from one camera to multiple computers over a small ethernet network. Using a second computer allowed the images to be processed and displayed without slowing down force measurement or interfering with the feedback loop rates. It is also possible, using multiple threads communicating asynchronously, to achieve similar performance on a single, multi-core computer. This was done when using the stereo system in conjunction with a CameraLink camera (Mikrotron EOSens 1362-CL) which allowed frame rates of up to 1000 Hz at 1280×512 pixel resolution (and was proportionally faster for smaller regions of interest). Frames from a stereoscopic video are shown in Figure 2.4, recorded using a reduced separation angle (to make the 3D effect more natural) and combined as the red and blue colour channels to allow them to be viewed with red–blue glasses.

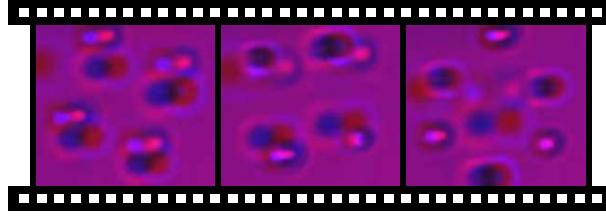


Figure 2.4: Frames from a red–blue anaglyphic video, showing a cube of $2\ \mu\text{m}$ beads being tumbled in 3D using holographic optical tweezers. The left and right eye images are captured by the stereomicroscope described in this chapter, and combined in software to make the anaglyphic video. Video [online](#) [55] or on enclosed disc.

2.4 Particle tracking accuracy

By tracking a bead which is firmly attached to a surface it is possible to assess the precision of the measurement system. This reveals a standard deviation of $3\ \text{nm}$ in x , y and z at $400\ \text{Hz}$, with an Allan variance which decreases with averaging time until about $0.1\ \text{s}$, where the error in position is around $1\ \text{nm}$ in all three dimensions. Thermal drift and laser pointing instability then cause the repeatability to deteriorate on timescales longer than a few seconds, as observed on a similar system in 2D [68]. Another method of estimating the error, which can be performed in real time, is to look at the difference in y positions of the two images of an object, similar to [98]. Motion in z should not affect the images' motions in y , and thus any difference in the two positions must be due to error. It is necessary to ensure that the two images of a particle are not at exactly the same height on the camera so that camera noise is uncorrelated between the images, as the noise is correlated along each sensor line (when using the GC640M).

Comparing y coordinates estimates the error on a single image as approximately $1 - 2\ \text{nm}$, though this takes into account only error in the image tracking and not drift and vibration in the system. As this method can be performed during force measurement, it is possible to use this error estimate to disable force feedback when the force signal is unreliable (e.g. when there

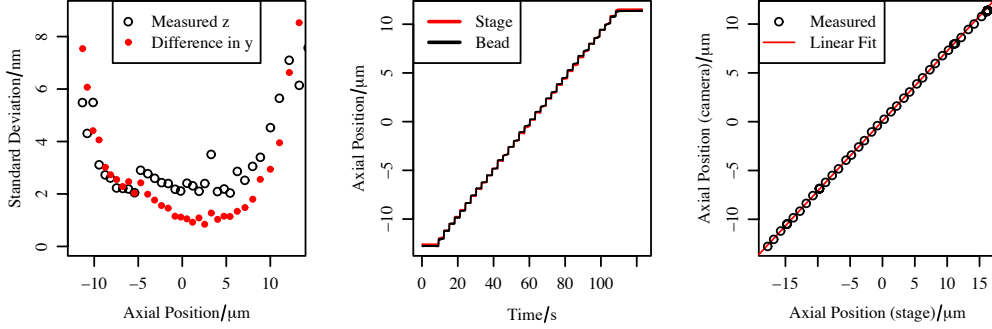


Figure 2.5: Measures of particle tracking accuracy, as a fixed $3\ \mu\text{m}$ bead is stepped axially. (left) Error as estimated from the apparent motion of a fixed bead, and from the difference in the two measured y values. (centre) The bead’s path, as reported by particle tracking and by the stage. (right) Measured position and stage position, showing a linear fit.

is no particle in the trap). Both error estimates are plotted as a function of depth in Figure 2.5, using a $3\ \mu\text{m}$ silica microsphere stuck to a coverslip and scanned in $1\ \mu\text{m}$ steps over the entire axial range. Figure 2.5 also shows the path taken by the bead, as reported by the stereoscopic tracking system and by the encoders on the Newport M-MFN25CC linear translation stage. Plotting stage position against measured z position shows the sensor to be linear to within 1% over the range of $-11\ \mu\text{m}$ to $5\ \mu\text{m}$. The stage position was scaled by a constant factor to match the measured particle position. This agreed with the predicted scaling factor (due to the changing depth of immersion oil) to within 10%. Exact agreement is not expected, as the prediction is from a simple geometric model that does not account for spherical aberration due to the oil immersion objective [90].

Analysing the Power Spectral Density (PSD) of the position fluctuations allows us to estimate white noise due to the camera. Figure 2.6 shows the PSD of a trapped $5\ \mu\text{m}$ silica bead’s fluctuations, with a reduced region of interest on the camera allowing it to run at 1 kHz. The PSD of a trapped bead’s fluctuations is Lorentzian in shape [105], meaning it falls off as $1/f^2$

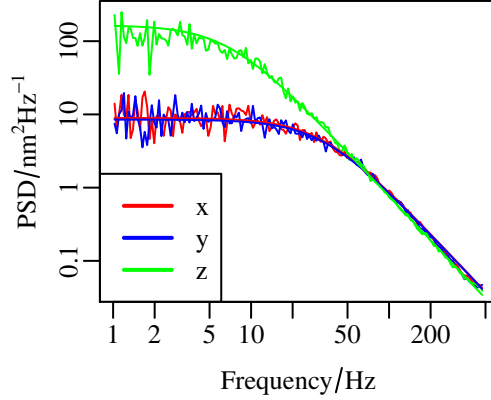


Figure 2.6: Power Spectral Density of a 5 μm silica bead's position fluctuations in an optical trap, from 60000 positions of the bead recorded at 1 ms time intervals. A Lorentzian fit (smooth line) is overlaid.

at high frequencies. Noise due to inaccurate measurement of the particle position should be uncorrelated between adjacent frames, so it is constant with frequency and causes the PSD to exceed the $1/f^2$ trend (a straight line on the log-log plot in Figure 2.6) at high frequencies. Aliasing due to the camera's finite frame rate also has this effect, however it is counteracted by the low pass filtering due to exposure time. Assuming that all the deviation from the Lorentzian at high frequency is due to camera noise yields an error estimate of around 1 nm on each data point (i.e. around $0.03 \text{ nm Hz}^{-1/2}$). This is in agreement with the estimate from comparing y positions.

2.5 Discussion

The stereomicroscope described in this chapter provides both quantitative data and qualitative depth perception when looking at the micron-sized objects in an optical tweezers system. There is a trade-off here between presenting a natural view of the sample (requiring a physiologically appropriate separation angle of $\approx 10^\circ$) and attaining the highest possible particle track-

ing accuracy (where a larger separation angle is desirable). The separation angle of 72° used here was chosen to maximise accuracy at the expense of aesthetics. This gives axial tracking with a resolution only 1.4 times less than the lateral resolution, enabling nanometre precision in tracking beads. This is the primary advantage of my approach over the projector-based approach of Dam *et al.* , where a much smaller numerical aperture and separation angle were in use and hence the axial position error was much higher.

Axial tracking range is limited by the depth of field of the imaging system, which in this case is of order $10\ \mu\text{m}$. This can be varied by changing the effective NA of the images, either by varying the size of the Fourier plane apertures, or by changing the distance of the fibres from the sample. The use of plane wave illumination, such as that used in digital holographic microscopy, would enable much better depth of field whilst retaining the speed and simplicity of stereoscopic imaging. However, longer depth of field is not always desirable; in crowded samples it can result in a much less uniform background, which interferes with accurate particle tracking. The axial range over which an object can be seen is set by the NA of the bright-field illumination and the 3D pattern formed by light scattered from that object. Typically, this gives a higher value than that expected for a point source given the NA of the objective [130]. Thus, the depth of field in this system is similar to that obtained with the same objective lens in standard bright-field mode, typically around $10\ \mu\text{m}$.

The apertures in the Fourier plane perform the important function of making the point spread function more symmetric in each image, at the expense of reducing the resolution of the images, making sub-micron objects harder to track. Without the apertures, particles near the microscope's focal plane look asymmetric, an effect which increases as the separation half-angle α is increased. This effect is simply understood if we consider the scattering cross-section of a bead, as shown in Figure 1.15. If the illumination and imaging are both on-axis, we are taking a horizontal slice through an axisymmetric pattern. However, the stereo illumination means that this scattering

pattern is now skewed with respect to the axis, and consequently our slices through it (which are still horizontal) no longer produce symmetric images. Artificially reducing the NA of the system with apertures blurs out this effect at the expense of resolution, but this is not the only Fourier filter that could be used. The same re-imaging system can also implement dark-field imaging [133], which has a simpler scattering cross-section that may be more symmetric when tilted, as well as providing better contrast for small objects. Alternatively, more sophisticated image analysis could be used to exploit the elliptical shapes found in the off-axis bright-field scattering pattern rather than assuming circular symmetry.

The primary benefit of removing the apertures is increased light throughput for high speed imaging, but the system as presented here can already image at up to 10 kHz. A better model of the imaging system may also improve the range over which we can track particles with good linearity, perhaps improving performance for tracking asymmetric particles such as tools. The resolution of the imaging system also ultimately limits the precision with which particles can be tracked. However, the Cramer-Rao bound (a limit derived from information theory) places this constraint at the sub-nanometre level for a 3D PSF not dissimilar to that of the system described in this chapter [62, 134].

The particle tracking method used is free from lengthy calibration steps and does not require a threshold setting as it works for both bright and dark beads. This is due to the symmetry transform, which it uses to track symmetric objects regardless of appearance. This transform is extremely efficient, providing kHz speeds without requiring GPU processing or other detailed optimisation of the code. Tracking particles in 2D using video microscopy and a cross-correlation function would allow one to follow non spherical objects such as biological cells or micro-tools [75, 114, 135]. This could be applied to images from a microscope such as ours, enabling 3D tracking of the position and orientation of complex objects.

Robust tracking of multiple objects in three dimensions is a key challenge

in the use of optically actuated tools [115]. Tracking multiple points on an extended probe allows the recovery of its orientation as well as its position, giving access to all six degrees of freedom of a rigid body. Combined with the fast holographic control described in the next chapter, this technology has enabled feedback control of extended tools [118] to be extended to three dimensions. Stereo tracking will be used to enable faster 3D contact imaging with optically trapped probes, extending previous work using 2D tracking [117]. The stereoscopic system described in this chapter has also been used to provide 3D stiffness measurements when optimising a trapping system for metallic nanoparticles [136], and to observe particle stacking and guiding in Mathieu beams [137].



Chapter 3

Fast holographic control

Closed-loop control is a mainstay of modern engineering; the availability of effective sensors has enabled more precise control of systems as diverse as Compact Disc players and high-end fighter jets. When using holographic optical tweezers as a tool to perform delicate operations on the micron scale, the ability to sense and react to the forces involved in real time is crucial to achieve good dexterity. In particular, optical traps are often much less stiff axially than they are radially [15,85] and the ability to compensate for this would improve tasks where the particle must be constrained axially. Faster SLMs and my work on high-speed hologram generation means holographic optical tweezers systems are now fast enough to reach these goals [54].

Various techniques have been used to effect feedback control over optically trapped objects, often in a bid to reduce the effect of Brownian motion. Most commonly, galvanometer-driven mirrors or Acousto-Optic Deflectors (AODs) have been used in conjunction with Quadrant Photo diodes (QPDs)

to provide high bandwidth feedback [138, 139]. These are extremely effective in the x - y plane, however most AOD systems provide no method of controlling z . 3D control of a laser focus for multiphoton microscopy has been demonstrated using four custom AODs [38], however this has yet to be applied to optical tweezers due to its extremely low efficiency (a few percent).

Other actuators such as piezoelectric nanopositioning stages [140] or modulating the intensity of the trapping laser [7] have also been used, though these approaches have not proved effective for position-clamping (they were used to ensure a constant force was applied by the trap). Many such feedback systems are used in biological experiments [3], where position or force feedback control can help prevent damage to biological specimens or increase measurement sensitivity. Closed-loop control of HOT has been demonstrated for slowly varying biological forces [141], however the performance of such a system has not been discussed for a bandwidth of more than 0.2 Hz. Typically the SLM can only be updated at a few tens of Hertz and has a response time of tens of milliseconds, meaning that the system is unresponsive at the short time-scales required to reduce thermal motion. Recently, intensity modulation was used to cool a particle trapped in a vacuum to milliKelvin temperatures [142]. This system is extremely powerful and did work in 3D, however its experimental complexity makes it difficult to envisage as a tool, and it would be prohibitively difficult to extend to multiple traps.

Recent improvements in the speed of liquid-crystal based SLMs combined with modern camera technology [68, 96] mean that holographic optical tweezers are now able to react to a particle's motion in a few milliseconds. In addition to axial servocontrol, tracking the position on a camera allows multiple particles to be tracked and servocontrolled, a significant advantage over QPD-based systems. Measuring the trapped object's position with a camera is also inherently suited to position-clamping, as it measures the absolute position of the particle rather than its displacement from the (rapidly moving) laser spot.

As described in Chapter 2, stereomicroscopy allows us to measure the

axial position of particles and thus exploit the unique 3D capabilities of HOT to position-clamp in three dimensions [55]. This allows much more complex trap configurations to be used with feedback, for example a tool or probe controlled by multiple traps [75, 114–116, 118].

Increasing the rate at which trap positions can be updated also improves the responsiveness of the holographic system when manipulating objects. This results in smoother motion, and increases the speed at which traps can be moved before trapped particles are dropped due to the distance between successive trap positions being too large. This responsiveness is particularly important if the system is to be used with a force feedback interface, or if force measurements are to be made as the traps are moved. Large steps while moving particles (a consequence of a low update rate) can result in artefacts in the recorded force data, and can destabilise a force-feedback system (which is in effect a kind of servocontrol, where the operator forms a part of the control loop). Increasing the update rate of the SLM minimises these artefacts, however it is important to take them into account when making precise force measurements at the same time as moving the traps.

3.1 GPU hologram calculation

In order to suppress the motion of a particle as much as possible, it is desirable not only to be able to calculate holograms at the update rate of the SLM, but to be able to generate them in the minimum possible time to minimise latency τ_{lag} . To this end, I have implemented the well-known non-iterative algorithm based on direct superposition of wedges and lenses [33] in OpenGL Shader Language, which runs on the system's graphics processor.

An optical Fourier transform transforms the expanded beam incident on the SLM into a diffraction limited spot. Thus, to produce a single spot we can use the simple analytic expression for a plane wave given in Section 1.2.3. To maximise the speed with which holograms are generated, the OpenGL hologram engine then simply superposes the complex fields from each spot, again

as described in Section 1.2.3. Iterative algorithms are often used to optimise the hologram, which is particularly important for large arrays, however in this case the improvement in speed outweighs the imperfections in the holograms produced. The vast majority of these iterative algorithms optimise the relative phases of the spots [45] (i.e. they add a constant phase shift term to each spot). It is therefore possible to use such an algorithm to optimise the phases in a separate, slower process and use the optimised phases with this simple algorithm if efficiency or uniformity become limiting factors. The OpenGL code accepts a phase parameter for each spot, to allow this to be done. Randomising these phases leads to significantly improved results with regular arrays, for example the Shack-Hartmann arrays projected in Chapter 4. Randomising the positions of the traps in the array also breaks the symmetry and goes a long way towards decreasing ghost spots and improving uniformity [49]. In a system where each trap is being moved in response to independent Brownian motion, one would expect this inherent “jittering” to be sufficient to make iterative optimisation less important.

Driven by the demand for realistic 3D graphics, modern GPUs have a large number of processing cores (112 for the nVidia GeForce 9800 GT used for much of the work described in this chapter), which can execute custom “shader programs” during rendering. This has previously been used to calculate $\phi_i(x, y)$ as arrays and then to sum the arrays [143], however I have used a single custom shader to allow the entire algorithm to be executed in parallel. This implementation evaluates the summation of the holograms from each spot (1.1) using one loop over i (the spot index) for each pixel, rather than calculating ϕ_i as an array for each spot and summing afterwards. This reduces the memory requirements of the algorithm dramatically, which removes a significant bottleneck from the system’s performance. The flowcharts in Figure 3.1 show the two possibilities together with the memory requirements. Combined with the OpenGL environment which allows rendering directly into the framebuffer, this means the holograms can be calculated without writing or accessing large arrays and can be rendered directly into

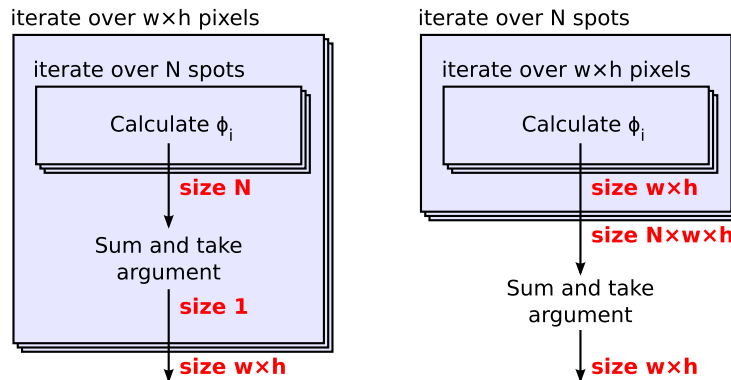


Figure 3.1: Flowcharts of the hologram calculation algorithm, showing the memory required to calculate a hologram $w \times h$ pixels in size with N spots. The left hand flowchart iterates over pixels first, then has an inner loop that calculates the contribution from each spot and sums them. The outer loop can be trivially parallelised, and the whole algorithm requires only slightly more memory than the output framebuffer. The right hand flowchart reverses this order, as has been done in a number of previous implementations [43, 143], requiring an entire frame of memory for each spot. Even if optimised to re-use memory, the large number of memory accesses is prohibitively slow.

the framebuffer in a single pass. This is a significant advantage over nVidia’s more flexible CUDA environment where the hologram must be calculated as a large array then re-rendered from texture memory to the frame buffer. The OpenGL program takes less than a millisecond to calculate and display a hologram, allowing us to achieve sufficiently low latencies to make feedback viable.

Minimising latency also involved a detailed examination of the graphics drivers’ buffer management; in order to provide smooth 3D graphics, modern graphics accelerators use one framebuffer to hold the image currently on screen and another to hold the image which is currently being rendered. These buffers are swapped when the GPU has finished rendering a frame. This is often constrained to occur at fixed intervals, such that the buffer is never swapped during a “vertical retrace”, i.e. when the graphics card

is sending a frame to the monitor (or SLM in this case). This is generally desirable, as it prevents “tearing”, where the displayed image contains part of one frame and part of the next because the buffers were swapped halfway through updating the screen. However, to optimise frame rates in games most graphics cards introduce extra buffers, so that the graphics processor is never waiting for the buffers to swap. This leads to the maximum possible quality of graphics in games, but comes at the expense of several frames of latency. This can have a serious impact on the performance of a closed loop system, so the graphics drivers were set not to lock buffer swaps to screen updates. To prevent “tearing”, we then use a second process rendering into a very small OpenGL window to detect when vertical retrace events occur (by locking its buffer swaps with the screen update) and swap the buffers in the main hologram generation program between these events. This approach does not remove tearing entirely, however it does reduce it significantly, and when it occurs it is usually only the top few lines of pixels which are affected. An oscilloscope was used to probe one of the bus lines to the SLM, which allowed us to verify that the tearing was reduced even when operating at 200 Hz.

Aside from much higher speed and lower latency, calculating the holograms on the GPU also frees up the main processor for other tasks. This allows, for example, image processing or the user interface to be run on the same computer as hologram generation without adverse effects on speed. In fact, GPU technology has advanced to the point where mobile phones can now calculate holograms at tens of frames per second [15].

3.2 Modelling a particle in a closed-loop trap

The motion of a particle in an optical trap is well described by the Langevin equation [105]:

$$m\ddot{x} + \gamma\dot{x} + \kappa x = \zeta(t) \quad (3.1)$$

where m is the particle's mass (the inertial term $m\ddot{x}$ is small and usually neglected), x is the position of the particle, $\gamma = 6\pi\eta a$ is the hydrodynamic drag coefficient (for a sphere of radius a in a fluid with viscosity η) and $\zeta(t)$ represents the force exerted on the bead by the thermal motion of the fluid molecules. The restoring force from the optical trap enters through the κx term, which assumes a Hookean optical trap at $x = 0$ with spring constant κ . This equation also holds for y and z independently, as the model used here is separable. By taking the Fourier transform of (3.1) and using the equipartition theorem to give the power spectrum of ζ as $\gamma k_B T / \pi$, where k_B is Boltzmann's constant and T is absolute temperature, we can derive the power spectrum for x (stated in Section 1.4.3) as

$$(i\omega\gamma + \kappa)\tilde{x} = \tilde{\zeta}(\omega) \quad (3.2)$$

$$S_x = \frac{\gamma k_B T}{\pi} (\kappa^2 + \gamma^2 \omega^2)^{-1} \quad (3.3)$$

for a trap without feedback, where \tilde{x} denotes the Fourier transform of x and S_x is its power spectrum. We can modify (3.1) to include a varying trap position in the restoring force term:

$$m\ddot{x} + \gamma\dot{x} + \kappa(x - x_{\text{trap}}(t)) = \zeta(t). \quad (3.4)$$

Ideally, x_{trap} would be proportional to $-x$ and the only effect of feedback would be to increase the effective stiffness of the trap $\kappa' = k_B T / \langle x^2 \rangle$. However, each element of the feedback system (outlined in Figure 3.2) introduces latency and filtering. Latency in the system of τ_{lag} (i.e. $x_{\text{trap}}(t) \propto x(t - \tau_{\text{lag}})$) gives rise to the term $\exp(i\omega\tau_{\text{lag}})$, while the response of the SLM is modelled as an exponential decay, having the Fourier transform $1/(1+i\tau_r)$. The discrete updates of the SLM (a new hologram is displayed every $\tau_{\text{SLM}} = 5$ ms) lead to aliasing (which we neglect) and a filter term $\text{sinc}(\pi\omega/\omega_{\text{SLM}}) \exp(-i\omega\tau_{\text{SLM}}/2)$. Aliasing, represented by the term $\sum_m \delta(\omega - 2\pi m/\tau_{\text{SLM}})$, can be neglected as the power spectrum falls sharply with ω , and the sinc term acts as an anti-aliasing filter. This leads to an expression for \tilde{x}_{trap} of

$$\tilde{x}_{\text{trap}} \approx -\tilde{x} \times \tilde{f}(\omega) \text{sinc}(\omega/\omega_{\text{SLM}}/2) e^{-i\omega(\tau_{\text{SLM}}/2 + \tau_{\text{lag}})} \frac{1}{1 + i\tau_r\omega} \quad (3.5)$$

where $\tilde{f}(\omega)$ represents filtering in the control loop (which is, for the rest of this chapter, set to a constant proportional gain G). The response time of the SLM is $\tau_r = 2$ ms. Substituting (3.5) into (3.2), we can derive the power spectrum for a bead in a closed loop holographic trap:

$$S_x = \gamma k_B T / \pi \left| -\omega^2 m + i\gamma + \kappa + \kappa \tilde{f}(\omega) \text{sinc}(\pi\omega/\omega_{\text{SLM}}) e^{-i\omega(\tau_{\text{SLM}}/2 + \tau_{\text{lag}})} / (1 + i\tau_R\omega) \right|^{-2} \quad (3.6)$$

Due to the approximation made in (3.5) that aliasing in the feedback signal is unimportant, this result is only valid for cases where the update frequency of the SLM is much greater than the knee frequency of the trap; with currently available technology this restricts us to relatively weak traps or highly viscous fluids. Figure 3.4(a) shows this spectrum plotted along with experimental data for a $5 \mu\text{m}$ bead in a trap with $\kappa = 2.1 \mu\text{Nm}^{-1}$. The spectra exhibit the expected suppression of Brownian motion at low frequencies (decreasing the variance by a factor of $1 + G$), but have a resonance at a frequency of approximately $(2\tau_{\text{SLM}} + 4\tau_{\text{lag}} + 2\tau_r)^{-1}$. Control theory establishes it is impossible to achieve a broadband reduction in the system's sensitivity to error, and hence this resonance cannot be eliminated [138]. However, as the underlying power spectrum for $G = 0$ has a Lorentzian shape, the impact of the resonance on the particle's position distribution decreases as it is moved to higher frequencies; thus the improvement in effective trap stiffness depends to a large extent on minimising latency in the system.

To obtain the expected improvement in spatial localisation, we can calculate the variance of the particle's position distribution $\langle x^2 \rangle$ (and similarly $\langle y^2 \rangle$) by numerically integrating the power spectrum. For a standard 60 Hz SLM, we would not expect a significant reduction in $\langle x^2 \rangle$. However, with an SLM running at 203 Hz the improvement could be as much as 50%. The improvement for a $5 \mu\text{m}$ bead in a relatively weak holographic trap ($\kappa \approx 2.1 \mu\text{Nm}^{-1}$) is shown in Figure 3.4(b) along with experimental data, as a function of feedback gain G . It shows a reduction in $\langle x^2 \rangle$ as gain is increased, which reaches a minimum and starts to increase again. At higher

gains, the assumption in (3.6) that the restoring force is unlimited becomes invalid, as the trapping force falls off once $|x - x_{\text{trap}}| \gtrsim a$. In practice this means the bead is lost from the trap.

3.3 Experimental setup

As outlined in Figure 3.2, the trapping beam is generated by a 532 nm frequency doubled Nd:YAG laser (Opus, Laser Quantum, Stockport, UK), operating at an output power of 1 Watt). The beam's polarisation is controlled via $\lambda/2$ waveplates to maximise diffraction efficiency. The beam is expanded and directed onto a Boulder Nonlinear Systems Spatial Light Modulator (XY Series) 512×512 pixels, operating at 203 Hz, 16 bit. The diffracted beam is then sent via a polarising beam splitter cube into an inverted Zeiss Microscope (Axiovert 200). The same objective lens (Zeiss $100\times$ Plan-Neofluar oil immersion, NA 1.30) was used for trapping and imaging the particles onto a Prosilica GC640M camera. The frame rate of this camera depends on the field of view, for example a single bead can be imaged at over 1 kHz and a triangular configuration of beads about $14 \mu\text{m}$ across could be imaged at 460 Hz. Image analysis and feedback control were performed in LabVIEW running on a quad core computer, which also contained the graphics processor used for hologram calculation. A centre of mass algorithm was used for 2D tracking as described in the introduction, prior to incorporating the 3D tracking methods of Chapter 2.

3.4 Results

It is important to distinguish the addressing rate of the SLM and the speed with which a beam can be steered in practice. To measure the beam steering speed of the SLM, it was used to switch the laser spot between two positions repeatedly. The intensity at these two positions was measured using the camera at a frame rate of 1.6 kHz and is plotted in Figure 3.3. This

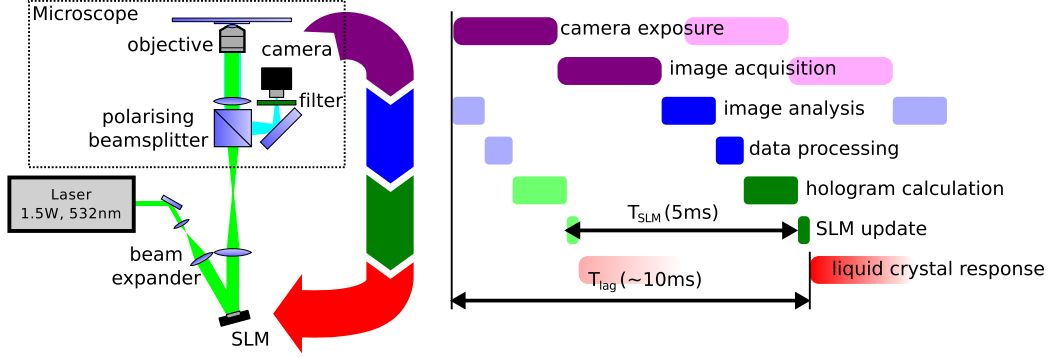


Figure 3.2: (a) Experimental setup; a 532nm laser beam is expanded then steered via an SLM onto the back aperture of the microscope objective. This same objective is then used to view the sample with bright-field illumination. The Gantt chart to the right outlines the steps in one iteration of the loop. N.B. Each iteration starts before the previous one completes, so $\tau_{\text{SLM}} < \tau_{\text{lag}}$.

shows the response to a 50 Hz square wave, and is close to the exponential approximation in Section 3.2 with a response time $\tau_{\text{R}} \approx 2\text{ms}$. The asymmetry in the response may be due to nonlinearities in the camera's response and the overall decrease in diffraction efficiency as the SLM switches from one hologram to the next.

The power spectra of a single bead's fluctuations about the target position are shown in Figure 3.4 for various values of feedback gain G . The trap had an open loop stiffness of $\kappa = 2.1 \mu\text{Nm}^{-1}$, measured by fitting a Lorentzian to the power spectrum in the case of no feedback. This had a corner frequency $f_c = \kappa/(2\pi\gamma) \approx 4.0\text{Hz}$. The response time was taken as 2 ms to match the experimentally observed response of the SLM. This left additional latency as the only parameter to fit; the best fit value was 10 ms. A good agreement is seen for low feedback gains, though at higher gains the resonance is less sharp than predicted, and there is more noise power at very low frequencies than we expect. The former effect may be due to the finite trap depth as discussed above, and the low frequency discrepancy is likely due to drift in the optical system [68]. However, the system still performs as expected, reducing the

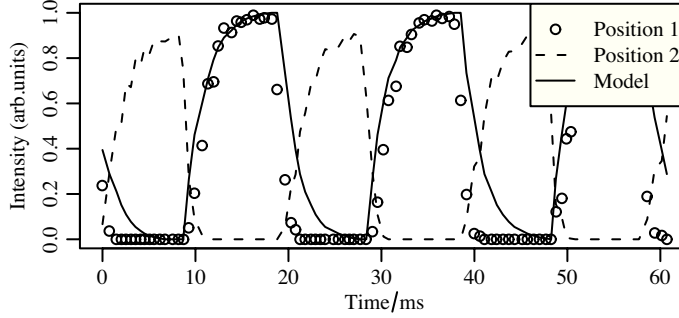


Figure 3.3: Intensity at two points, when the SLM is used to switch the laser spot between them. The solid line shows the modelled response of Section 3.2, with $\tau_R = 2$ ms.

mean squared displacement by 44% corresponding to an increase in effective trap strength $\kappa' = k_B T / \langle x^2 \rangle$ of 77%. The data shown in Figure 3.4 were collected with the high speed camera running at 1 kHz. The exposure time was close to 1 ms, and this finite exposure time acted as an antialiasing filter. The deviation from the Lorentzian curve at high frequencies arises from the noise floor of the camera system, however its contribution to $\langle x^2 \rangle$ is extremely small.

The results in Figure 3.4 are for a single particle, and could be reproduced with other techniques such as AODs. The advantage of holographic optical tweezers is that we can easily extend this to multiple particles, and to that end Figure 3.5 shows three trapped beads and histograms of their displacements from the trap centres (x and y). The variance of their position distributions was reduced by 47% on average when position-clamping was turned on. This demonstrates the unique ability of holographic optical tweezers and camera-based position measurement to perform feedback on multiple optical traps. The power spectra are also shown in Figure 3.5(c), for no feedback and for the optimal gain $G = 1.7$. These power spectra are very similar to those shown in Figure 3.4, for a single particle. This is in spite of the fact that the larger region of interest necessitated a slower frame rate for the camera of 460 Hz (c.f. 1 kHz). This shows the slower frame rate does not affect

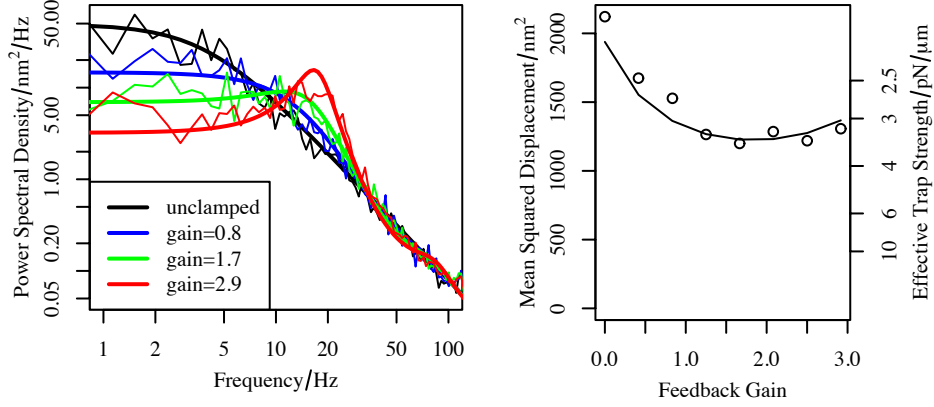


Figure 3.4: (a) Experimentally measured power spectra (points) and theoretical curves (lines) from (3.6) for a $5\ \mu\text{m}$ bead in a trap with stiffness $\kappa \approx 2.1\ \mu\text{Nm}^{-1}$. (b) The variance of the particle’s displacement as a function of feedback gain, with experimental data as points and the theoretical curve as a line. Model parameters and experimental data are the same for both plots.

the system’s performance, only the range over which power spectra can be plotted. The resonance at approximately 100 Hz is most likely mechanical in origin, though it is also possible that mains frequency fluctuations in the illumination intensity play a role. The height of the resonant peak was similar for both the $G = 0$ and $G = 1.7$ cases, and it accounted for less than 5% of the variance in each measurement. Filtering out the resonance gives a slightly greater improvement (by a few percent) in $\langle x^2 \rangle$. Other configurations of beads, such as a line, were also used and similar results were obtained.

Using stereomicroscopy to determine the bead’s axial position, it is possible to increase the effective axial stiffness by a factor of more than three. This is better performance than we obtain in x and y , which is in part attributable to the lower open loop trap stiffness in z . The power spectral density of the bead’s open loop position fluctuations follows a Lorentzian shape with a knee frequency which is proportional to trap stiffness [105]. Thus, in z (where the trap is weaker and hence the knee frequency is lower), more of the bead’s

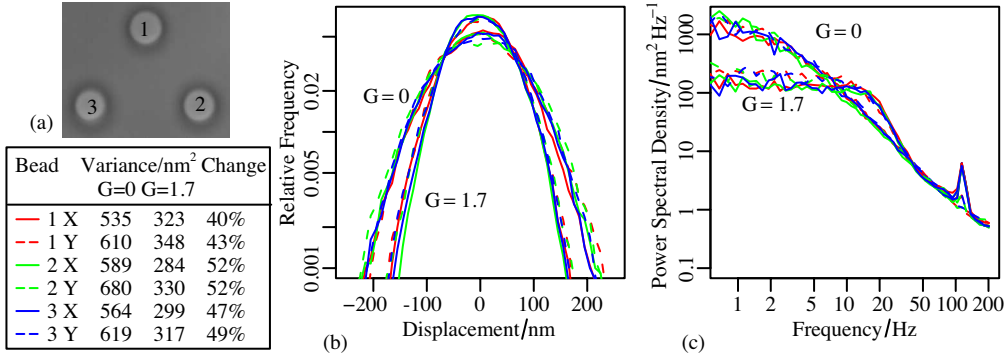


Figure 3.5: Three 5 μm beads in optical traps (a), along with a histogram of the position distributions (b) and the power spectra of their motion (c) with and without feedback. The variances with and without clamping, and the percentage decrease in $\langle x^2 \rangle$ and $\langle y^2 \rangle$ are shown in the legend.

motion is due to low frequency fluctuations which fall within the bandwidth of the feedback system. With position clamping enabled, the ratio of axial to lateral stiffness was improved from 1 : 2.9 to 1 : 1.1. The in-plane stiffness was also increased as shown in Figure 3.6. The increase in lateral stiffness is much less than that obtained with AODs, however the improvement we see agrees with the theoretical prediction given the bandwidth of the system.

3.5 Discussion

The ability to effect high-speed control over the position of the trapping laser focus makes HOT a much more responsive tool for manipulation. Calculating the holograms required to steer and multiplex the laser beam is no longer the limiting step in such a system; the slowest link in the chain is now the SLM. While the liquid crystal response time is a significant limitation, the speed with which we can transfer holograms to the SLM from the graphics card is also a potential bottleneck. Custom PCI Express interfaces can be used to sidestep graphics card limitations, at the expense of requiring much more data transfer inside the computer; Boulder Nonlinear Systems supply such an

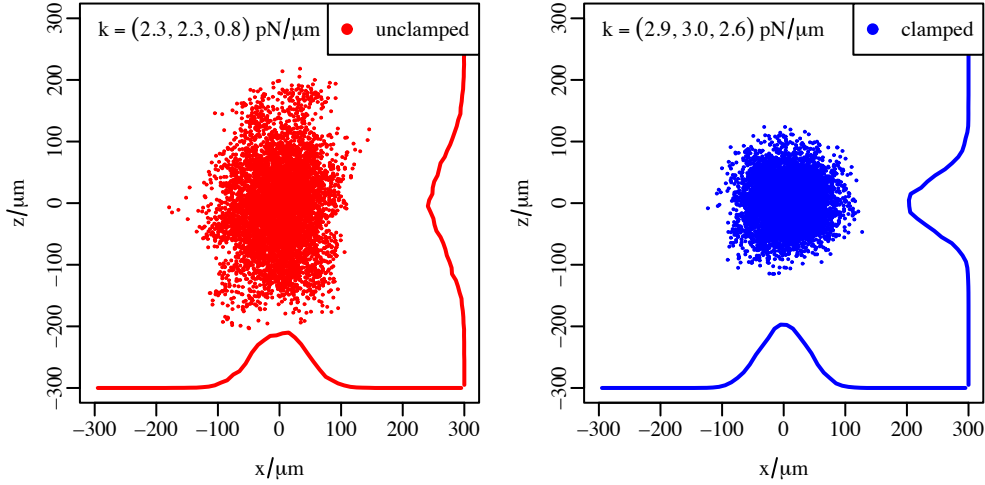


Figure 3.6: Scatterplots of a $5 \mu\text{m}$ silica bead's position fluctuations with and without position clamping, showing (x, y, z) stiffnesses for both cases. Histograms of x and z motion are shown on the graphs as lines on the bottom and right edges of the graphs.

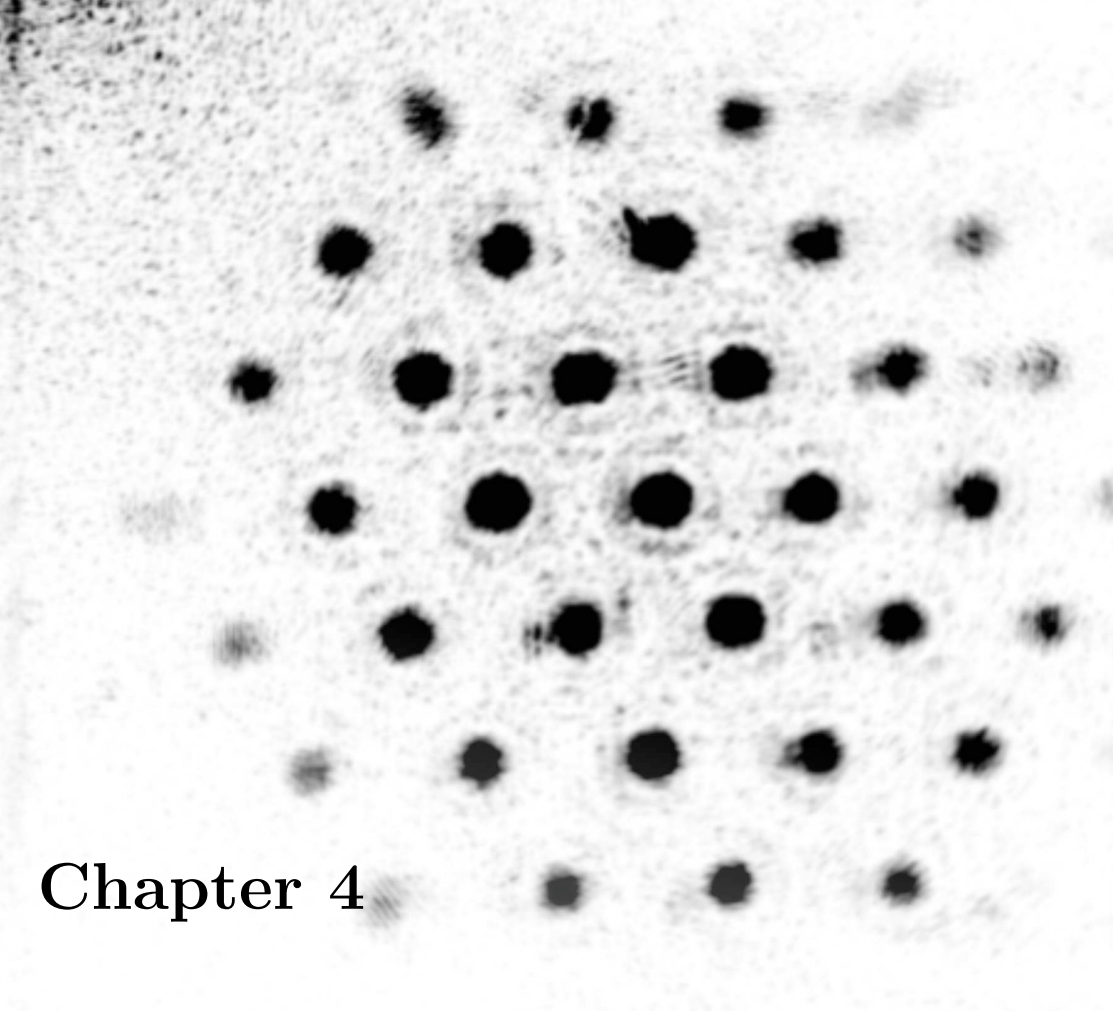
interface capable of uploading holograms at just over 2 kHz. Operating SLMs at very high refresh rates, such that the update interval is less than the crystal response time, would seem to be pointless. However, this would allow the use of transient holograms that could “overdrive” the liquid crystal and make it respond faster, a technique which is already used in LCD monitors and televisions. As computer technology continues to develop, there is no doubt that hologram generation and transmission rates will increase. Liquid crystal technology is also continually getting faster, which may one day allow SLMs to attain speeds similar to those of AODs. It is also possible to deliberately sacrifice diffraction efficiency for speed, either by using a liquid crystal layer that is too thin (i.e. cannot produce a full wavelength of retardation) or by using a different type of crystal. Ferroelectric liquid crystals typically have response times of a few hundred microseconds, but they can usually only apply a limited phase retardation, and are often restricted to binary holograms by the requirement to DC balance the control voltage (this is

necessary to avoid degradation of the crystal). It is also possible to improve matters by taking time-dependence into account when calculating holograms, for example Persson *et al.* developed a method to minimise the intensity fluctuations seen when moving spots in HOT [52].

Closed-loop feedback has great promise for overcoming many of the limitations of HOT technology, for example constraining a particle within an approximately spherical volume despite the lower stiffness shown in the axial direction by an open-loop optical trap. While the latency in the system presented here is still not low enough to reduce the Brownian fluctuations in a stiff optical trap, it can make significant contributions when working with larger objects such as multi-part tools. This is borne out in Chapter 6 with 10 μm beads in a counterpropagating geometry. There, I attained an increase in the axial stiffness of more than three orders of magnitude, when using the system at its maximum laser power (i.e. highest attainable open-loop stiffness). When using optically controlled tools, it is sometimes desirable to shape the properties of each individual trap, or of the whole trapping system, to tailor the way in which a tool interacts with the sample. Closed loop control allows much of this work to be done in software, which is easy to change, rather than by optimising the optical system each time.

Acknowledgements

The initial, 2D implementation of this system was done jointly by Dr. Daryl Preece (then a PhD student in the Optics group) and I. Daryl's contribution was the camera and particle tracking subsystem, and the control logic in LabVIEW was jointly written between us. My responsibility was the OpenGL hologram generation, and interfacing to the prototype Boulder Nonlinear Systems spatial light modulator. The subsequent 3D implementation of the system is entirely my own work.



Chapter 4

Aberration correction

One of the great advantages of SLM technology is the freedom to create arbitrary phase structures. This means that we are not limited to beam steering, but we can use the SLM to improve the performance of our optical system by cancelling out aberrations due to imperfections in the optical elements or their alignment. Indeed, we can use the SLM to synthesise a wavefront sensor which allows us to determine the phase pattern that will cancel out said aberrations, as described in this chapter.

Shack-Hartmann wavefront sensors were inspired by a method for aligning and optimising telescopes [144], where an array of holes was inserted into the pupil plane and the distortion of this array revealed aberrations in the telescope. Modern Shack-Hartmann sensors employ an array of lenslets to focus a collimated beam into an array of spots. The displacement of each spot is proportional to the tilt of the wavefront at that point, and the resultant tilt information can be integrated to recover phase information. Wavefront

sensors are also used in microscopy and ophthalmology [145–147] to improve imaging in conjunction with adaptive optic elements, particularly deep in the sample [148]. The lenslet arrays employed by Shack-Hartmann sensors have been used to create arrays of optical tweezers [149]. Conversely, the SLM found in a holographic optical tweezers system can be used as a Shack-Hartmann wavefront sensor, as described in this chapter [74].

Considerable attention has been paid to the estimation and correction of aberration in SLM-based optical systems, as diffraction limited performance is particularly important when trapping small particles or creating sophisticated optical landscapes. Methods include adding manually adjusted superpositions of Zernike polynomials to the hologram [72], interfering subdomains of the SLM with undiffracted light [73, 150], and iteratively optimising a Laguerre-Gauss doughnut mode [151]. Discrete Shack-Hartmann sensors have also been used to estimate the wavefront distortion in HOT [152]. In HOT, the SLM is generally imaged onto the back aperture of a microscope objective, such that a plane wave from the SLM is focused to a point in the sample.

In order to recover the wavefront shape, the SLM is segmented into an array of circular apertures, each of which displays a different blazed diffraction grating. Each aperture is then focused by the Fourier transform lens into one spot in the array as shown in Figure 4.1. Each spot is from a different part of the SLM. By observing the distortion of this array, we are able to estimate the tilt of each region on the SLM. The tilt information can then be used to estimate a phase map of the aberration that is subtract from the hologram to correct the wavefront. The displacement of the spots is relatively large, allowing some analysis of the image by eye. Automated analysis simply requires tracking the spots, so a correction hologram can be estimated from a single image of the spot array.

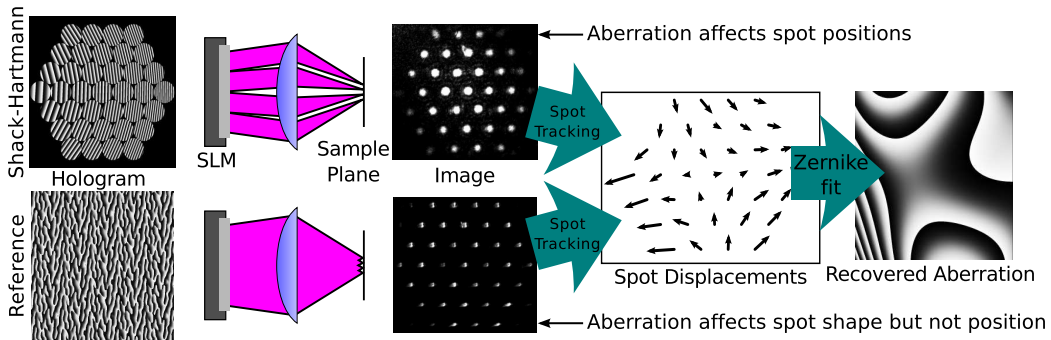


Figure 4.1: Schematic of the SLM-based Shack-Hartmann sensor showing the reference array and the Shack-Hartmann wavefront sensor. The displacement of the spots between the two patterns can be used to recover the wavefront. Relay optics have been omitted for clarity.

4.1 Hologram Design

Using the “Red Tweezers” control software, incorporating the fast hologram generation described in Chapter 3 [153], I construct a hologram consisting of an array of apertures. Each circular aperture contains a blazed diffraction grating of different pitch, such that each grating focuses to a different point in the focal plane, shown in Figure 4.1. The hologram does not have curvature and so is not a lenslet array as used in the “Adaptive Shack-Hartmann Sensor” [154, 155]. Instead, it uses the objective lens to focus the light and simply displaces the focal spots from each of the apertures, similar to the displacement of images for the scene-based adaptive optics method in [156]. The correction can thus be performed *in situ*, without modifying a standard HOT set-up. Each spot in this array has a reduced Numerical Aperture (NA), as it comes from a different part of the back aperture. Previous work has used an SLM in a different plane, such that each spot comes from a different part of the SLM but still fills the whole back aperture [157].

It is also possible to create an array of spots where each spot comes from the whole SLM [45] as shown in the “reference” array in Figure 4.1. In this case, smooth aberrations will primarily affect the shape of the spots

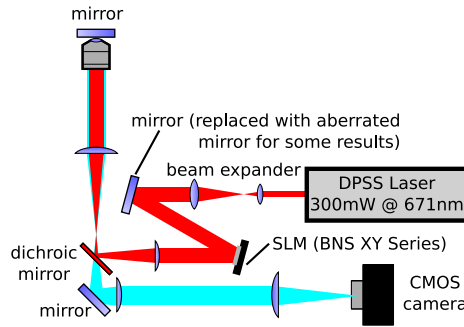


Figure 4.2: The optical system used in the experiment.

and not the geometry of the array. This provides a very simple way of generating a reference image, and greatly simplifies the set-up of this system. Taking the displacement of each spot in the Shack-Hartmann array from its corresponding spot in the reference image removes artefacts resulting from inaccuracies in the placement of the regions of interest on the camera, etc.

4.2 Optical System

The experiment was performed in the holographic optical tweezers system shown in Figure 4.2. To image the sample plane, the microscope slide was replaced with a mirror. For some experiments, additional aberration was introduced by using an aberrated SLM as a mirror. The aberrated SLM was switched off and placed just after the beam expander, replacing a mirror. This “aberrated mirror” introduced around three wavelengths (peak to peak) of aberration, which is not unreasonably high for an SLM [158]. As the beam was collimated by adjusting the beam expander, defocus would have been removed, leaving astigmatism as the predominant aberration [159].

It was also possible to image the reflection of the array from the coverglass-water interface in a sample, however the reflection of spots from different parts of the array was not uniform. This is due to the Fresnel reflection coefficient varying as a function of incident angle and polarisation, and was improved by the use of circularly polarised light. The reflection was also

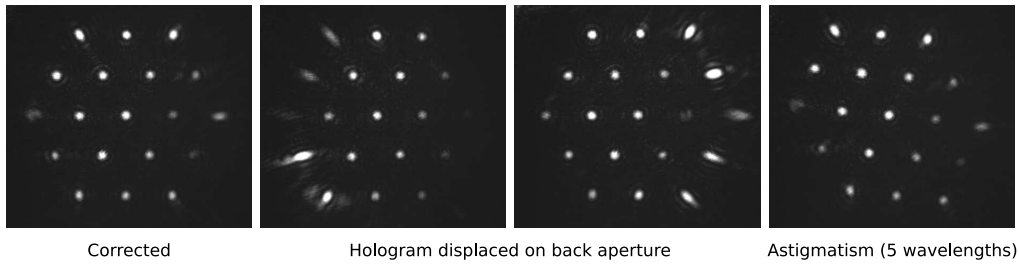


Figure 4.3: Images of the Shack-Hartmann array reflected from a coverglass-air interface.

relatively faint as the refractive index difference of a glass-water interface is less than 0.2. To improve this without sacrificing experimental convenience, an empty sample cell was used, replacing the glass-water interface with a glass-air one, which greatly increased the brightness of the reflected image. This also ensured that aberrations due to the coverslip were present. While it should not be significant when using an index-matched oil immersion objective, the coverslip introduces spherical aberration in water immersion objectives and it is thus important to include it when making corrections.

The array of spots was quantitatively analysed using LabView and National Instruments' Vision library. An image of the sample was split into an array of sub-images matching the array of spots. For each sub-image, a threshold function was applied and the centre of mass of the spot calculated. To cope with varying brightnesses of the spots, the threshold for each sub-image was scaled by the maximum brightness in that region. The spot displacements were then analysed by fitting a linear combination of the first 15 Zernike polynomials to recover a phase map of the aberration. This recovered phase map was then subtracted from the hologram on the SLM to correct for aberration.

4.3 Results

Arrays of spots were projected into the sample using the SLM as described. Some images of the Shack-Hartmann array are shown in Figure 4.3. This

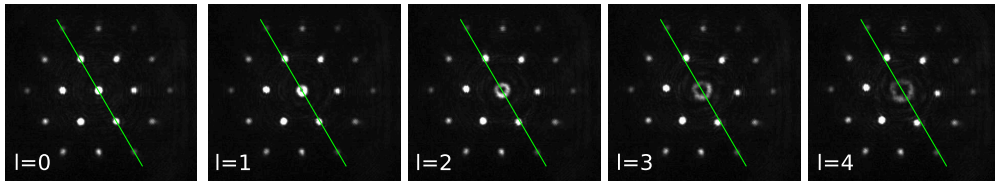


Figure 4.4: Images of the Shack-Hartmann array when a helical phase term is added to the SLM. The green line is at the same angle in each image, as a reference for the distortion of the array. The spots “twist” around the central spot as helical phase is added to the SLM, with the optical singularity at the centre of the SLM showing up as a distortion of the central spot into an annulus.

also shows distortion of the array by misalignment of the hologram with the back aperture and by the presence of astigmatism. The array can therefore be used as a tool for aligning the system even without automated analysis. To illustrate the sensitivity of the technique, Figure 4.4 shows images taken with helical phase added to the SLM. Even for an additional shift of one wavelength around the SLM, distortion of the array is visible by eye.

The system was initially corrected for aberrations arising from the beam expander and SLM (the aberrated mirror was not used). This correction was performed with the spot pattern reflected from both a mirror and a coverslip, and the results are shown in Figure 4.5. There are some differences in the Zernike coefficients obtained when using the mirror and the coverslip, however the correction hologram generated using the mirror still leads to a marked improvement in the spot size on the coverslip. The largest aberration term is astigmatism, as has previously been reported [72, 159]. The RMS deviation from flatness was about 0.35λ , and the RMS difference between the two holograms was 0.12λ .

An aberrated mirror before the SLM was then used to degrade the beam quality in the system, and the Shack-Hartmann sensor was employed to correct the resultant, larger aberrations. Figure 4.6 shows images of the focal spot as a mirror is scanned through the focus, demonstrating the much im-

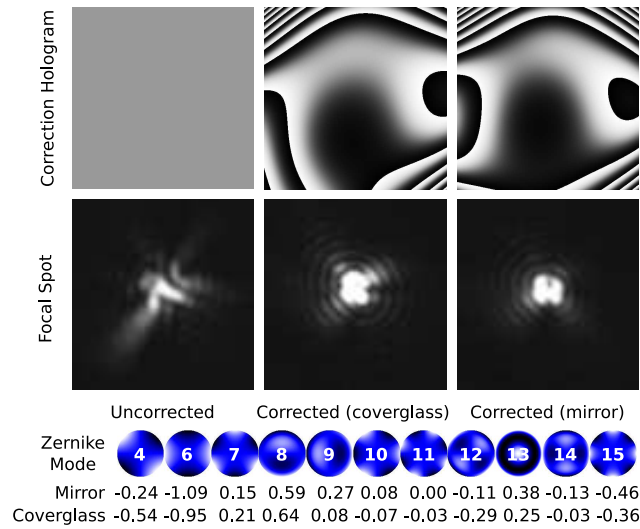


Figure 4.5: Images of the focal spot before and after correction. All images are reflections from a coverglass-air interface. Also shown are the Zernike coefficients recovered by the two corrections, in wavelengths peak-peak.

proved point spread function, along with the phase map of the recovered aberration. To further verify the improvement in beam quality, I used the system to trap 800 nm silica beads. Figure 4.7 shows scatterplots of a beads motion over 15 seconds in traps with and without the correction applied. The bead was tracked using the stereomicroscope described in Chapter 2. The trap strengths in x , y and z as estimated from the position fluctuations were increased by a factor of more than four, from 0.95, 3.1, 0.33 to 11, 11, 1.4 μNm^{-1} . This is much greater than that seen in [72] but is significantly less than that estimated in [152] (for a larger aberration than we see here). The aberration (about 3 wavelengths, dominated by astigmatism) was typical for a HOT system. This experiment was repeated with 2 μm beads and a much less dramatic improvement was observed, due to the larger beads decreased sensitivity to spot shape. However, when using Laguerre-Gauss modes to trap the 2 μm bead [14], the system did benefit from the correction.

Quantitative measurement of the sensitivity and range of this method is

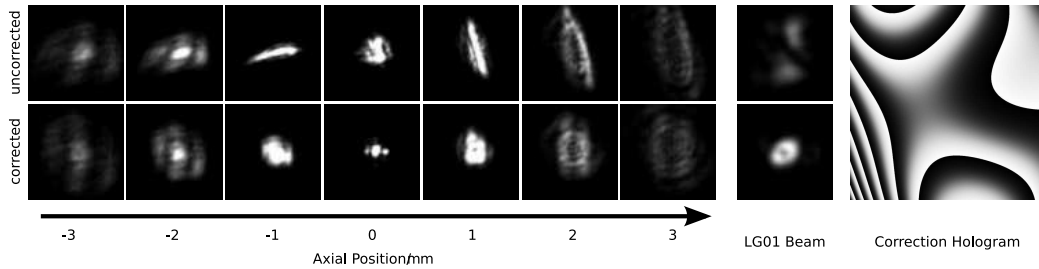


Figure 4.6: Point spread function before and after correction. Laguerre-Gauss 0,1 modes are also shown, as a sensitive indicator of aberrations. Zernike coefficients for the correction are $(-0.91, 1.52, 0.55, 0.26, -0.46, -0.22, -0.01, -0.02, 0.05, -0.04, -0.13)$, for the modes given in Figure 4.5.

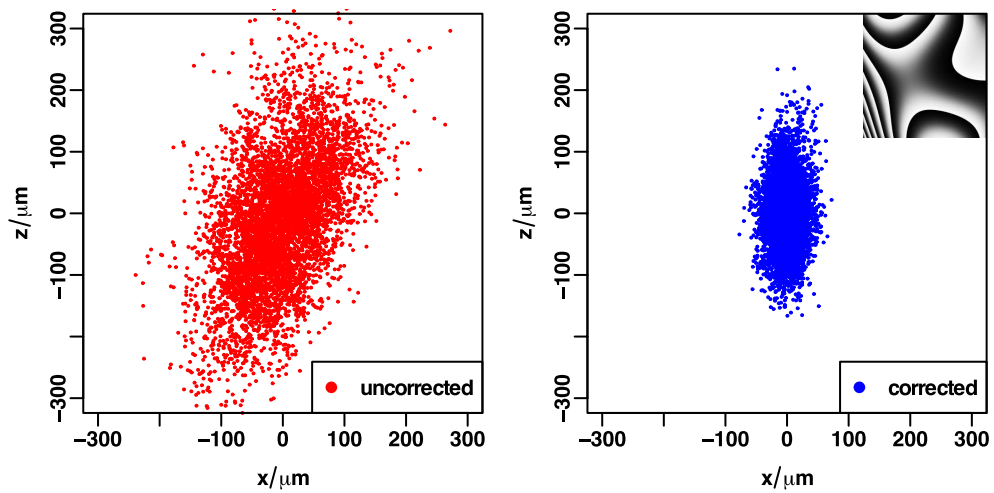


Figure 4.7: Scatterplots of an 800nm silica bead trapped in the laser focus with and without the correction applied.

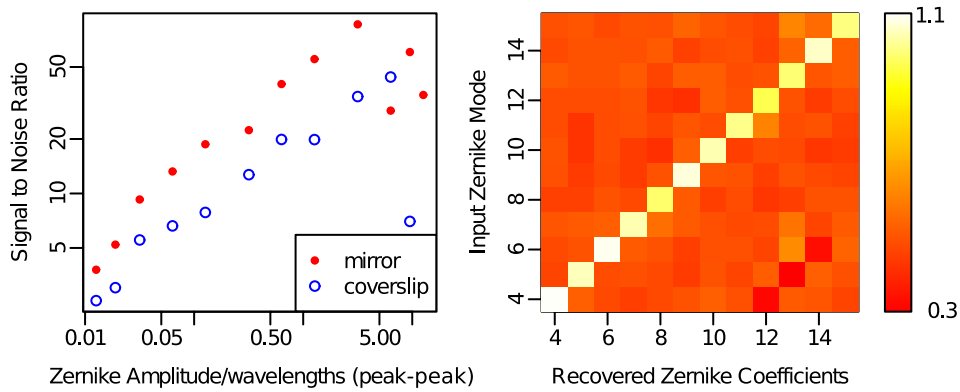


Figure 4.8: Recovered Zernike coefficients when individual Zernike modes are deliberately added to the system, and signal-to-noise ratio for different severities of aberration. The right hand plot shows the aberration measured when a small amount of each Zernike mode is added to the hologram. This was repeated for different amplitudes of distortion, and the resultant signal to noise ratio is plotted on the left. The smallest distortions that can be detected are around 0.01 wavelengths peak to peak, and the sensor starts to fail for aberrations that are more than about 5 wavelengths peak to peak. Mode numbers are the same as Figure 4.5.

possible by looking at known aberrations. The different Zernike modes used in correction were displayed on the SLM in addition to the Shack-Hartmann hologram, and the resultant wavefront was measured. This should give a response where all coefficients are zero except the one displayed on the SLM, so the ratio of the displayed mode to the background modes indicates how well the sensor is performing. This is shown for each of the 12 modes used in Figure 4.8. By plotting the signal-to-noise ratio (SNR) against aberration strength, we can determine the smallest detectable aberration. This is a few hundredths of a wavelength peak-peak, however imperfections in the mirror or imaging lenses will introduce systematic errors not detectable by this method. Aberrations of around 10 wavelengths peak-peak could be measured, after which the spots deviated from their assigned regions of interest.

4.4 Discussion

In this chapter, I have demonstrated the use of a Spatial Light Modulator as a Shack-Hartmann type wavefront sensor. The same SLM is also used to correct the wavefront in a closed-loop adaptive optics system. The advantage of this technique compared to other methods lies primarily in its ease of use and robustness; two images (sensor and reference) are sufficient to estimate errors in the system, with only one scaling factor remaining to be determined (the scaling between spot displacement and wavefront tilt). This is simple to determine experimentally, or can be calculated with geometric optics. The optical system is the same as that usually found in holographic optical tweezers.

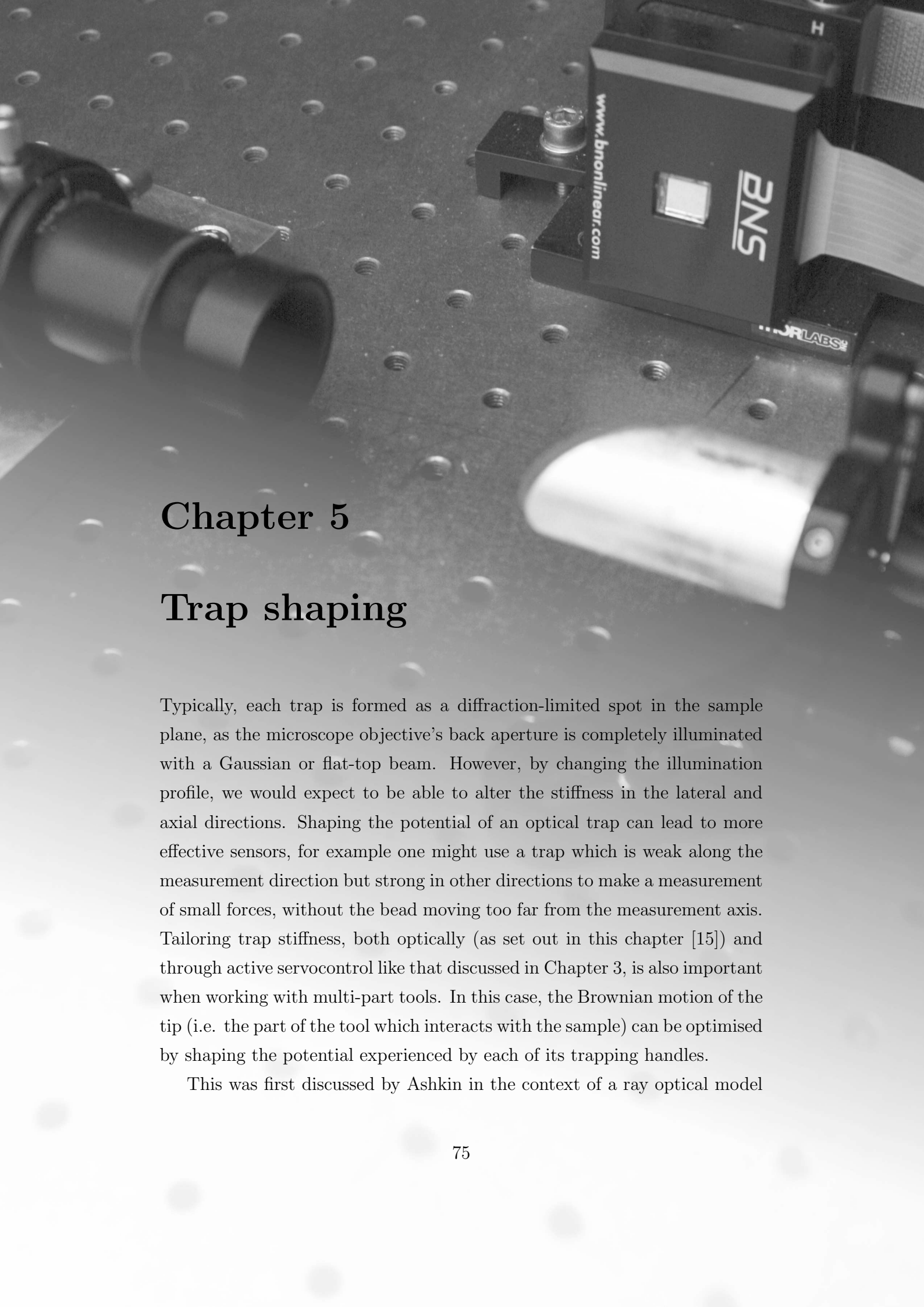
Diffraction places the most restrictive limit on this technique; the size of each spots in the array is inversely proportional to the size of the aperture corresponding to that spot. To access higher spatial frequencies, more sub-apertures are needed, corresponding to smaller apertures and larger spots. The spots must be separated from each other on the camera, which places an upper bound on the number of apertures that can be used. This in turn limits the maximum spatial frequencies which can be detected and corrected for. Focusing through turbid media, which has been achieved using interferometric techniques [73, 150] is therefore not feasible with a Shack-Hartmann sensor. However, the system is much faster than the interferometric techniques, and is robust in the presence of large but smooth aberrations, meaning it succeeds in cases where the iterative approach of Jesacher *et al.* [151] would not converge.

Projecting the spot pattern onto a mirror (or other reflecting surface) in the image plane is a very convenient method, however it is sensitive to aberrations in the mirror, and aberrations between the mirror and the camera can affect the wavefront recovered. As the area occupied by the spot pattern is only a few tens of microns, I would not expect flatness to pose a major problem. However, the double-pass through the objective means that aberrations relating to the objective (and other imaging optics) may not

be estimated correctly. This could be circumvented by using a fluorescent sample, such that the light returning through the objective was diffuse. A fluorescent sample would also allow the measurement of spherical aberration (and other aberrations) due to immersion media, etc. which are currently not detectable as the reflection is from a plane in front of the sample.

Aberrations as small as a few hundredths of a wavelength are detectable by this method, though drift and systematic error from the imaging optics mean this should be regarded as a lower bound. The difference between the corrections estimated looking at reflections from a coverslip and from a mirror was about 0.12λ RMS, which gives an idea of the accuracy obtained in practice. The maximum aberration measurable is currently limited by displacement of the spots beyond their regions of interest on the camera. Reducing the number of spots [155] or using a more sophisticated spot tracking algorithm [160] would extend the range even further than the ten wavelengths reported here.

Computer analysis of the spot pattern is not the only way in which this technique can be used; looking at the intensity of the spots allows us to determine the intensity distribution on the SLM, or to pinpoint any clipping of the beam which is occurring. It allows for very simple alignment of the expanded laser beam onto the SLM, and of the imaging optics to relay the SLM onto the back aperture of the microscope objective. This is, in part, because the intensity of the spots is directly proportional to the illumination intensity at each aperture on the SLM. Thus, the intensity profile of the beam illuminating the SLM can be estimated, which is useful when designing holograms with the Gerchberg-Saxton algorithm [46]. This also makes it obvious when clipping of the beam has occurred, as spots are missing from the array. Carefully aligning the optics before correcting for aberrations helps to maximise the performance of the system. The Shack-Hartmann holograms in this chapter aid both alignment and correction, making them a useful tool for setting up and maintaining HOT systems.



Chapter 5

Trap shaping

Typically, each trap is formed as a diffraction-limited spot in the sample plane, as the microscope objective's back aperture is completely illuminated with a Gaussian or flat-top beam. However, by changing the illumination profile, we would expect to be able to alter the stiffness in the lateral and axial directions. Shaping the potential of an optical trap can lead to more effective sensors, for example one might use a trap which is weak along the measurement direction but strong in other directions to make a measurement of small forces, without the bead moving too far from the measurement axis. Tailoring trap stiffness, both optically (as set out in this chapter [15]) and through active servocontrol like that discussed in Chapter 3, is also important when working with multi-part tools. In this case, the Brownian motion of the tip (i.e. the part of the tool which interacts with the sample) can be optimised by shaping the potential experienced by each of its trapping handles.

This was first discussed by Ashkin in the context of a ray optical model

[12], where he noted that rays from the edges of the microscope aperture contribute more to the trap's axial stiffness (and less to its radial stiffness) than those in the centre. This means that a flat-top beam has a higher axial stiffness than a Gaussian beam of the same power, and that decreasing the numerical aperture (i.e. using only the centre of the back aperture) decreases the axial stiffness relative to the lateral stiffness. The use of Laguerre-Gaussian beams to enhance axial stiffness agrees with this ray-optical model [14], however more general control is possible by controlling the radial intensity profile at the back aperture.

Control over the optical field used to generate a trap could also make difficult-to-trap objects easier to trap, for example objects which experience a large scattering force. By removing light from the centre of the back aperture of the system, we decrease the on-axis component of the light's momentum (light propagating at an angle to the optical axis, i.e. from the edges of the back aperture, has a smaller component of its momentum along the optical axis). This in turn means that light absorbed or scattered isotropically from the particle (which has zero net momentum, and hence usually accelerates the particle along the beam axis) will exert less force. As rays at the centre of the back aperture contribute little to the axial stiffness, an annular beam could enable stable axial trapping of small, high-index particles, possibly including metallic nanoparticles.

5.1 Axial and lateral stiffness

The Point Spread Function (PSF) of even a high-NA objective lens is longer axially than it is wide. This results in a lower trap stiffness in the axial direction, as seen in Chapter 1. Different parts of the back aperture of the objective correspond to rays entering the focus from different directions, which we expect will contribute differently to the stiffness of the optical trap [12]. I have measured this using the SLM to synthesize different apertures in the back focal plane (by redirecting some of the light to the zero-order

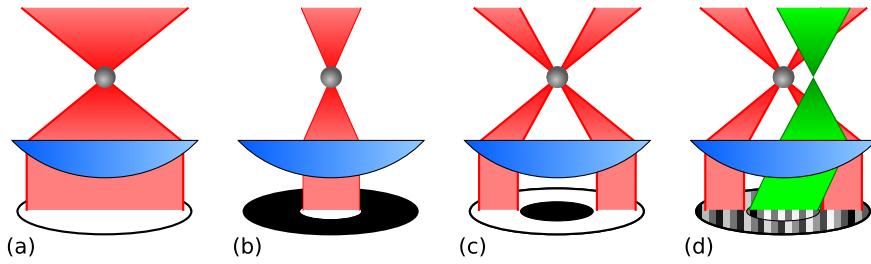


Figure 5.1: Placing different apertures in the back focal plane of the microscope objective can change the trap properties. Here we consider (a) no aperture, (b) a circular aperture that reduces the effective NA and (c) an annular aperture that blocks the centre of the back aperture. (d) As the SLM modulates phase and not amplitude, unwanted light is redirected to another point, rather than absorbed by the SLM.

undiffracted spot, effectively modulating the amplitude of the light reflected from the SLM [161, 162]). The apertures used here are either simple circular apertures (which effectively reduce the NA of the trap) or annular apertures, which block out the central region as shown in Figure 5.1.

It is possible to use non-axisymmetric intensity patterns in the Fourier plane to produce optical traps with extended shapes, such as line traps [59] (line traps result from modulation of the back aperture with a function like $\text{sinc}(k_l x)$, where k_l sets the length of the line). By varying the phase gradient along the line, it is possible to set the scattering force, for example to push beads along a line trap. For long line traps like those used in [60], even small intensity fluctuations from imperfections in the system can prevent beads travelling along at a uniform rate, however short line traps could function as constant-force springs (in contrast to the usual Hookean springs found in optical tweezers). This could be useful when working with micro-tools where one might need to maintain a constant force against a sample.

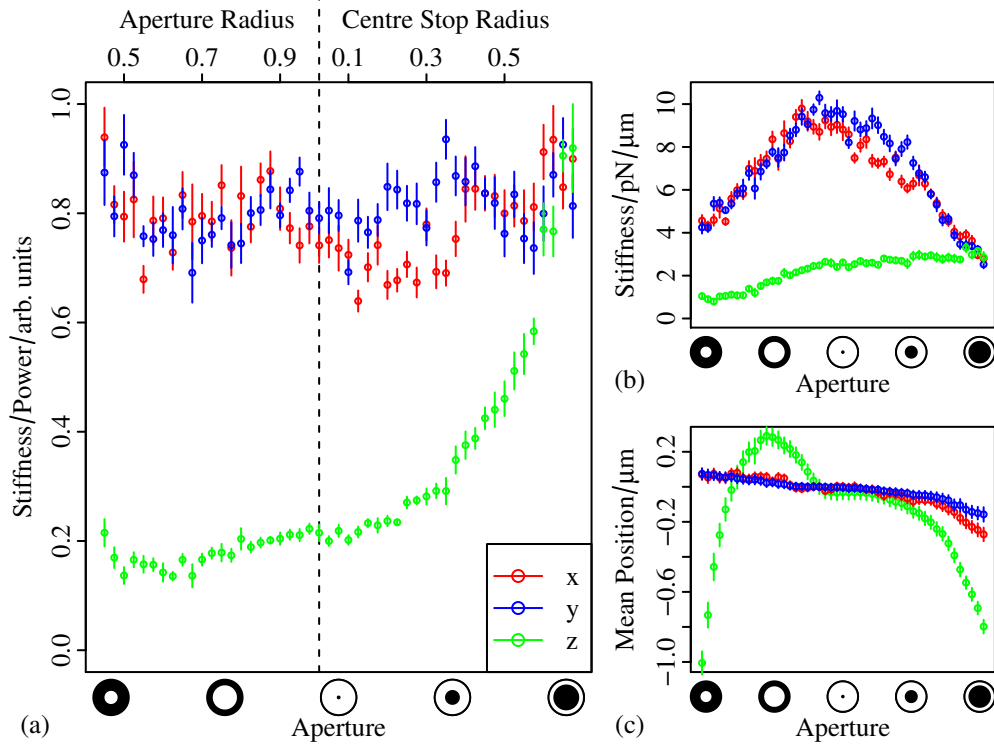


Figure 5.2: (a) Stiffness of an optical trap for a 5 μm silica bead created with various apertures at the back focal plane of the microscope objective. The values of stiffness are per unit power in the trap. On the left of the dotted line, an aperture is placed on the SLM to reduce the effective NA, and on the right a centre stop is used to block the centre of the beam. The radii of both are displayed on the top axis, as fractions of the back aperture of the microscope objective (i.e. the dotted line corresponds to no aperture). (b) The same stiffnesses for fixed illumination power. (c) Mean position of the bead when trapped with each aperture.

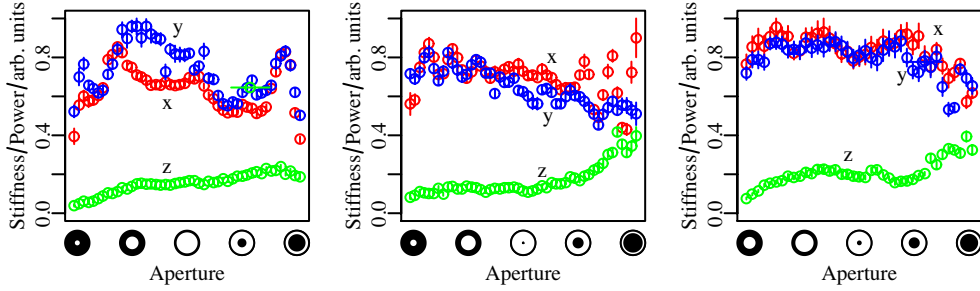


Figure 5.3: Stiffness of an optical trap with various apertures, for (a) a $2\ \mu\text{m}$ silica particle, (b) a $3\ \mu\text{m}$ silica particle, (c) a $5\ \mu\text{m}$ polystyrene particle.

5.2 Experimental results

For each particle, a progression of apertures was used. The results presented here are all for axisymmetric apertures, so we expect the variation to be between the axial and lateral stiffness. First, simple circular apertures starting at low NA and working up to full NA were applied. Secondly, the stiffness from rays near the edge of the back aperture was probed with annular apertures blocking out a small section in the middle of the beam, which was gradually expanded until the particle was lost. These apertures are shown on the horizontal axis in Figure 5.2. For each aperture, the equipartition theorem applied to the particle's position fluctuations allows us to estimate stiffness as $\kappa_x = k_b T / \langle x^2 \rangle$. This was measured over intervals of 1.5 seconds and averaged over 10-20 intervals. The resultant stiffnesses in x , y and z are plotted in Figure 5.2. Data shown here has been normalised by the power in the optical trap, so the curve represents stiffness per unit optical power in the trap (an un-normalised plot is shown in Figure 5.2(b)).

This procedure was repeated for beads with a number of different sizes and materials. Figure 5.3 shows results for $2\ \mu\text{m}$ and $3\ \mu\text{m}$ diameter silica beads and for $5\ \mu\text{m}$ polystyrene, where the same trends are visible. For the low-NA traps (left side of the graph), the axial stiffness is much lower than the radial stiffness. In this regime, the scattering force becomes more prominent, resulting in a shift of the equilibrium trapping position to further behind the

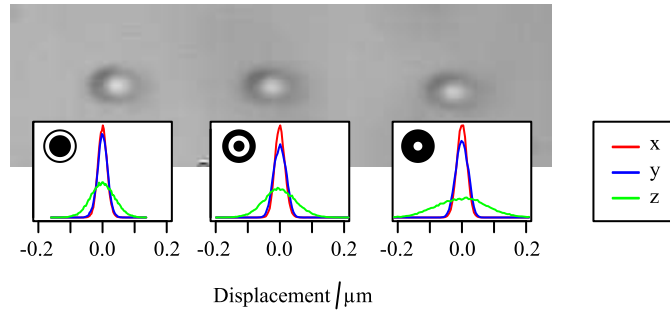


Figure 5.4: Position histograms for three beads trapped with different apertures, showing different axial stiffnesses.

focus. When ring-shaped traps are used, the axial stiffness starts to approach the radial stiffness. The scattering force has a smaller influence here relative to the gradient force, resulting in the bead's equilibrium position being closer to the focus. This effect can be seen in Figure 5.2(c).

It is possible to create multiple traps with different apertures, as shown in Figure 5.4, where three beads are trapped with different axial stiffness. If the trap configuration includes some traps with high axial stiffness and some with low axial stiffness, it is possible to make use of the whole back aperture and create the traps with high optical efficiency.

5.3 Discussion

By controlling the intensity distribution at the back aperture, the axial stiffness can be varied from nearly 0 to almost the same as the radial stiffness. This can be applied to the use of optically controlled tools and probes [75, 114, 118], for example if a one-dimensional force measurement is to be made, the trap could be made less stiff along the direction of force measurement. Similarly, when axial force must be applied to an object, a shaped trap would allow this to be done with less light used per unit force required. Compared to the active feedback in Chapter 3, it is important to note that an optically shaped trap does not involve rapidly updating the SLM. While

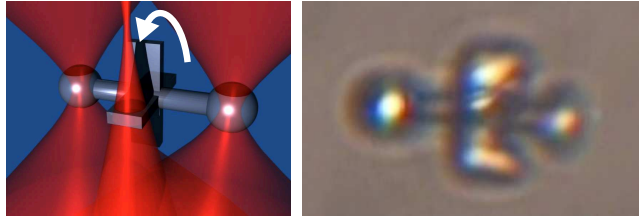


Figure 5.5: An optically trapped paddle wheel, fabricated by two photon polymerisation and driven using the scattering force [135]. This could be driven very effectively using shaped optical traps, some with high axial stiffness and some with very low axial stiffness. Photomicrograph courtesy of Asavei *et al.* [166]

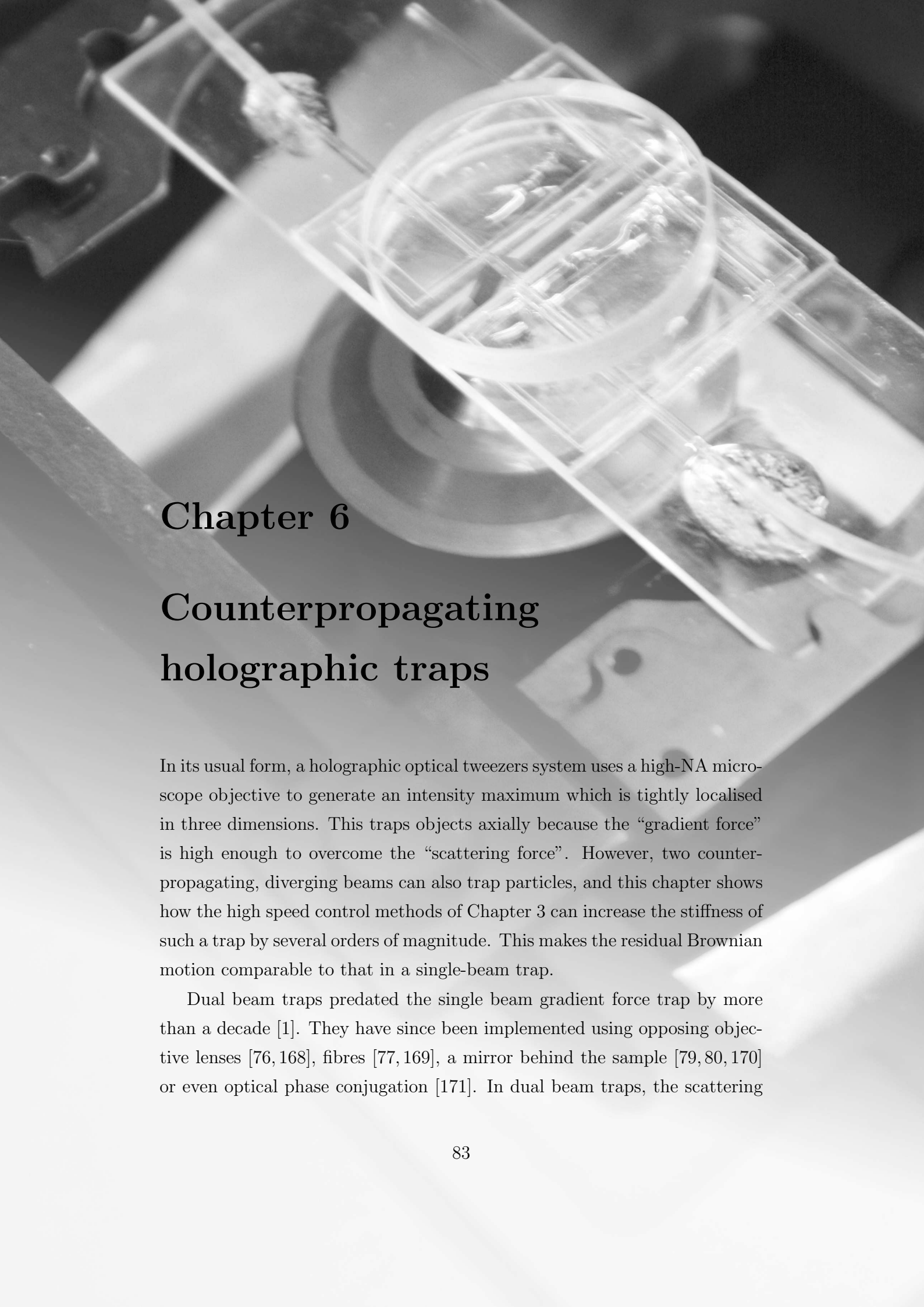
optical trap shaping cannot reproduce all the capabilities of active control, it is inherently free from noise and resonances introduced by an imperfect control loop. This is advantageous in situations where it is important not to add energy to the system, and also removes the requirement for a high speed SLM.

Traps with a small effective NA have a larger scattering force relative to the axial stiffness, which is weak due to the extended axial PSF. This is a property shared by Bessel beams [163], recently exploited to hold beads just above a surface for UV nanopatterning [164]. Using an SLM to shape the trap means that we can alter the characteristics of a trap dynamically and we are able to have multiple traps, each with a different shape. When using light to power micro-machines, for example [135, 165, 166], it can be advantageous to have some traps with high axial stiffness and some which are dominated by the scattering force (i.e. very low axial stiffness). If both shapes of trap are required, this can be done with very good efficiency. In particular, the work in [166] used an out-of-focus trap to push the blades of a paddle wheel (micrograph in Figure 5.5) with the scattering force, without trapping the blades. By using one or more low-NA optical traps, it would be possible to do this with better efficiency, while having a higher axial stiffness in the two optical traps holding the spherical “handles” on the structure, as shown in

Figure 5.5.

It is also worth noting that laser power affects the equilibrium axial position of a particle. Optical forces scale with the power of the trapping laser, while other forces (such as the particle's weight) remain constant. This can be seen in Figure 5.2(c) where the particle "sags" in the trap at the extremes of the graph, where the apertures are small and thus only a small amount of the available optical power is sent to the trap. This effect suggests that it could be possible to use an optical trap to weigh trapped particles, which will have masses in the region of 10^{-15} kg.

Optical traps having a shape other than a simple focused spot are very difficult to generate in a controlled way using any method other than HOT. Using an SLM gives an unprecedented degree of control over the wavefront, which allows us not only to correct the wavefront and regain the optimal focus (as in Chapter 4), but also to deliberately change the structure of the optical trap [167]. This is another tool available to HOT, which can easily be added without modifying any optics, and indeed can be different for each trap in a multi-trap configuration. Such tailored optical potentials should prove themselves very useful when working with extended objects that have multiple trapping points.



Chapter 6

Counterpropagating holographic traps

In its usual form, a holographic optical tweezers system uses a high-NA microscope objective to generate an intensity maximum which is tightly localised in three dimensions. This traps objects axially because the “gradient force” is high enough to overcome the “scattering force”. However, two counterpropagating, diverging beams can also trap particles, and this chapter shows how the high speed control methods of Chapter 3 can increase the stiffness of such a trap by several orders of magnitude. This makes the residual Brownian motion comparable to that in a single-beam trap.

Dual beam traps predated the single beam gradient force trap by more than a decade [1]. They have since been implemented using opposing objective lenses [76, 168], fibres [77, 169], a mirror behind the sample [79, 80, 170] or even optical phase conjugation [171]. In dual beam traps, the scattering

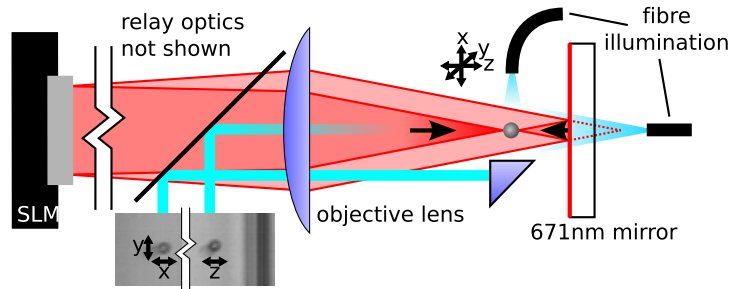


Figure 6.1: Schematic of the trapping and imaging system. The laser is split into two beams with the SLM, one of which is reflected by the mirror to form a backward-propagating focus. A right angle turning prism provides a side view, from which we can find the axial position of objects. N.B. this figure is rotated by 90 degrees compared to Figure 6.2; the optical axis is vertical in the experiment.

forces from the two beams cancel out when the particle is in the centre, and act to push the particle back when it is displaced axially. This removes the requirement for high numerical aperture, and enables the use of long working distance objectives and lower magnifications than are typically used for single beam tweezers.

The use of lower magnification objectives also opens up the possibility of manipulating larger objects [11] and of adding a side view to the system [172]. Both of these can use multiple objective lenses [1, 81], however it is also possible to use a single objective with a modified sample cell. This is done by placing a mirror behind the sample and creating focal spots in front of and behind the mirror using an SLM [79,80]. The mirror then reflects one of these to give two spots with opposite directions of propagation, as shown in Figure 6.1, and these foci can form a counterpropagating optical trap. This has been referred to as “macro-tweezers” [11] because of the much larger objects which can be trapped, and the greater working volume afforded by a low-magnification objective. By adding a prism at the side, we can use the same objective to view the sample from two orthogonal directions [11].

Counterpropagating traps can achieve very high axial forces by turning off

the upwards- or downwards-propagating beam. However, the axial stiffness is usually very low and consequently Brownian motion causes the particle's axial position to vary by as much as several microns, precluding accurate positioning or force measurement. This combination of low stiffness and high maximum force makes the system an ideal candidate for closed loop control. Applying the high speed control methods described in Chapter 3 to the macro-tweezers geometry suppresses a great deal of the particle's Brownian motion. The bandwidth of the control loop described in this chapter is an order of magnitude higher than that previously reported using a GPC-based system [81], resulting in much smaller residual motion and a greatly reduced resonance.

Position clamping in single-beam gradient traps [3,138,139,173] requires a bandwidth of many kHz to achieve a large suppression of residual Brownian motion. However, the larger objects which can be trapped in the macro-tweezers exhibit less high-frequency motion due to the greater viscous drag forces they experience. More of their motion falls within the bandwidth of the control loop, and consequently the SLM and camera can be used to suppress much more of their motion than when working with smaller objects. Also, servocontrol of a single-beam trap does not increase the maximum force available; this is still determined by the laser power and optical properties of the particle. In contrast, actively controlling axial position in the counterpropagating trap by changing the power in the upper and lower beams allows much larger forces to be used than are found for any position of the particle in the static trap.

6.1 Method

6.1.1 Optical System

Figure 6.2 shows the optical system, similar to that described in [15] but with an Olympus 10 \times , 0.2 NA objective, and a different focal length lens in front of the SLM to fill the objective's back aperture. A 300 mW, 671 nm DPSS

laser system (Roithner LaserTechnik) was used, and a corresponding band-reflecting mirror was placed behind the sample. Two fibres, similar to those in [15], were used to illuminate the sample from above and from the side. The sample cell was prepared as in [79], with a square cross-sectioned cuvette (VitroCells 8240) and a miniature right-angle prism (NT45-385, Edmund Optics). An air gap underneath the cell ensured the focal planes for the bottom and side views coincided approximately in the middle of the cell.

The fast SLM (Boulder Nonlinear Systems) runs at 203 Hz, as detailed in Chapter 3. A fast CMOS camera (Mikrotron EoSens 1362-CL) was used to monitor the position of the bead from the two viewpoints which allowed recovery of its 3D position. Image acquisition and control logic were performed in LabVIEW (National Instruments). Regions were defined on the camera corresponding to bottom and side views, then smaller regions were extracted around the trapped particles, which were tracked with a symmetry transform implemented in C as used in Chapter 2. A CameraLink Full framegrabber (National Instruments PCIe 1433) provided sufficient bandwidth to run the camera at 1 kHz with a field of view 1280×512 pixels (1.6×0.6 mm) across.

6.1.2 Control Logic

Trapped objects can be moved in z either by axially shifting the two foci or by adjusting the balance of power between the upper and lower beams, keeping total power constant. The latter method allows large forces to be exerted (by concentrating all the power in one or other beam), so we use this to effect closed-loop control. Shifting the foci allows the equilibrium position of the bead to be moved over a large axial range while keeping the foci relatively close (thus maximising the lateral force), so we use this to position the bead in open-loop mode. The foci are centred on the position set-point in closed loop mode. Changing intensities can also change the equilibrium position with fixed focal planes [81], however stable traps can only be formed between the two foci, limiting either the axial range or the maximum lateral force.

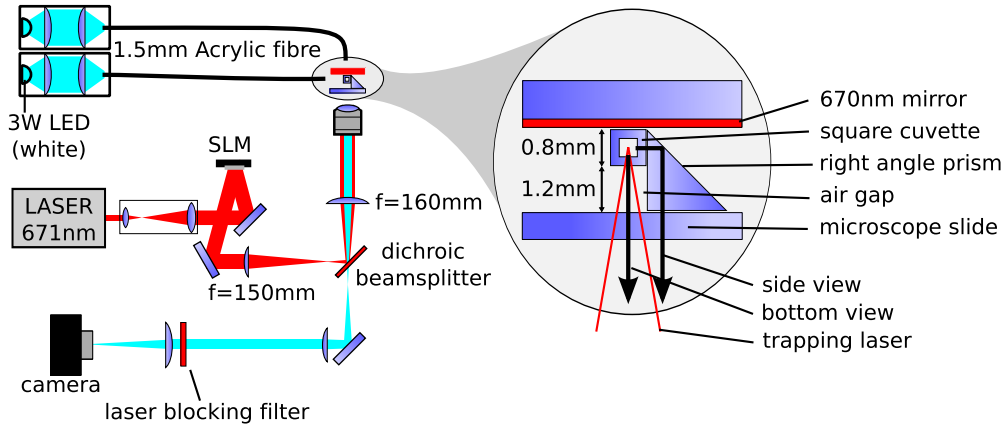


Figure 6.2: The sample cell and optical system used to implement closed loop control in the “macro-tweezers” geometry. Samples were held in a square cuvette, with a mirror immediately above it. A right-angle turning prism provided the side view, and an air gap was left directly underneath the sample such that the side view and bottom view would both focus on the centre of the cuvette when viewed through the same objective, from below.

A simple proportional controller is used to minimise the displacement of the bead from the setpoint [54, 139]. More precisely, the balance of power in the two beams $\beta = (P_{\uparrow} - P_{\downarrow})/P_{\text{total}} = a_z \Delta z$ where Δz is displacement, a_z is feedback gain and P_{\uparrow} , P_{\downarrow} are the powers in the two beams. However, as the force due to changing β is nearly independent of the particle’s position, the controller is effectively integrated by the bead on timescales smaller than the autocorrelation time, which is several seconds ($\dot{z}_{\text{bead}} \propto \beta$ and hence $z_{\text{bead}} \propto \int \beta dt$).

The control loop runs at 1 kHz, the speed of the camera. The SLM is updated each time it refreshes, which occurs at the maximum frame rate (203Hz). The system’s round trip latency is in the region of 10 ms, which means the servo loop becomes resonant at around 20 Hz. This is a significant limitation when working with small objects where there is significant Brownian motion above this frequency, which cannot be compensated for with servocontrol. However, the larger objects which can be trapped in counter-

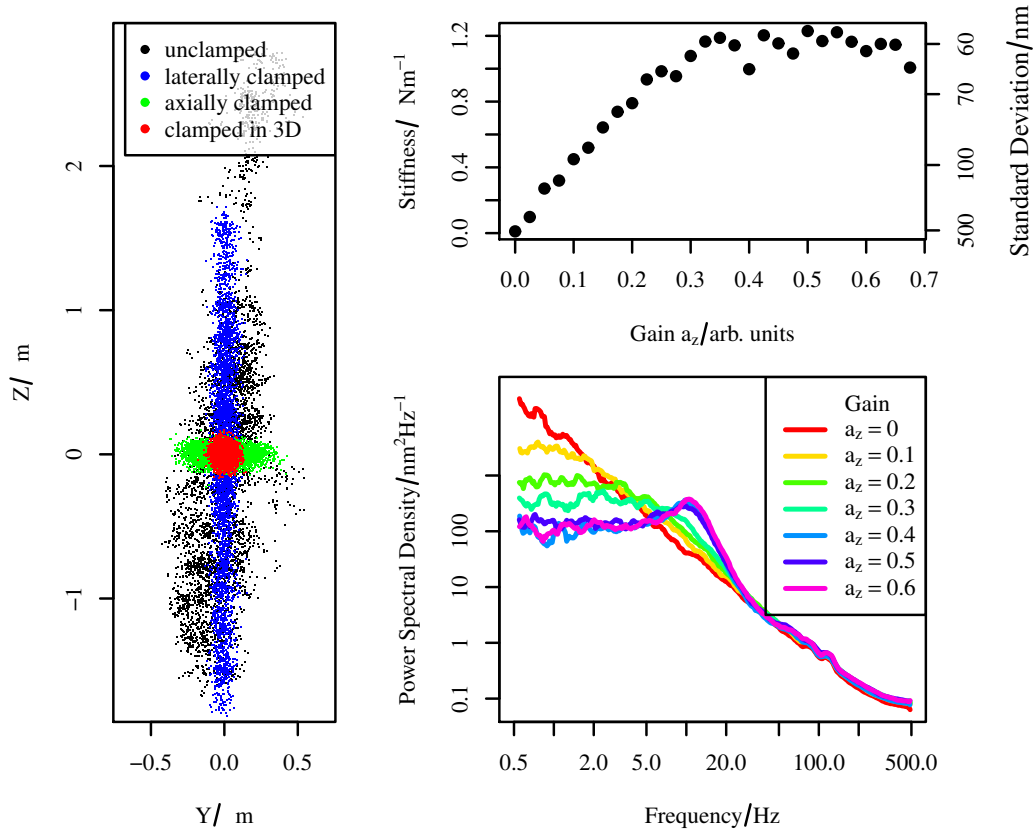


Figure 6.3: A scatterplot of the motion of a $10\ \mu\text{m}$ silica particle in the trap with and without feedback (100s of data at 1 kHz), along with power spectra of the particle's motion and corresponding stiffness values for different feedback gains a_z in the axial direction.

propagating traps are more strongly damped by the surrounding fluid, and consequently they exhibit less high-frequency motion. This means that a greater proportion of their Brownian motion can be cancelled out.

6.2 Results

Using the system described above, a $10\ \mu\text{m}$ silica sphere was held in a trap, and then servocontrol was activated laterally, axially, and in 3D. A scatterplot of the bead's motion in y and z is shown in Figure 6.3(a). Stiffness in x ,

y and z (as estimated using the equipartition formula, $\kappa_z = k_B T / \langle z^2 \rangle$) was increased from (0.14, 0.08, 0.004) μNm^{-1} to (1.9, 0.85, 1.3) μNm^{-1} . A stiffness of 1.5 μNm^{-1} was reached when the particle was clamped only in z . As the feedback gain is increased, the particle's position fluctuations decrease—the standard deviation of the position fluctuations in z was 1 μm in open-loop mode and 53 nm with feedback. Power spectra for axial motion are given in Figure 6.3 as a function of gain, along with a plot of effective stiffness against gain. The y axis is the long axis of the cuvette. The ends of the cuvette were connected to small plastic hoses to simplify the process of loading a sample. These hoses were clamped shut during measurements, but residual fluid flow made the y direction more susceptible to mechanical interference. This, combined with slight misalignments, may explain the lower stiffness in y .

Active feedback not only reduces position fluctuations, it also improves the speed and settling time when moving particles over longer distances. Figure 6.4 shows particle tracks for a 10 μm bead moved in a square wave pattern in the axial direction. In open-loop mode, the axial position of the two foci (separated by 20 μm , chosen to maximise axial stiffness) were shifted to move the trap centre to the position set-point. The axial stiffness is very low, so the relaxation time of the trap was much longer than the few seconds between flips. With closed-loop control, the bead quickly reached the set-point. The response time of the bead was limited by the maximum speed which could be reached by the particle, with all the power in one beam. This is why the response is predominantly linear rather than exponential. The amplitude of 20 μm was the maximum possible without the bead being lost from the trap in open-loop mode.

Holographic optical tweezers and camera-based position sensing make it simple to extend closed-loop control to multiple particles: Figure 6.5 shows three beads position-clamped in 3D. The stiffness of these traps was approximately $0.7 \pm 0.2 \mu\text{Nm}^{-1}$ in 3D. Weaker traps are to be expected relative to the single-trap case as the same laser power is divided between three traps.

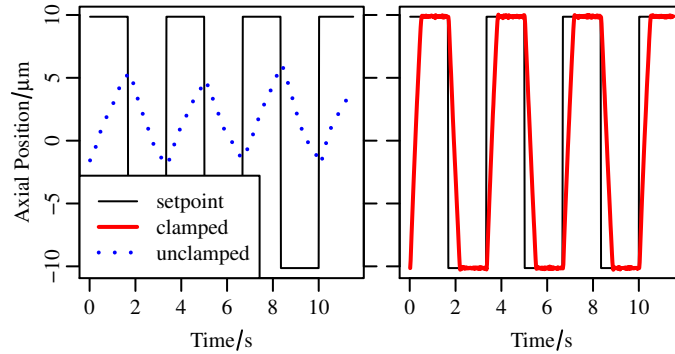


Figure 6.4: Response of a 10 μm bead to a square-wave control signal, with and without feedback. Video [online](#) [82] or on enclosed disc.

Provided the regions of interest corresponding to each trap were distinct (i.e. separation $\geq 20 \mu\text{m}$), crosstalk between traps was not observed.

6.3 Discussion

The use of closed loop control in a counterpropagating optical trap can significantly increase both the effective stiffness of the trap and the maximum axial force it can apply. The servocontrolled trap is stiff and stable when the two foci are close together, which maximises the available lateral force (in the open loop system one must compromise between axial stability when the foci are well separated and maximum lateral force when they are close together). This is important when manipulating particles over the comparatively large distances, and hence high speeds, accessible using a low-magnification objective. This implementation uses a high-speed camera [97] and a fast SLM with optimised hologram generation to increase the bandwidth of the system by an order of magnitude compared to previous work [81]. Its bandwidth is sufficient to increase the axial trap stiffness by a factor of 300, thereby suppressing a significant portion of the particle's position fluctuations due to Brownian motion. Also, the ability to axially reposition the foci increases the maximum force available to us compared to a fixed-focal-plane system

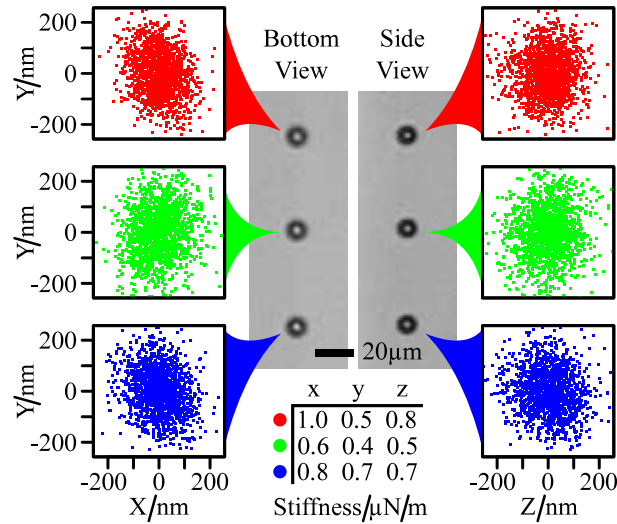


Figure 6.5: Three $10\ \mu\text{m}$ beads simultaneously clamped in 3D, with scatter-plots of their position. Stiffness values are shown below the image.

such as [76].

Having a side view allows very simple 3D tracking of particles for closed loop control, and is a useful addition to existing techniques. Digital holographic microscopy can track objects in 3D [100,126], but requires demanding image processing making it too slow for closed-loop control at present. It also requires coherent light and often a high-NA objective. Similarly, stereoscopic particle tracking [15,55,102,128] achieves high resolution only in conjunction with high-NA optics. Looking from the side has been implemented before using an additional objective [172], however the convenience of a modified sample cell [11] is a significant advantage.

Holographic dual-beam traps are a useful addition to our toolkit for micro-manipulation, as they extend the range of sizes and sample geometries that are compatible with optical manipulation. The ability to work with large objects without sacrificing accuracy in position allows the use of larger optically actuated tools [113,117], which could prove simpler to manufacture. Larger sample volumes also permit a wider range of specimens to be investigated, and allow larger areas to be probed without having to shift the microscope

stage. As objects are held between the foci rather than in a focus, the peak intensity experienced by the trapped object is much less. Dual beam traps are thus well suited to working with biological samples, and might prove useful in work with motile micro-organisms, which require high powers to trap effectively. Improving the axial confinement in such systems is important for them to be useful, and this has led to a combined acoustic and optical trapping system being developed [174]. The work in this chapter, however, provides a method which allows objects to be repositioned axially rather than simply confined to a plane, and requires no equipment over and above the SLM which is already in use.



Chapter 7

Interface technology

In the preceding chapters, I have documented many of the capabilities of holographic optical tweezers. The technique affords a great deal of flexibility in the way we interact with microscopic objects as it can deal with multiple points of contact, in arbitrary 3D configurations, with force measurement in real time. In a number of situations, the limiting step is not the experimental hardware but the software interface used to control it. More specifically, the primary way of interacting with optical traps is to use a mouse. A standard mouse, however, only gives 2D control of a single point and offers no sensation of force.

The interfaces described in this chapter addresses this limitation, by using a 3D force feedback joystick to restore the tactile feedback that is lost when operating via a computer. Many current consumer devices, such as the iPad, have a multi-touch interface that is a perfect match to the problem of controlling many particles at once. I have taken advantage of this rich in-

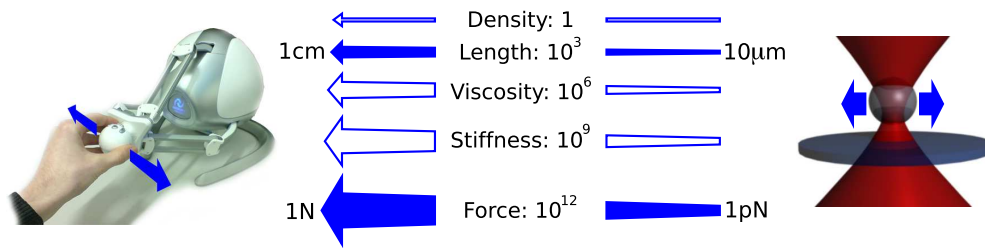


Figure 7.1: Scaling factors between the microworld and the macroworld (filled arrows), and the distortion of dynamic parameters which follows by dimensional analysis (hollow arrows).

terface technology to create an intuitive multi-touch control application for holographic optical tweezers, building upon previous work using a custom multi-touch table [175].

Increasing the degree of automation is another approach to realise the full potential of parallel optical manipulation. Machine vision systems are very effective at performing specific tasks, for example automated assembly of microfabricated components [168, 176, 177]. This makes good use of the capability to manipulate particles simultaneously (in their case using counterpropagating optical traps). However, human control greatly speeds up trying out new experiments and dealing with problems which the computer has not encountered before.

7.1 Force feedback remote handling

Everyday tasks are possible thanks to our ability to see and touch. Neither sense is sufficient on its own; touch supplies the fine force perception necessary for delicate operations, while vision gives the necessary overview of the task. Touch is also faster; we are able to resolve information at up to 1 kHz instead of 24 Hz for vision [178]. This is important for macroscopic tasks such as picking up a soft piece of fruit, and is equally relevant to tricky operations on the micron scale where we must be careful to exert just the right force. Force perception through the hand is much more intuitive than

an indicator on a screen, and this is particularly important when interacting with objects that cannot readily be seen in the microscope.

Most tweezers systems use a mouse or a standard joystick to control the optical trap. Although more complex methods of position control have been tried [175,179], force feedback has been relatively unexplored. Restoring the sense of touch when using macroscopic robotic manipulators, termed “force feedback remote handling”, has improved the operator’s dexterity in surgery and nuclear energy applications. It has also been explored for non-contact manipulation with magnetic levitation by Van West *et al.* [180]. Within optical tweezers, haptic interfaces have been shown to help guide the user in following a path [181] and avoiding collisions [182] by generating an artificial force field to help guide the operator. This “haptic assistance” was shown to assist the user in performing various tasks, though it does not allow the user to feel the forces actually experienced by the particle.

Forces measured using a quadrant photodiode have been relayed to the operator in optical tweezers by Arai *et al.* [183]. However, this system used a piezoelectric nanopositioning stage to move the sample relative to a static optical trap, meaning that the operator sees the background, rather than the particle, moving. As well as being confusing for the operator, this technique is very difficult to extend to multi-particle manipulation: indeed, the authors have since implemented a holographic system building on the work described in this chapter [184].

The technique of “force feedback remote handling” refers to the use of 2 robots, a “slave” and a “master”, in our case the optical tweezers and a 3 axis force feedback joystick (Novint Falcon) respectively. The information passed between these two systems needs to be transformed, as forces and displacements have very different magnitudes in everyday manipulation and in the microscope (Figure 7.1). The relationship between master and slave systems is known as the “coupling” (see Figure 7.2(a)). The work presented here uses constant scaling factors, but more sophisticated schemes have been tried to compensate for latencies or other quirks of the manipulation system

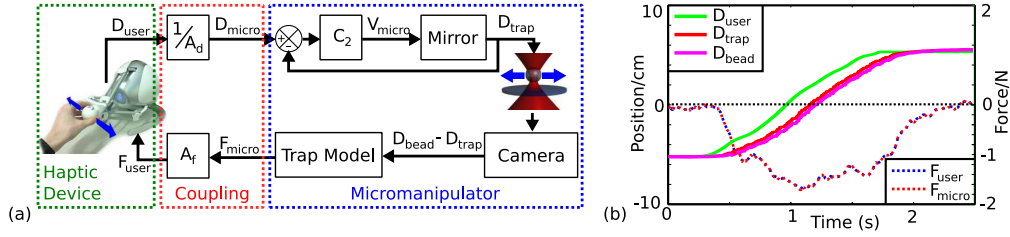


Figure 7.2: (a) Schematic of the control system for force feedback in optical tweezers. D_{user} and D_{micro} are respectively the displacement of the user's hand and the position set point of the laser. $D_{bead} - D_{trap}$ is the deviation of the bead from the trap centre and V_{micro} is the mirror speed command. F_{micro} and F_{user} are the estimated forces exerted on the object by the environment and the force feedback to the user. (b) Response of the system to a motion of the controller at a constant speed. The mirror lags behind the desired trajectory by 200ms, and for a $5 \mu\text{m}$ bead, the delay behind the trap is 50ms. The two force curves match exactly, showing good transparency in force. Microworld quantities have been scaled to macroworld units.

used [185]. In our case, force measurement in the optical tweezers system is used to create the sensation of touch on the joystick.

Microscopic dynamics are very different from conventional macroworld mechanics. On the metre scale, bulk forces like mass and inertia are the most important effects. On the micron scale, optical forces, viscosity, adhesion forces and Brownian motion are the predominant forces on trapped objects [5, 6]. The differences between the scaling factors (shown in Figure 7.1) for position and force cause distortion of the perception of the environment. For example, stiffness and viscosity are perceived as stronger than they are relative to displacements.

Because the dynamics of the two systems are different, there may be stability problems: deviations between the systems will increase instead of converging to zero, and the system will start to oscillate. This places limits on the scaling factors we can use to amplify forces and reduce displacements. As these scaling factors are necessarily large (to convert microns and pi-

coNewtons to centimetres and Newtons), the system is extremely sensitive to perturbations and delays, as discussed in more detail by Pacoret *et al.* [186]. This means that it is important to minimise latencies in the control loop, as well as measuring forces and moving the trap as quickly as possible. Energy introduced to the system by coupling two actuators with such high scaling factors must be dissipated for stable operation, and it is thus fortunate that most optical tweezers experiments are performed in liquid media. As viscous effects dominate inertial ones, the system is overdamped and viscous drag dissipates much of the unwanted motion.

7.1.1 Experimental configuration

In the optical tweezers, a camera tracks the position of the trapped object [68, 187]. Initially, a motorised mirror was used to steer a single trap in 2D, and a camera was located behind the trap steering mirror, such that the optical trap was always centred in the field of view. In later work using holographic tweezers, the position was measured using the stereoscopic system described in Chapter 2. This also afforded the user depth perception, by relaying the left and right images of the stereomicroscope to the operator's eyes with a stereo monitor (Zalman ZM-220W).

Forces measured on the trapped object were fed back as a force on the operators hand by the motorised axes of the haptic interface. The position of the joystick was scaled and used to control the position of the optical trap. The spherical handle of the Novint Falcon joystick used here is appropriate for working with microspheres, however other handles might be more appropriate for working with differently shaped objects. For example, a sharp-tipped probe might work well with a pen-shaped handle, which not only resembles the probe but also provides access to the orientational degrees of freedom of such a tool.

Figure Figure 7.3 shows a schematic representation of the experiment. Trapping is achieved using a CW Ti:sapphire laser system (M^2 , SolsTiS) which provides up to 1.3 W at 830 nm, as described in [188]. This is steered

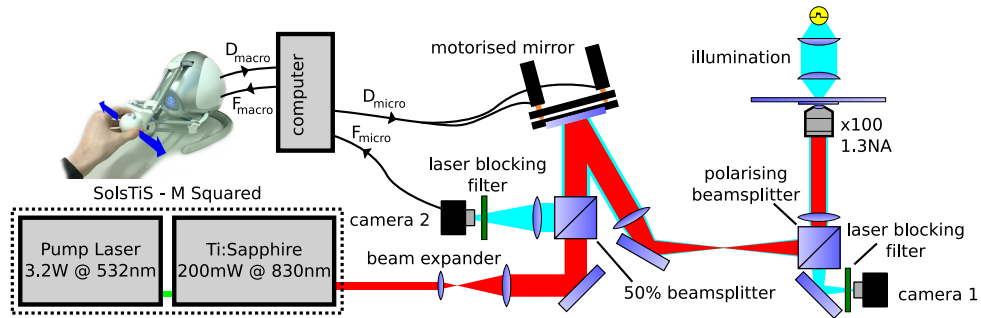


Figure 7.3: The laser beam is steered by a computer-controlled mirror, providing one trap with a power of approximately 30 mW. Camera 1 images a $60\ \mu\text{m}$ wide area of the sample, while camera 2 takes high-speed images centered on the optical trap for particle tracking and force measurement.

using a computer-controlled, micrometer driven mirror allowing us to position the trap anywhere within the field of view. The tweezers are based around an inverted microscope, where the same objective lens, 100x 1.3NA, (Zeiss, Plan-Neofluor) is used to both focus the trapping beam and to image the resulting motion of the particles.

Initially, two CMOS cameras were used to view the sample, with bright-field illumination. One was in the traditional location (immediately after the objective and tube lenses and therefore unaffected by the beam steering optics), and provides a wide field of view to see the experiment (Prosilica EC1280, camera 1). The other (Prosilica GC640M, camera 2) uses a reduced region of interest to take high speed images. The position of camera 2 behind the beam steering mirror (analogous to de-scanned detection in a confocal microscope) means that the trap will always be in the centre of the camera, and the workspace is limited only by the field of view of the microscope. Thus, by measuring the deviation of the particle position from the centre of the image, we can measure the force without knowing the position of the trap exactly. This makes the force measurement insensitive to position error and latency in the mirror control system. Positioning the camera behind the steering optics makes force measurement simpler and faster, and permits

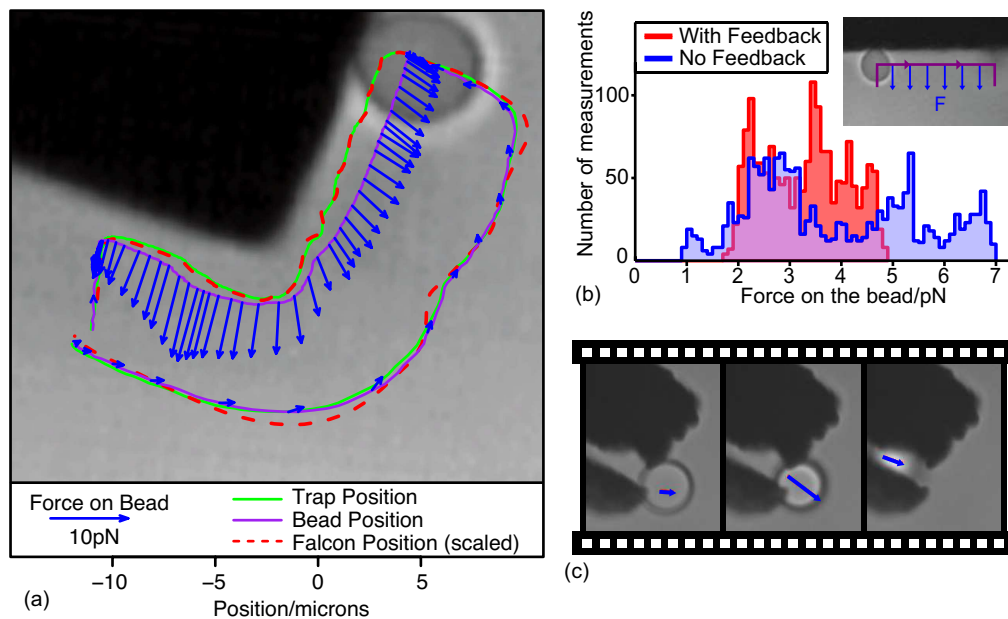


Figure 7.4: (a) A bead is pushed along the edge of a silicon cube, maintaining contact as it moves. The force acting on the bead is shown as arrows, at 130 ms intervals. (b) Histogram showing the force applied to a wall as the bead was moved along it, trying to maintain a constant force. The path followed (line) and force on the bead (arrows) are shown in the insert. (c) Frames from a video sequence showing a 5 μm silica bead being inserted into a crack in a piece of chrome. Video [online](#) [129] or on enclosed disc.

a larger workspace compared to a quadrant photodiode or a camera in the traditional position. A bandwidth of order 1 kHz is required for smooth perception of force, and this is reached by using a region of interest on the second camera 50 pixels across. The limiting factor in the responsiveness of this system is the steerable mirror. This approach was later improved by Pacoret *et al.* [186], by replacing the micrometer-actuated mirror with one mounted on a galvanometer, gaining orders of magnitude in the speed at which the beam could be steered.

7.1.2 Force feedback in 2D

Several tasks were performed using the mirror-based force-feedback system, using a $5\ \mu\text{m}$ bead trapped with a stiffness of about $1\ \mu\text{Nm}^{-1}$. The trap was calibrated using the equipartition method described in Section 1.4.3. First, we interacted with some silicon cubes, $100\ \mu\text{m}$ across. Figure 7.4(a) shows the path taken by the bead and the force acting on it as it was pushed around the corner of a cube. The system allowed intuitive perception of the reaction force when the bead was in contact with the cube, and of the viscous drag when it was moved through the water. Without feedback, this task is difficult: the bead often escapes from the trap or encounters adhesion on the corner. With force feedback, those problems are greatly reduced.

To demonstrate the improvement in dexterity due to haptic feedback, we used a simple task: the bead was moved into contact with a cube then pushed along the edge for $20\ \mu\text{m}$, attempting to maintain a constant force. This was performed ten times each with haptic feedback and with only visual feedback, and we recorded the force applied against the cube every 100 ms during the task. Haptic feedback resulted in the bead escaping from the trap less often; two attempts have been discarded due to failing the task with only visual feedback. The remaining eight trials resulted in a total of 1600 data points each, which are shown in Figure 7.4(b). Haptic feedback enabled better precision in maintaining a constant force during each repetition of the task.

As an example of micromanipulation, $5\ \mu\text{m}$ beads were used to explore the surfaces of pieces of chrome. Haptic feedback made it very clear when contact had been made with the surface, and enabled precise control of the force applied through the bead. One example was a chrome fragment with a crack into which a bead could be inserted, shown in Figure 7.4(c). Locating the entrance of the crack was made simpler by haptic feedback as the bead could be felt slotting into place. Haptic feedback also made it possible to apply just enough force to insert the bead, without applying any more than was necessary. This is especially relevant to micromanipulation to avoid ad-

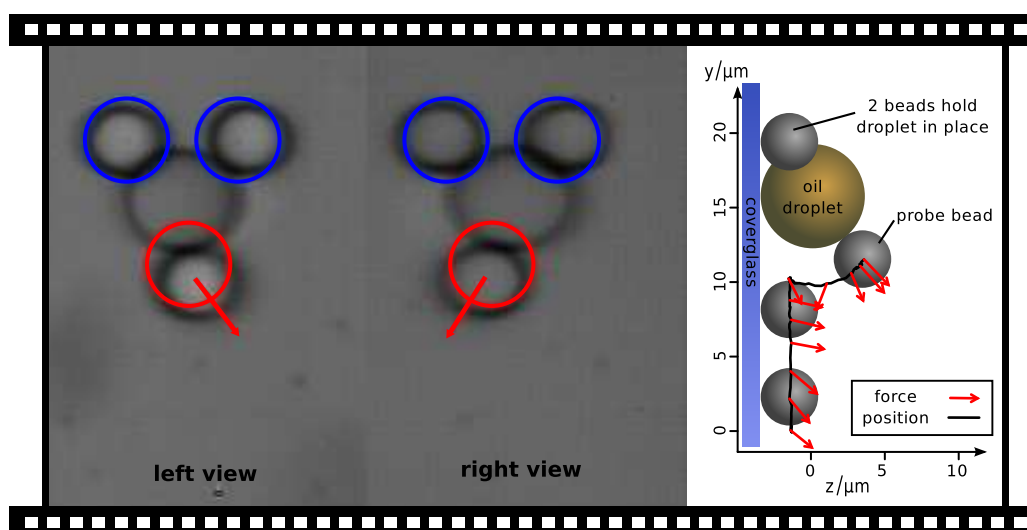


Figure 7.5: Left and right stereo images of a $5\ \mu\text{m}$ bead rolled up the surface of an oil droplet. (right) The path of the probe bead as it traces out the coverslip and oil droplet in the y - z plane. Video [online](#) [55] or on enclosed disc.

hesion, and to microassembly, where the forces involved are often important to position parts correctly.

7.1.3 Force feedback in 3D

By using the stereoscopic particle tracking described in Chapter 2 to measure the displacement of the trapped bead from the centre of the trap, it is possible to generate force data in real time. The CMOS camera was run at 400 frames per second, with a region of interest 659×220 pixels in size. This enabled particles to be tracked as they were moved around with HOT, and hence the 3D joystick could be used both to control the position of the particles in 3D and to relay the measured forces to the user at 400 Hz.

Brownian motion and drag forces could be perceived by the user in three dimensions, as well as contact forces from the microscope coverglass, inaccessible to the 2D system as the force is only in z . Most importantly, the system allowed perception of forces from objects “touched” with a trapped

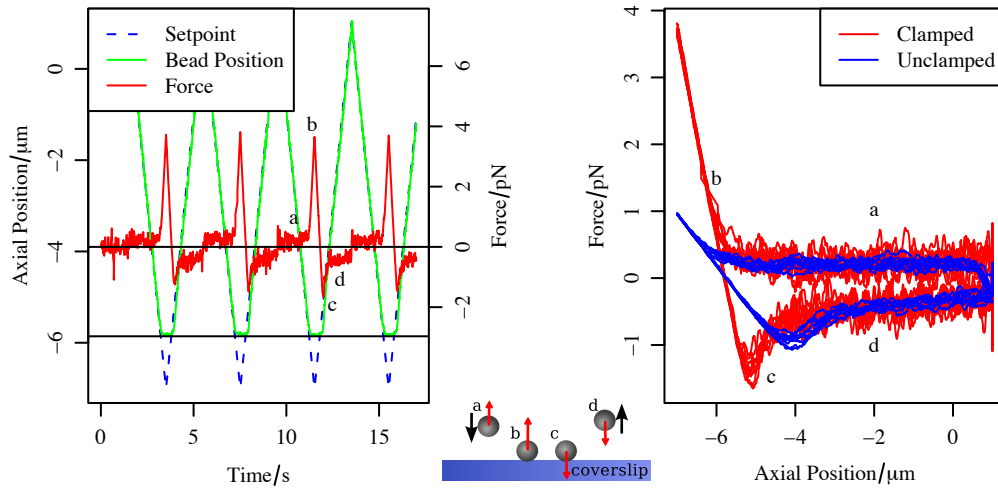


Figure 7.6: Measured force and position data as a $3\ \mu\text{m}$ silica bead was pressed against the coverslip. We see (a) viscous drag as the particle is moved down, (b) contact force as the bead is pushed against the coverslip, (c) a force in the other direction as the bead is removed, and (d) viscous drag as it is moved up.

bead, such as the oil droplet shown in Figure 7.5. The accompanying video demonstrates that we can generate quantitative force and position data at the same time as performing force-feedback micromanipulation in 3D. It opens the way to interactively scanning 3D scenes with a bead [85, 189] or even an optically trapped tool [114, 117].

Forces were measured using the camera and relayed to the joystick in a control loop running at 400 Hz, while the fast holographic control system of Chapter 3 updated the SLM at 203 Hz. The SLM had a response time of around 3 ms [54], making the system much more responsive than the previous, mirror-based haptic interface.

It was possible, using the high-speed SLM, to activate closed-loop position clamping (as described in Chapter 3) at the same time as interactively manipulating particles. Figure 7.6 shows a $3\ \mu\text{m}$ silica bead being pressed against the coverslip with and without position clamping. Initially, we see

the Stokes drag force as the bead is moved towards the coverslip (labelled ‘a’ in Figure 7.6). This force is the same whether or not position clamping is enabled, showing that the system estimates constant forces consistently. As the coverslip is rigid, we assume the bead does not move once it has made contact. The force-extension curve (labelled ‘b’) therefore represents the apparent stiffness of the trap, which is increased by active feedback. The enhanced drag force as the particle leaves the surface (‘c’) and as it makes contact (between ‘a’ and ‘b’) is due in part to hydrodynamic interaction with the coverslip [112, 190].

Shorter-range effects such as electrostatic potentials and structured water layers also affect the interaction between the bead and coverslip, for example preventing the bead sticking to the coverslip [191, 192]. These forces are also important in Figure 7.5, however as they are relatively short-range (a few nanometres) the surfaces of the droplet and the coverslip can reasonably be modelled as rigid and non-stick. Effects due to multiply-scattered light between the bead and coverslip [90] are not apparent here due to the lower trap stiffness used. All the forces in Figure 7.6 are calibrated by the equipartition method [90], and the graph is plotted from 20000 data points taken at 400 Hz.

At present, the force relayed to the user assumes an infinitely fast feedback system which results in exaggerated high-frequency forces, visible in Figure 7.6 as increased noise. Modelling the system should allow us to correct for this effect, which is important if we are to take force measurements in position-clamped mode [173].

7.2 Multi-touch micromanipulation

Apple’s multi-touch tablet computer has been the focus of much attention since it was launched in early 2010, and it has encouraged further development of the multi-touch interface technology used by the latest generation of smartphones. This includes the idea of multi-touch gestures where the user



Figure 7.7: The iTweezers interface as shown to the user. Video [online](#) [193] or on enclosed disc.

can, for example, zoom in on an image by moving two fingers further apart. The iPad provides a 10 inch colour screen with capacitive touch sensor, and it is capable of processing up to 11 simultaneous touches and relaying them to the active application. iTweezers, an application I have written for the iPad, uses this multi-touch technology to control multiple particles in 3D.

7.2.1 Implementation

Images are streamed from the microscope and displayed on the iPad, overlaid with markers representing optical traps as shown in Figure 7.7. Using the JPEG compression available in the National Instruments Vision library, we can stream up to 20 frames per second from the control PC to the iPad over a wireless network (limited by available CPU power on the iPad—an iPad 2 can reach 40 Hz). Up to 11 optical traps can be simultaneously dragged around, and they can be created and removed with a double-tap on the screen. Double-tapping with multiple fingers creates multiple optical traps simultaneously, which is very useful when trapping non-spherical objects [114]. The interface represents the axial position of optical traps by the size of the ring-shaped markers. This leads naturally to the use of “pinch” gestures, where stretching or squeezing a marker with two fingers moves the corresponding particle up or down. All these functions are demonstrated in the video (online).

The trap co-ordinates are synchronised over the wireless network with a

desktop computer, which controls the SLM using the same LabVIEW software used elsewhere in this thesis [153]. Trap positions can also be modified on the computer and changes sent to the iPad, which allows the interface to be switched on and off without losing the traps.

Translating the microscope stage from the iPad interface is achieved by tilting the device. The accelerometer data is relayed to the control PC, which then controls the stage (ASI MS-2000) via a serial link. Variable-speed control is possible, and a dead zone is defined when the iPad is nearly horizontal to avoid accidental drift of the stage.

To make it as responsive as possible, the interface runs as a native application on the iPad, which allows the use of Apple's gesture recognition toolkit. This toolkit simplifies the implementation of multi-finger gestures and ensures that particles are moved smoothly (fingers can be followed at up to 200 Hz), preserving continuity for each touch. Continuity and smoothness are important to avoid dropping particles, and processing touches on the device also frees up resources on the control PC. Markers representing optical traps are drawn on the iPad, so they follow the user's fingers closely even when the video image lags behind (by 200–500 ms). This keeps the system responsive, so latency in the video stream only shows up as particles lagging behind the trap markers as they are moved and does not cause particles to be lost from their traps. Video lag could be decreased (and frame rate increased) by using a more sophisticated video streaming codec and further optimising the network code, however there is relatively little to be gained from higher video frame rates and even sophisticated streaming protocols often involve significant latency.

7.2.2 Interactive hologram demo

When talking about holographic optical tweezers to non specialists, one of the most frequently asked questions is what the holograms look like. To help explain this, I have released an application which uses the iPad (or iPhone) GPU to render these holograms as the backdrop to the trap markers (see

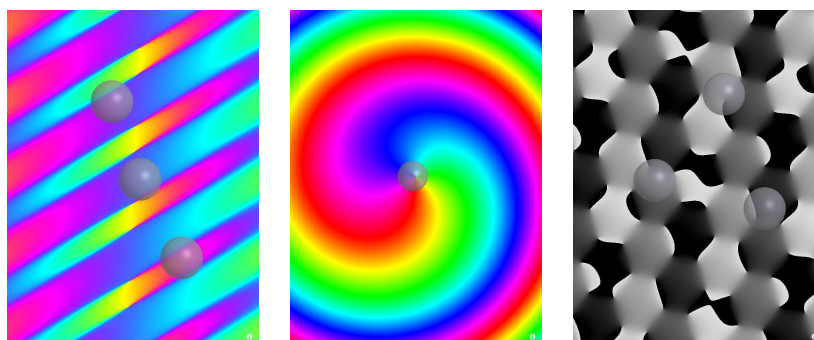


Figure 7.8: Screenshots of the interface being used to generate holograms on the iPad GPU, downloadable from the iTunes store as “iHologram”.

Figure 7.8) instead of the microscope image. This application is available free of charge from the iTunes store, and does not require a tweezers system to operate. Its main aim is to illustrate the key points of Fourier optics and diffraction as used in a tweezers system, in an accessible way. It also functions as a showcase for the multi-touch interface, and for the GPU technology which is used to generate holograms at high speed (Chapter 3).

7.2.3 Further interface improvements

Controlling the positions of optical traps is the core purpose of the optical tweezers interface, but not its only function. A number of instruments are often connected to the tweezers control program, such as the microscope stage, illumination, camera and laser controller. Replicating the controls in selected LabVIEW programs on the iPad makes it possible to control these items from the simple touch interface. I have implemented this function in a virtual drawer which slides in and out as required, and requires little or no modification to the program being controlled on the PC.

Another improvement to the interface is the integration of haptic feedback. While it is not possible to get the detailed 3D force information that can be relayed through the joystick used earlier in this chapter, it is possible to provide useful information to the operator via audio and vibrotactile



Figure 7.9: A task used to assess the effectiveness of vibrotactile feedback in iTweezers. Users were asked to collect beads and move them through a maze to the blue target area.

feedback. Lamont *et al.* [194] worked with me to extend iTweezers with a “tactor” attached to the back of the iPad. Dynamically synthesised sounds and vibrations give feedback proportional to the magnitude of the force acting on the beads. This interface also indicates the strength of the traps when the user starts to move them, and indicates when a particle has been lost from a trap. These simple audio and tactile cues can be interpreted more readily than the images on the iPad screen, especially as the trapped objects can easily be obscured by the operator’s fingers. An experiment where users were asked to perform tasks with and without feedback demonstrated that the extra feedback improved their performance. To ensure consistency, this experiment was performed using a simulation of the optical tweezers system, which I built in to the application. Realistic images are generated on the device, making the user experience very similar to that obtained using a real tweezers system.

7.3 Discussion

As optical tweezers are increasingly used by non-specialists, effective, intuitive interfaces become ever more important. Force feedback is a very powerful way of increasing the dexterity of someone using optical tweezers, restoring the tactile sensation that allows our hands to perform delicate operations in everyday life, such as picking up a soft fruit without crushing it. Awareness of the forces involved is also extremely useful when exploring surfaces with optically trapped probes, as maintaining contact with a surface without dropping the probe is a difficult problem. While computer control can implement constant-force scanning of objects, a human operator in the control loop has much more scope to adapt to the object being probed, perhaps modifying the motion of the probe based on the video image as well as the measured force. This avoids situations where an automated scan fails and must be restarted from scratch, as the operator is able to fix problems as they occur.

One of the limitations of the current system is the trade-off between field of view and speed. While the two-camera system overcomes this limitation for a single particle, the stereo tracking uses a single camera for both the view relayed to the user and the raw data for particle tracking. CMOS camera technology is constantly increasing in speed and so this limit on measurement bandwidth is being raised. However, a more elegant approach would be the use of smart camera technology to move particle tracking into the camera hardware [195, 196]. This means that image data need only be acquired at standard video rates, while high-speed particle position information can be obtained with low latency and minimal commitment of processing power from the control computer. Pacoret *et al.* took an alternative approach to more responsive manipulation—instead of replacing the mirror with an SLM, they used a galvanometer-driven mirror. This gave a very responsive actuator (galvanometers can respond faster than 1 kHz), and kept the fast second camera. However, this approach does not scale to multiple particles and consequently their research group is also active in the development of smart

cameras [196].

The force feedback interface, particularly when combined with the stereoscopic vision system described in Chapter 2, is excellent for tasks requiring the highest level of immersion in the experiment. However, often optical tweezers are used in conjunction with other technologies (microfluidics, for example), meaning that operation of a microscope or other equipment must occur simultaneously with operation of the tweezers system. In this case, it is imperative that the tweezers interface is extremely fast and simple to use, and iTweezers has risen to this challenge in a number of experiments. The iPad-based interface allows intuitive control of a holographic optical tweezers system using a dedicated application on the iPad and the LabVIEW application “Red Tweezers” running on a host PC. Multiple particles can be simultaneously manipulated in 3D, overcoming a long-standing limitation of mouse-based interfaces.

Wireless control means that the tweezers system can be operated from outside the lab. Remote control can be useful for laser safety or contamination control reasons. It also allows the interface to be repositioned within the lab, allowing real-time monitoring of the camera image as the laser is aligned or the illumination is adjusted, without moving the control PC inside the laser area. The interface is responsive and easy to use, so even inexperienced users can trap particles, move them around and translate the microscope stage. The iPad app is more effective than the mouse-based interface for these tasks, and has a much shallower learning curve [194]. It is my hope that, in the future, this interface technology will improve the usability and uptake of optical tweezers by non-specialists.

iTweezers is now available as a free download from the iTunes store (including the simulation for demo purposes), and has been used to control experiments in a number of other research groups. I have also adapted it for Kleindiek Nanotechnik GmbH to control their piezoelectric nanomanipulators, used in electron microscopy. As multitouch interfaces become more commonplace in consumer devices, applications like this have the potential

to make scientific instruments easier and more intuitive to operate. This realises the full potential of the instrumentation, and enables the scientists operating it to focus on scientific problems rather than the limitations of their equipment.

Acknowledgements

The initial work on 2D force feedback was carried out jointly with Cecile Pacoret, Ph.D candidate working on haptic interfaces for micromanipulation, from a robotics group at Institut des Systèmes Intelligents et Robotique (ISIR), Université Pierre et Marie Curie & CEA LIST, Laboratoire Interfaces Sensorielles, Paris, France. I would like to thank Prof. A. Walton from the School of Engineering and Electronics, Edinburgh University for fabricating silicon micro-cubes and COST for funding a short term scientific mission. I constructed the optical system and LabVIEW control software for the 2D force feedback system, and was entirely responsible for the 3D system. The inspiration for the iPad work came from the development of a multi-touch table by collaborators in the University of Bristol. The multi-touch interface presented in this chapter, however, is entirely my own work. Development of the vibrotactile interface was done by Stuart Lamont during a summer project jointly run with Prof. Rod Murray-Smith from the School of Computer Science at Glasgow University.



Chapter 8

Conclusions

As science asks ever more questions on tiny length scales and engineering is increasingly concerned with micro-structures, the need for robust, simple and precise micromanipulation is clear. The technologies described in this dissertation have been designed and implemented with robustness and simplicity, as well as functionality, in mind. One of the key advantages of cameras over interferometric tracking is their ease of use, which is a crucial factor in the uptake of a new technology by non-specialists. The convenience and versatility of cameras and spatial light modulators have led to an increasingly large community of users of holographic optical tweezers, despite the higher bandwidths available with acousto-optic deflectors and quadrant photodiodes.

8.1 Stereoscopic tracking

Reliable, linear tracking of objects over a three dimensional volume is a valuable tool for position and force measurement in optical tweezers. It also has wider applications, for example in particle imaging velocimetry or other microscopy techniques, where the ability to image and track in 3D can be used without combining it with optical tweezers. Within optical tweezers, it complements interferometric methods by providing a simple, easier to align system which is independent of the laser. This last point is important, as camera tracking measures the absolute position of objects in the sample cell, rather than their displacement from the laser focus. In many situations, for example when the laser is rapidly moved in closed loop control or when trapped objects are used to map out a surface, this is a significant advantage, though for static force measurements it can be useful to measure displacement directly rather than estimating and subtracting the position of the laser.

Independence from the laser also means that holographic optical tweezers, which create a complicated interference pattern in the back focal plane, can be combined with camera tracking to give manipulation and measurement of multiple particles. Quadrant photodiodes or position sensitive detectors looking at transmitted laser light still attain higher bandwidths, however camera-based tracking does perform fast enough to enable closed loop control. Camera technology is constantly improving; real time tracking at 10 kHz is possible using modern cameras [97] and this upper limit is constantly increasing. In this thesis, I have used stereoscopic particle tracking to demonstrate the first closed loop control of optically trapped objects in 3D, and it has also been used to effect the first servocontrol of optically actuated microtools [118].

Working with non-spherical objects (such as micro-tools or even cells) requires the relaxation of a number of assumptions, and implies that our system must be robust to imperfections such as misshapen trapping handles and non-orthogonal modes of motion. These problems create difficulties for holographic microscopy and back focal plane interferometry, but the simple,

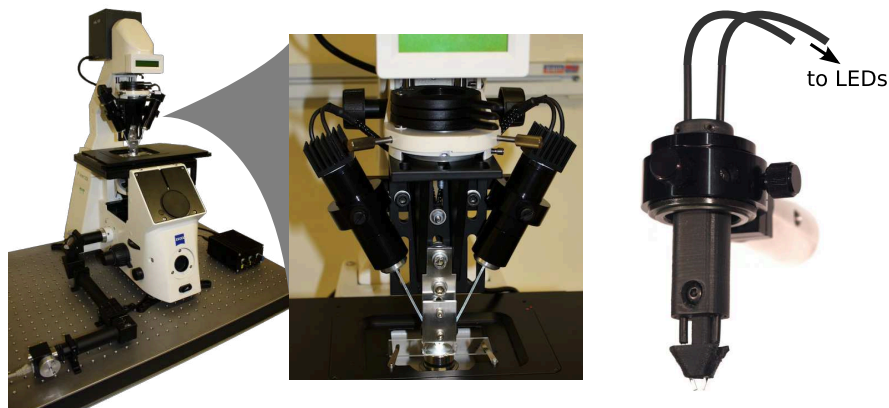


Figure 8.1: The stereoscopic imaging system, packaged to fit a Zeiss inverted microscope (left), along with an improved, 3D printed mount to fit the “Cube” tweezers system described later in this chapter (right).

robust tracking described in Chapter 2 maintains performance for imperfect objects, allowing me to work with non-spherical probes and paving the way for new probing and imaging techniques based around optically controlled tools.

This technology has developed from initial experiments to a mature system, transferred from my lab bench to collaborators’ laboratories in Bristol. Figure 8.1 shows the system built by Graham Gibson and I, packaged to fit a Zeiss inverted microscope using the standard add-on ports. I have continued to refine this system, most recently redesigning the fibre mount to take advantage of 3D printing technology, which enables me to precisely place the fibres at the correct angle. This eliminates the most difficult part of the alignment process and makes the stereo imaging system much more user-friendly, as well as ensuring the best performance is reached.

During my PhD I have also worked with Elliot Scientific (St. Albans, UK) to commercialise the 2D particle tracking software used in the Glasgow Optics group, an important step towards this technology gaining wider use. More generally, computer vision in microscopy has a great deal to offer the physical and life sciences. Applications include following the transport of

mitochondria through cells [197], monitoring cell signalling, and measuring the deformation of optically “stretched” cells [77]. These examples are but a few of those in the literature to date, and we have yet to realise the full potential of computer vision in microscopy.

New modes of microscopy have the potential to give new insights into physical, chemical and biological processes, and the use of Fourier filters in microscopes is a mainstay of many forms of optical microscopy. For example, dark-field, phase contrast and differential interference contrast (DIC) are all techniques which can be implemented with a simple Fourier filter. More general filters can be used to shape the point spread function of the microscope in many ways. In effect, the stereomicroscope in Chapter 2 produces an X shaped point spread function (in the x - z plane), but with a more complicated filter it would also be possible to produce other shapes. A phase-only filter implemented on an SLM in the same plane as the stereo filter has been used to create a double helix point spread function [62, 134], where the axial position of objects shows up as a rotation of the two spots relative to each other. Furhapter, Maurer and co-workers also used a spatial light modulator to implement various forms of microscopy (both conventional imaging modes and optimised ones with sophisticated filters) [61, 198]. Compared to these patterns, Fourier filtering with two wedge prisms and apertures is a simple technique, however this simplicity allows it to be robust and efficient. Avoiding diffractive optics in the imaging path also removes the problems of low diffraction efficiency and chromatic aberration, making it possible to image at high speed with white light.

8.2 Fast control

Historically, one of the biggest criticisms of SLM-based systems is the slow rate at which holograms can be updated. Recalculating the kinoform to move the beam has always been a computationally intensive task that has placed a limit of a few Hertz on the maximum refresh rate attainable with

holographic tweezers. Using graphics card technology takes advantage of the massively parallel processing unit already present in most computers, and has sped up by several orders of magnitude the rate at which we can generate holograms. In fact, with the OpenGL software written during my PhD, the limiting step is now the refresh rate of the DVI interface to the SLM. This is closely followed by the response time of the liquid crystal, which also limits the maximum speed attainable. However, driven at least in part by the demand for faster response times in commercial display devices, both the liquid crystals and their drive electronics are increasing in speed. The application of techniques used in consumer devices (for example “overdrive”, which actively adjusts the cell voltage to speed up its response) to SLMs will allow them to reach higher update rates. In turn, this will enable control of processes currently too fast to be accessible with holographic systems. Apart from better position clamping, faster holographic projection could be used to implement new scanning microscopy techniques or to probe cell signalling on a millisecond timescale [199].

There has been an increasing interest in recent years in the use of graphics processors for parallel processing. This technique, known as General Purpose Graphics Processing Unit (GPGPU) programming, has been enhanced by toolkits from GPU manufacturers, such as nVidia’s CUDA system, and OpenCL (by the Khronos group). Applied to problems as diverse as modelling fluid dynamics and analysing X-ray diffraction data, the availability of huge amounts of cheap computing power has allowed many experiments and simulations to be carried out which would previously have required access to large, specialised supercomputers. In optical manipulation, GPGPU processing not only enables more sophisticated hologram algorithms to be used but also allows more computationally intensive image analysis [101]. In the future, this could enable digital holographic microscopy to be performed in real time or permit many more objects to be simultaneously tracked than is currently possible.

A natural use of the ability to track objects and adjust the laser at high

speed is my work on closed loop control (Chapter 3), which enables better control of optically trapped objects. This is particularly noticeable when working with very large objects, either using the “macro-tweezers” system described in Chapter 6 or working with multi-handle objects in conventional single-beam traps [118]. Tailoring the trap’s characteristics to suit the experiment in hand can be accomplished with modified feedback algorithms [116]. This has particular promise for non-spherical tools, where one might, for example, want to constrain the position of one point on the tool (most usually the tip) as tightly as possible [118]. By generalising the feedback gain to couple different degrees of freedom (for example, reacting to a rotation of the object by translating the optical traps), we can affect the trapping dynamics of extended objects and exert better control over the motion of probe tips. This level of control is analogous to the various imaging modes present in atomic force microscopy, and is an important step towards realising scanning probe microscopy in optical tweezers.

8.3 Aberration correction

Adaptive optics uses reconfigurable optical elements to cancel out distortions in a light beam resulting from the optical system or an inhomogeneous sample. As SLMs can display an arbitrary phase pattern, it makes sense to use this ability to correct the system for aberrations. When using an SLM, the problem is not how to change the wavefront, it is simply one of determining the correct phase function to cancel out the aberrations.

A number of methods have been used to achieve this, from image analysis on higher-order beams [151] to interferometry that can recover a sharp spot even through very highly scattering media [73, 150]. This latter approach is able to recover very accurately the phase and amplitude of the wavefront distortion, at the cost of taking some time to acquire the necessary data. The Shack-Hartmann sensor described in Chapter 4 provides a much faster readout of the distortion, suitable for real time measurement. This means

that aberrations can be reduced by improving the alignment of the optics before using the SLM to correct the wavefront. While the SLM can correct for a great deal of aberration, it cannot restore beams which have been clipped due to misalignments in the system. It is also more efficient to correct relatively weak aberrations rather than trying to fix unnecessarily aberrated beams.

Facilitating quicker, better alignment of the optics in HOT is a significant benefit of the Shack-Hartmann sensor. Indeed, ensuring good alignment and compensating for misalignment is a very important part of making systems robust enough to be used outside of a specialist optics laboratory, by users whose primary concern is not the optical system but its application. Further automation of the correction process will ensure that holographic tweezers generate optimal traps every time, with alignment procedures that might be as simple as clicking a “calibrate” button.

Adaptive optics might also extend the scope of optical trapping to deeper, more biologically relevant samples. While most tweezers experiments pass the beam through nothing more than a few microns of distilled water, many biological applications demand trapping deeper into the sample, or trapping within a medium which is not optically homogeneous. Adaptive optics is capable of restoring imaging quality deep into samples that distort the beam [145, 148, 200], so there is no reason it should not be capable of enabling optical trapping experiments in challenging samples.

8.4 Trap shaping

As well as correcting for unwanted aberrations to restore a diffraction-limited focal spot, the SLM can be used to deliberately deform the laser focus, shaping the stiffness of the optical trap to suit particular tasks, as done in Chapter 5. This allows the optical trap to have a spring which is softened in one direction and stiffened in another, permitting, for example, tight constraint in lateral position while giving the probe freedom to move along the

measurement direction.

Optically adjusting the trap characteristics can be done simply, without monitoring the motion of the trapped object. However, more sophisticated optical control is possible when closed loop feedback is used to alter the trap properties. Rather than simply increasing the stiffness (which can be done more effectively by increasing the laser power), closed loop control allows the trap to dynamically respond to the trapped object's motion. Static trap shaping and active feedback have different advantages; the latter can effect virtual stiffnesses which are not possible in an open-loop system, while the former can be used to distribute the available laser power in the most efficient manner possible. They can also be used in combination, and key to both is the ability to reconfigure the traps' properties on-the-fly, thanks to the flexibility afforded by the SLM.

8.5 Counterpropagating traps

The addition of a mirror to the back of the sample cell allows low numerical aperture optics to project counterpropagating foci through a single objective lens. Using a spatial light modulator to do this means that the optical system is kept simple, and the 3D positions of upper and lower beams can be adjusted independently. While such systems typically do not attain the same optical stiffness as conventional high-NA optical traps, the addition of feedback control allows them to constrain objects to a similar volume (around 60 nm in each dimension). The larger available workspace allows objects tens to hundreds of microns in size to be manipulated, while the ability to tightly constrain objects makes the system suitable for force and position sensing. It might be easier to fabricate microscopic tools with handles tens of microns in size, and while these would not be useful in a conventional optical tweezer, the "macro-tweezers" geometry makes their use practicable.

8.6 Interface technology

If we are to create effective tools, we must find methods of controlling them which are robust, powerful and easy to use. The multi-touch interface described in Chapter 7 fulfils this brief for many qualitative experiments, providing intuitive control over multiple traps. It has since proved invaluable in the optical manipulation of self-assembling structures, where the operator must react to the growth of crystalline tubes in real time, often while adjusting other apparatus. The importance of effective interfaces is often overlooked in the design of scientific equipment, but in order to realise the full potential of a technology it is crucial that the operator has an effective way of controlling it. Furthermore, equipment which is intuitive to use allows scientists to spend less time learning to use equipment, and thus tackle more ambitious projects.

Force feedback interfaces are an interesting way of enhancing remote manipulation, and the force feedback system presented in Chapter 7 certainly restores a missing link by allowing the operator to feel the forces involved in micromanipulation. This sort of interface can enhance the dexterity of experienced users by giving them tactile information they can react to quickly, and it can shorten the learning curve for new users of the technology by making the strange dynamics of the micro-world quite literally more tangible. Adding vibrotactile feedback to iTweezers provides many of the benefits of force feedback, while preserving the advantages of the tablet interface such as portability, multi-particle control and the ability to use it at the same time as operating other equipment.

More generally, well-designed interfaces can enhance the use of new technologies enormously. My work on the tablet interface to holographic tweezers has been picked up by a number of other research groups and companies, and I have worked with Kleindiek Nanotechnik GmbH to bring multi-touch technology to their mechanical nanomanipulators. These use stick-slip piezoelectric motors to move nanometre sized tips inside electron microscopes, for nanofabrication or electrical measurement. Like iTweezers, the system



Figure 8.2: Piezoelectric nanomanipulators developed by Kelindiek Nanotechnology GmbH along with the tablet interface I developed, based on iTweezers. Video [online](#) (Glasgow University's iTunesU site) or on enclosed disc.

focuses on a microscope image (in this case an image from an electron microscope as shown in Figure 8.2), and the operator can manipulate the tips in 3D with gestures on the image. However, the nanomanipulators provide relative, rather than absolute, positioning and consequently the interface uses touch zones resembling trackballs, which can be continuously scrolled. Incorporating inertia (as is commonly done on modern touch-screen devices for displaying web pages) allows the tips to be moved quickly and smoothly, whilst retaining the ability to make small, controlled movements.

While each system has its own quirks and challenges, the ability of a rich, multi-touch interface to give the operator unfettered access to the available features is a common theme. To this end, I am involved in a project which aims to bring multi-touch control to LabVIEW, enabling engineers and scientists to trivially take advantage of touch interfaces to control their custom equipment, realising many of the goals of Chapter 7 with significantly less work required on the part of the developers of the apparatus to be controlled.

8.7 Commercialisation

The culmination of much of the work described in this thesis has been the construction of a portable optical tweezers instrument, shown in Figure 8.3. Removing the requirement for collaborative experiments to be performed in

the optics lab extends the scope of experiments which can be performed with researchers from other disciplines, and freeing the instrument from the constraints of a large optical bench opens up a number of possibilities for new experiments. The potential of holographic optical micromanipulation is huge, and taking it out of physics labs should help us find new experiments only possible in conjunction with scientists from other disciplines, including cell biology and chemistry amongst many others.

Miniaturising the optical system to fit underneath a motorised microscope stage (the optical unit measures approximately one cubic foot) not only enables portability, but actually improves performance; its small size reduces the influence of thermal drift and mechanical interference. The “Cube” is now commercially available from Boulder Nonlinear Systems (Boulder, CO), incorporating many of the technologies described in this thesis. In particular, it uses the fast SLM control technology of Chapter 3, a re-imaging arm that enables different imaging modes as used in Chapter 2, and aberrations arising from the necessarily shorter focal length lenses are corrected using the method described in Chapter 4. The system is controlled using “Red Tweezers”, the LabVIEW program developed throughout my PhD, and also features the touch-screen interface “iTweezers” outlined in Chapter 7. As well as the developments outlined in this thesis, the Cube owes much to the experience of Dr. Graham Gibson, with whom I jointly designed and built it.

The Cube was designed with non-specialist users in mind, and as such requires relatively little set-up or alignment. The alignment that is required is simplified by the placement of mirrors as close as possible to conjugate planes in the system, in an effort to minimise cross-talk between the adjusters. Enclosing the laser beam in an interlocked housing is an important safety feature which allows the system to be used outside a laser lab (and, indeed, at trade shows and public science demonstrations). All the alignment controls are accessible with the laser guards in place, which eliminates the need for laser safety eyewear during normal use. As well as making an optical set-up which

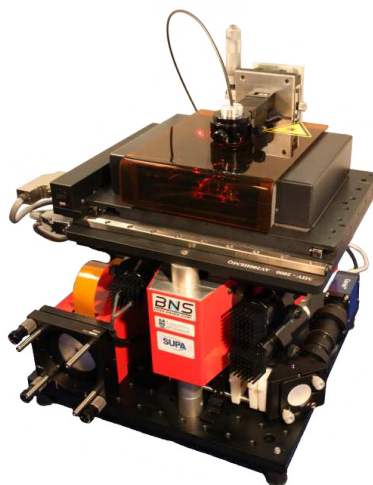


Figure 8.3: The “Cube”, a portable optical tweezers instrument which incorporates many of the techniques described in this thesis. It is now commercially available from Boulder Nonlinear Systems. Photograph by G. Gibson.

is easier to use, building the portable tweezers provided the opportunity to optimise the optomechanics. The most critical part of any microscope is the mounting of the sample and objective relative to each other. In the Cube, this is done using a custom aluminium tripod and a motorised microscope stage (ASI MS-2000), which allows the system to function effectively even when not placed on a mechanically isolated optical table. Miniaturising the optics also prompted the use of a 1070 nm fibre laser (IPG Photonics), which helps mechanical stability as well as removing a major heat source from the optical assembly. As the illumination is also delivered by fibre (using white LEDs as in Chapter 2 for either stereo or standard bright-field illumination) the only remaining heat source on the Cube is the camera. Combined with the fact that all the optics are enclosed, this is what makes the Cube more stable than the best system previously built in our lab [68].

Having now built and characterised the Cube, it is destined to be used for a number of experiments that would have been difficult or impossible to do with previous tweezers systems. Using the counterpropagating traps

described in Chapter 6, I will set up optical trapping inside an anvil cell, enabling us to work in an environment compressed to as much as 50 GPa. Collaboration with experts in high-pressure phenomena will then be made possible by the Cube's portability. Another possibility opened up by the size of the system is investigating the weight of particles. By tipping the Cube on its side, we change the direction of gravitational forces relative to the optics. This should enable the measurement of weight (or buoyancy) forces on a picogram scale. In addition to its uses in our lab, the availability of the portable tweezers as a commercial product will give access to scientists from many more diverse backgrounds and, I hope, promote the use of optical tweezers in applications far beyond the scope of this thesis.

In addition to the Cube tweezers system, I have been involved in two other transfers of technology. Elliot Scientific (St. Albans, UK) now sell a Camera Particle Tracking add-on to their optical tweezers system, which was also developed and transferred by myself and Graham Gibson. This complements their acousto-optic deflector based tweezers system, and their quadrant photodiode force measurement system. In fact, one major advantage of the camera system is that it can allow the QPD to be calibrated without the need for an expensive closed-loop piezo stage to generate known displacements. I have also produced a modified version of the iTweezers application described in Chapter 7 which will soon be marketed by Kleindiek Nanotechnik GmbH (Tübingen, Germany) as a more intuitive way of controlling their nanomanipulators. All three of the technology transfers described in this section took place under the "Easy Access IP" scheme (indeed, the Elliot Scientific deal was the first under the scheme), which facilitates very simple transfer of technology to industry [201]. By dramatically reducing the amount of work and investment required (relative to a conventional scheme where patents are applied for and then licensed to the company), the Easy Access IP scheme made it possible to bring these technologies to a much wider audience. This model for technology transfer enables engagement between academia and industry which would otherwise not be financially viable

for the university or the company, and has meant that I was able to work with a number of companies without taking large amounts of time out of research.

8.8 Optically actuated tools

Optically controlled probes and tools have been the motivation for many of the technologies explored during my PhD. Now that 3D trapping and tracking are working reliably, the next step is to realise scanning probe imaging with optically trapped probes. Ultimately, this should become a complementary technique to atomic force microscopy, with several orders of magnitude better force sensitivity, though consequently lower position resolution. There are many challenges to overcome, such as the fabrication of sharp, functionalised probe tips and the tendency of micro-objects to stick together with forces higher than those available using optical tweezers. However, optically controlled tools and probes are promising candidates for working with micro- and nano-objects, and should complement work on optically actuated micro-machines from the MEMS community [135, 165, 202].

During the work detailed in this thesis I have worked closely with Prof. Mervyn Miles's Nanoscience group at the University of Bristol, particularly with David Phillips, James Grieve, Stephen Simpson and David Carberry. Their work on the design and fabrication of optically actuated microtools is the counterpart to my work on multi-point positioning and measurement. Together, we are working towards the use of optically controlled probes which are able to map out nano structures and measure femtoNewton forces, without exposing the sample to the intense laser trapping light as happens in photonic force microscopy. Imaging was demonstrated using a naturally occurring structure [117], and work is ongoing with synthetic probes that have sharper tips. These probes will be tracked using the microscope described in Chapter 2 and controlled as in Chapter 3. Figure 8.4 shows some of our first probes made using two-photon polymerisation, imaged on the Cube tweezer-

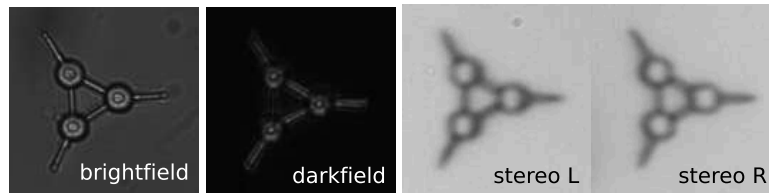


Figure 8.4: A microscopic tool, fabricated using two-photon polymerisation, imaged on the Cube tweezers system.

ers system in a variety of imaging modes. From the stereoscopic image, it is possible to recover precise force, position and orientation data in three dimensions [203].

Many of the applications of microscopic tools are in biology, where it is particularly important to isolate the specimen from the intense light of the trapping laser. Working with biological samples also requires the system to be robust to detritus in the trapping medium, which is a particular challenge for systems using coherent light such as digital holographic microscopy. The stereoscopic particle tracking I have described is relatively simple, and this simplicity brings with it an inherent robustness which is a great advantage when working with imperfect samples.

8.9 Conclusion

Holographic optical tweezers have developed from the first few experiments with home-made SLMs to powerful tools, built around cutting-edge imaging and beam shaping technology. They can measure some of the smallest forces in nature, and manipulate microscopic objects more delicately than any other technology in widespread use. The work presented in this dissertation develops this technology to provide better control and measurement of optically manipulated objects in 3D, particularly non-spherical objects such as tools. By using fast cameras rather than back focal plane interferometry, I have ensured that the technology is simple to use, align and calibrate, and is as reliable as the microscope it is built around. As we progress towards

the use of optically controlled tools and micro-machines, I look forward to seeing (and touching) the microscopic world with new eyes.



Bibliography

- [1] A. Ashkin, “Acceleration and trapping of particles by radiation pressure,” *Phys. Rev. Lett.*, **24**, 4, 156–159, 1970.
- [2] K. Svoboda, C. Schmidt, B. Schnapp, and S. M. Block, “Direct observation of kinesin stepping by optical trapping interferometry,” *Nature*, **365**, 6448, 721–727, 1993.
- [3] J. E. Molloy, J. E. Burns, J. Kendrick-Jones, R. T. Tregear, and D. C. S. White, “Movement and force produced by a single myosin head,” *Nature*, **378**, 6553, 209–212, 1995.
- [4] R. Brown, *The miscellaneous botanical works of Robert Brown*, J. J. Bennett, Ed. R. Hardwicke, London, 1866, **1**.
- [5] E. Purcell, “Life at low Reynolds-number,” *Am. J. Phys.*, **45**, 1, 3–11, 1977.
- [6] J. B. S. Haldane, “On being the right size,” *Harper’s Magazine*, March, 1926.
- [7] M. Wang, H. Yin, R. Landick, J. Gelles, and S. Block, “Stretching DNA with optical tweezers,” *Biophys. J.*, **72**, 3, 1335–1346, 1997.
- [8] A. Ashkin, J. M. Dziedzic, J. E. Bjorkholm, and S. Chu, “Observation of a single-beam gradient force optical trap for dielectric particles,” *Opt. Lett.*, **11**, 5, 288–290, 1986.

- [9] L. Bosanac, T. Aabo, P. M. Bendix, and L. B. Oddershede, “Efficient optical trapping and visualization of silver nanoparticles,” *Nano Letters*, **8**, 5, 1486–1491, 2008.
- [10] S. N. S. Reihani and L. B. Oddershede, “Optimizing immersion media refractive index improves optical trapping by compensating spherical aberrations,” *Opt. Lett.*, **32**, 14, 1998–2000, 2007.
- [11] S. B. G. Thalhammer, R. Steiger and M. Ritsch-Marte, “Optical macro-tweezers: trapping of highly motile micro-organisms,” *J. Optics*, **13**, 4, 044024, 2011.
- [12] A. Ashkin, “Forces of a single-beam gradient laser trap on a dielectric sphere in the ray optics regime,” *Biophys. J.*, **61**, 2, 569–582, 1992.
- [13] A. B. Stilgoe, T. A. Nieminen, G. Knoener, N. R. Heckenberg, and H. Rubinsztein-Dunlop, “The effect of Mie resonances on trapping in optical tweezers,” *Opt. Express*, **16**, 19, 15 039–15 051, 2008.
- [14] A. T. O’Neil and M. J. Padgett, “Axial and lateral trapping efficiency of Laguerre-Gaussian modes in inverted optical tweezers,” *Opt. Commun.*, **193**, 1-6, 45–50, 2001.
- [15] R. W. Bowman, G. Gibson, and M. Padgett, “Particle tracking stereomicroscopy in optical tweezers: Control of trap shape,” *Opt. Express*, **18**, 11, 11 785–11 790, 2010.
- [16] P. Wu, R. Huang, C. Tischer, A. Jonas, and E.-L. Florin, “Direct measurement of the nonconservative force field generated by optical tweezers,” *Phys. Rev. Lett.*, **103**, 10, 108101, 2009.
- [17] Y. Roichman, B. Sun, A. Stolarski, and D. G. Grier, “Influence of nonconservative optical forces on the dynamics of optically trapped colloidal spheres: The fountain of probability,” *Phys. Rev. Lett.*, **101**, 12, 128301, 2008.

- [18] G. Pesce, G. Volpe, A. Chiara De Luca, G. Rusciano, and G. Volpe, “Quantitative assessment of non-conservative radiation forces in an optical trap,” *Europhys. Lett.*, **86**, 3, 38002, 2009.
- [19] J. Arlt, V. Garces-Chavez, W. Sibbett, and K. Dholakia, “Optical micromanipulation using a Bessel light beam,” *Opt. Commun.*, **197**, 4-6, 239–245, 2001.
- [20] V. G. Shvedov, A. V. Rode, Y. V. Izdebskaya, A. S. Desyatnikov, W. Krolikowski, and Y. S. Kivshar, “Giant optical manipulation,” *Phys. Rev. Lett.*, **105**, 11, 118103, 2010.
- [21] A. O’Neil, I. MacVicar, L. Allen, and M. J. Padgett, “Intrinsic and extrinsic nature of the orbital angular momentum of a light beam,” *Phys. Rev. Lett.*, **88**, 5, 053601, 2002.
- [22] Y. Roichman, D. G. Grier, and G. Zaslavsky, “Anomalous collective dynamics in optically driven colloidal rings,” *Phys. Rev. E*, **75**, 2, 020401, 2007.
- [23] D. Carberry, J. Reid, G. Wang, E. Sevick, D. Searles, and D. Evans, “Fluctuations and irreversibility: An experimental demonstration of a second-law-like theorem using a colloidal particle held in an optical trap,” *Phys. Rev. Lett.*, **92**, 14, 140601, 2004.
- [24] D. Carberry, S. Williams, G. Wang, E. Sevick, and D. Evans, “The Kawasaki identity and the fluctuation theorem,” *J. Chem. Phys.*, **121**, 17, 8179–8182, 2004.
- [25] M. Dienerowitz, M. Mazilu, and K. Dholakia, “Optical manipulation of nanoparticles: a review,” *J. Nanophoton.*, **2**, 021875, 2008.
- [26] P. Neto and H. Nussenzveig, “Theory of optical tweezers,” *Europhys. Lett.*, **50**, 5, 702–708, 2000.

- [27] A. Mazolli, P. Neto, and H. Nussenzveig, “Theory of trapping forces in optical tweezers,” *P. R. Soc. Lond. A*, **459**, 2040, 3021–3041, 2003.
- [28] T. A. Nieminen, G. Knoner, N. R. Heckenberg, and H. Rubinsztein-Dunlop, “Physics of optical tweezers,” *Laser Manipulation of Cells and Tissues*, **82**, 207–236, 2007.
- [29] A. Rohrbach and E. Stelzer, “Optical trapping of dielectric particles in arbitrary fields,” *J. Opt. Soc. Am. A*, **18**, 4, 839–853, 2001.
- [30] T. A. Nieminen, V. L. Y. Loke, A. B. Stilgoe, G. Knoener, A. M. Branczyk, N. R. Heckenberg, and H. Rubinsztein-Dunlop, “Optical tweezers computational toolbox,” *J. Opt. A*, **9**, 8, S196–S203, 2007.
- [31] S. Simpson and S. Hanna, “Numerical calculation of interparticle forces arising in association with holographic assembly,” *J. Opt. Soc. Am. A*, **23**, 6, 1419–1431, 2006.
- [32] T. Nieminen, H. Rubinsztein-Dunlop, and N. Heckenberg, “Calculation and optical measurement of laser trapping forces on non-spherical particles,” *Journal of Quantitative Spectroscopy & Radiative Transfer*, **70**, 4-6, 627–637, 2001.
- [33] M. Reicherter, T. Haist, E. Wagemann, and H. Tiziani, “Optical particle trapping with computer-generated holograms written on a liquid-crystal display,” *Opt. Lett.*, **24**, 9, 608–610, 1999.
- [34] J. Moffitt, Y. Chemla, D. Izhaky, and C. Bustamante, “Differential detection of dual traps improves the spatial resolution of optical tweezers,” *Proc. Natl. Acad. Sci. U. S. A.*, **103**, 24, 9006–9011, 2006.
- [35] M. Klein, M. Andersson, O. Axner, and E. Fallman, “Dual-trap technique for reduction of low-frequency noise in force measuring optical tweezers,” *Appl. Opt.*, **46**, 3, 405–412, 2007.

- [36] L. McCann, M. Dykman, and B. Golding, “Thermally activated transitions in a bistable three-dimensional optical trap,” *Nature*, **402**, 6763, 785–787, 1999.
- [37] G. Brouhard, H. Schek, and A. Hunt, “Advanced optical tweezers for the study of cellular and molecular biomechanics,” *IEEE Trans. Biomed. Eng.*, **50**, 1, 121–125, 2003.
- [38] P. A. Kirkby, K. M. N. S. Nadella, and R. A. Silver, “A compact acousto-optic lens for 2D and 3D femtosecond based 2-photon microscopy,” *Opt. Express*, **18**, 13, 13 720–13 744, 2010.
- [39] Y. Hayasaki, M. Itoh, T. Yatagai, and N. Nishida, “Nonmechanical optical manipulation of microparticle using spatial light modulator,” *Opt. Rev.*, **6**, 1, 24–27, 1999.
- [40] D. G. Grier, “A revolution in optical manipulation,” *Nature*, **424**, 6950, 810–816, 2003.
- [41] D. A. Gregory, J. C. Kirsch, and E. C. Tam, “Full complex modulation using liquid-crystal televisions,” *Appl. Opt.*, **31**, 2, 163–165, 1992.
- [42] J. Liesener, M. Reicherter, T. Haist, and H. J. Tiziani, “Multi-functional optical tweezers using computer-generated holograms,” *Opt. Commun.*, **185**, 77–82, 2000.
- [43] J. Leach, K. Wulff, G. Sinclair, P. Jordan, J. Courtial, L. Thomson, G. Gibson, K. Karunwi, J. Cooper, Z. J. Laczik, and M. Padgett, “Interactive approach to optical tweezers control,” *Appl. Opt.*, **45**, 5, 897–903, 2006.
- [44] E. Dufresne, G. Spalding, M. Dearing, S. Sheets, and D. G. Grier, “Computer-generated holographic optical tweezers arrays,” *Rev. Sci. Instrum.*, **72**, 1810–1816, 2001.

- [45] R. D. Leonardo, F. Ianni, and G. Ruocco, “Computer generation of optimal holograms for optical trap arrays,” *Opt. Express*, **15**, 4, 1913–1922, 2007.
- [46] R. W. Gerchberg and W. O. Saxton, “Practical algorithm for determination of phase from image and diffraction plane pictures.” *Optik*, **35**, 2, 237, 1972.
- [47] J. R. Fienup, “Phase retrieval algorithms: a comparison,” *Appl. Opt.*, **21**, 15, 2758–2769, 1982.
- [48] V. Elser, I. Rankenburg, and P. Thibault, “Searching with iterated maps,” *Proc. Natl. Acad. Sci. U. S. A.*, **104**, 2, 418–423, 2007.
- [49] J. Curtis, C. Schmitz, and J. Spatz, “Symmetry dependence of holograms for optical trapping,” *Opt. Lett.*, **30**, 16, 2086–2088, 2005.
- [50] C. Hesselting, M. Woerdemann, A. Hermerschmidt, and C. Denz, “Controlling ghost traps in holographic optical tweezers,” *Opt. Lett.*, **36**, 18, 3657–3659, 2011.
- [51] R. W. Bowman, V. D’Ambrosio, E. Rubino, O. Jedrkiewicz, P. Di Trapani, and M. J. Padgett, “Optimisation of a low cost SLM for diffraction efficiency and ghost order suppression,” *Eur. Phys. J.—Special Topics*, **199**, 1, 149–158, 2011.
- [52] M. Persson, D. Engström, A. Frank, J. Backsten, J. Bengtsson, and M. Goksör, “Minimizing intensity fluctuations in dynamic holographic optical tweezers by restricted phase change,” *Opt. Express*, **18**, 11, 11 250–11 263, 2010.
- [53] M. Persson, D. Engström, J. Bengtsson, and M. Goksör, “Improving spot uniformity in holographic optical tweezers,” in *Optical Trapping Applications*, OTTuA2, 2011.

- [54] D. Preece, R. W. Bowman, A. Linnenberger, G. Gibson, S. Serati, and M. Padgett, “Increasing trap stiffness with position clamping in holographic optical tweezers,” *Opt. Express*, **17**, 25, 22718–22725, 2009.
- [55] R. W. Bowman, D. Preece, G. Gibson, and M. J. Padgett, “Stereoscopic particle tracking for 3D touch, vision and closed-loop control in optical tweezers.” *J. Opt. A*, **13**, 4, 044003, 2011.
- [56] S. Bianchi and R. Di Leonardo, “Real-time optical micro-manipulation using optimized holograms generated on the GPU,” *Comp. Phys. Commun.*, **181**, 8, 1442–1446, 2010.
- [57] H. He, M. E. J. Friese, N. R. Heckenberg, and H. Rubinsztein-Dunlop, “Direct observation of transfer of angular momentum to absorptive particles from a laser beam with a phase singularity,” *Phys. Rev. Lett.*, **75**, 5, 826–829, 1995.
- [58] N. Simpson, K. Dholakia, L. Allen, and M. J. Padgett, “Mechanical equivalence of spin and orbital angular momentum of light: An optical spanner,” *Opt. Lett.*, **22**, 1, 52–54, 1997.
- [59] Y. Roichman and D. G. Grier, “Projecting extended optical traps with shape-phase holography,” *Opt. Lett.*, **31**, 11, 1675–1677, 2006.
- [60] Y. Roichman, B. Sun, Y. Roichman, J. Amato-Grill, and D. G. Grier, “Optical forces arising from phase gradients,” *Phys. Rev. Lett.*, **100**, 1, 013602, 2008.
- [61] S. Furhapter, A. Jesacher, S. Bernet, and M. Ritsch-Marte, “Spiral phase contrast imaging in microscopy,” *Opt. Express*, **13**, 3, 689–694, 2005.
- [62] S. R. P. Pavani, A. Greengard, and R. Piestun, “Three-dimensional localization with nanometer accuracy using a detector-limited double-

- helix point spread function system,” *Appl. Phys. Lett.*, **95**, 2, 021103, 2009.
- [63] A. Ashkin, J. M. Dziedzic, and T. Yamane, “Optical trapping and manipulation of single cells using infrared laser beams,” *Nature*, **330**, 6150, 769–771, 1987.
- [64] H. Liang, K. Vu, P. Krishnan, T. Trang, D. Shin, S. Kimel, and M. Berns, “Wavelength dependence of cell cloning efficiency after optical trapping,” *Biophys. J.*, **70**, 3, 1529–1533, 1996.
- [65] M. Ericsson, D. Hanstorp, P. Hagberg, J. Enger, and T. Nystrom, “Sorting out bacterial viability with optical tweezers,” *J. Bacteriol.*, **182**, 19, 5551–5555, 2000.
- [66] G. M. Hale and M. R. Querry, “Optical-constants of water in 200nm to 200 μ m wavelength region,” *Appl. Opt.*, **12**, 3, 555–563, 1973.
- [67] J. A. Curcio and C. C. Petty, “The near infrared absorption spectrum of liquid water,” *J. Opt. Soc. Am.*, **41**, 5, 302–304, 1951.
- [68] G. M. Gibson, J. Leach, S. Keen, A. J. Wright, and M. J. Padgett, “Measuring the accuracy of particle position and force in optical tweezers using high-speed video microscopy,” *Opt. Express*, **16**, 19, 14 561–14 570, 2008.
- [69] F. Czerwinski, A. C. Richardson, and L. B. Oddershede, “Quantifying noise in optical tweezers by allan variance,” *Opt. Express*, **17**, 15, 13 255–13 269, 2009.
- [70] G. Sinclair, P. Jordan, J. Leach, M. Padgett, and J. Cooper, “Defining the trapping limits of holographical optical tweezers,” *J. Mod. Opt.*, **51**, 3, 409–414, 2004.

- [71] E. Theofanidou, L. Wilson, W. Hossack, and J. Arlt, “Spherical aberration correction for optical tweezers,” *Opt. Commun.*, **236**, 1-3, 145–150, 2004.
- [72] K. Wulff, D. Cole, R. Clark, R. Di Leonardo, J. Leach, J. Cooper, G. Gibson, and M. J. Padgett, “Aberration correction in holographic optical tweezers,” *Opt. Express*, **14**, 9, 4169–4174, 2006.
- [73] T. Cizmar, M. Mazilu, and K. Dholakia, “In situ wavefront correction and its application to micromanipulation,” *Nat. Photon.*, **4**, 6, 388–394, 2010.
- [74] R. W. Bowman, A. J. Wright, and M. J. Padgett, “An SLM-based Shack–Hartmann wavefront sensor for aberration correction in optical tweezers,” *J. Optics*, **12**, 12, 124004, 2010.
- [75] P. J. Rodrigo, L. Gammelgaard, P. Bøggild, I. Perch-Nielsen, and J. Glückstad, “Actuation of microfabricated tools using multiple GPC-based counterpropagating-beam traps,” *Opt. Express*, **13**, 18, 6899–6904, 2005.
- [76] P. Rodrigo, V. Daria, and J. Glückstad, “Four-dimensional optical manipulation of colloidal particles,” *Appl. Phys. Lett.*, **86**, 7, 074103, 2005.
- [77] J. Guck, R. Ananthakrishnan, H. Mahmood, T. J. Moon, C. C. Cunningham, and J. Käs, “The optical stretcher: A novel laser tool to micromanipulate cells,” *Biophys. J.*, **81**, 2, 767–784, 2001.
- [78] J. Guck, S. Schinkinger, B. Lincoln, F. Wottawah, S. Ebert, M. Romeyke, D. Lenz, H. M. Erickson, R. Ananthakrishnan, D. Mitchell, J. Käs, S. Ulvick, and C. Bilby, “Optical deformability as an inherent cell marker for testing malignant transformation and metastatic competence,” *Biophys. J.*, **88**, 5, 3689–3698, 2005.

- [79] M. Pitzek, R. Steiger, G. Thalhammer, S. Bernet, and M. Ritsch-Marte, “Optical mirror trap with a large field of view,” *Opt. Express*, **17**, 22, 19 414–19 423, 2009.
- [80] S. Zwick, T. Haist, Y. Miyamoto, L. He, M. Warber, A. Hermerschmidt, and W. Osten, “Holographic twin traps,” *J. Opt. A*, **11**, 3, 034011, 2009.
- [81] S. Tauro, A. Bañas, D. Palima, and J. Glückstad, “Dynamic axial stabilization of counter-propagating beam-traps with feedback control,” *Opt. Express*, **18**, 17, 18 217–18 222, 2010.
- [82] R. W. Bowman, G. Thalhammer, A. Jesacher, G. Gibson, M. Ritsch-Marte, and M. J. Padgett, “Position clamping in a counterpropagating holographic optical trap,” *Opt. Express*, **19**, 10, 9915–9922, 2011.
- [83] L. Ghislain, N. Switz, and W. Webb, “Measurement of small forces using an optical trap,” *Rev. Sci. Instrum.*, **65**, 9, 2762–2768, 1994.
- [84] I. Peters, B. de Groot, J. Schins, C. Figdor, and J. Greve, “Three dimensional single-particle tracking with nanometer resolution,” *Rev. Sci. Instrum.*, **69**, 7, 2762–2766, 1998.
- [85] A. Rohrbach, C. Tischer, D. Neumayer, E. Florin, and E. Stelzer, “Trapping and tracking a local probe with a photonic force microscope,” *Rev. Sci. Instrum.*, **75**, 6, 2197–2210, 2004.
- [86] M. Atakhorrani, K. M. Addas, and C. F. Schmidt, “Twin optical traps for two-particle cross-correlation measurements: Eliminating cross-talk,” *Rev. Sci. Instrum.*, **79**, 4, 043103, 2008.
- [87] W. H. Guilford, J. A. Tournas, D. Dascalu, and D. S. Watson, “Creating multiple time-shared laser traps with simultaneous displacement detection using digital signal processing hardware,” *Anal. Biochem.*, **326**, 2, 153–166, 2004.

- [88] D. Ruh, B. Traenkle, and A. Rohrbach, “Fast parallel interferometric 3D tracking of numerous optically trapped particles and their hydrodynamic interaction,” *Opt. Express*, **19**, 22, 21 627–21 642, 2011.
- [89] M. Speidel, L. Friedrich, and A. Rohrbach, “Interferometric 3D tracking of several particles in a scanning laser focus.” *Opt. Express*, **17**, 2, 1003–1015, 2009.
- [90] K. Neuman and S. M. Block, “Optical trapping,” *Rev. Sci. Instrum.*, **75**, 9, 2787–2809, 2004.
- [91] W. Grange, S. Husale, H. Guntherodt, and M. Hegner, “Optical tweezers system measuring the change in light momentum flux,” *Rev. Sci. Instrum.*, **73**, 6, 2308–2316, 2002.
- [92] J. C. Crocker and D. G. Grier, “Methods of digital video microscopy for colloidal studies,” *J. Colloid. Interf. Sci.*, **179**, 1, 298–310, 1996.
- [93] S. J. Lee and S. Kim, “Advanced particle-based velocimetry techniques for microscale flows,” *Microfluid. Nanofluid.*, **6**, 5, 577–588, 2009.
- [94] M. Polin, D. G. Grier, and S. R. Quake, “Anomalous vibrational dispersion in holographically trapped colloidal arrays,” *Phys. Rev. Lett.*, **96**, 8, 088101, 2006.
- [95] A. Curran, A. M. Yao, G. Gibson, R. W. Bowman, J. Cooper, and M. J. Padgett, “Real time characterization of hydrodynamics in optically trapped networks of micro-particles,” *J. Biophotonics*, **3**, 4, 244–251, 2010.
- [96] O. Otto, C. Gutsche, F. Kremer, and U. F. Keyser, “Optical tweezers with 2.5 kHz bandwidth video detection for single-colloid electrophoresis,” *Rev. Sci. Instrum.*, **79**, 2, 023710, 2008.
- [97] O. Otto, F. Czerwinski, J. L. Gornall, G. Stober, L. B. Oddershede, R. Seidel, and U. F. Keyser, “Real-time particle tracking at 10,000 fps

- using optical fiber illumination,” *Opt. Express*, **18**, 22, 22 722–22 733, 2010.
- [98] C. D. Saunter, “Quantifying subpixel accuracy: An experimental method for measuring accuracy in image-correlation-based, single-particle tracking,” *Biophys. J.*, **98**, 8, 1566–1570, 2010.
- [99] Z. Zhang and C.-H. Menq, “Three-dimensional particle tracking with subnanometer resolution using off-focus images,” *Appl. Opt.*, **47**, 13, 2361–2370, 2008.
- [100] S.-H. Lee and D. G. Grier, “Holographic microscopy of holographically trapped three-dimensional structures,” *Opt. Express*, **15**, 4, 1505–1512, 2007.
- [101] F. C. Cheong, B. J. Krishnatreya, and D. G. Grier, “Strategies for three-dimensional particle tracking with holographic video microscopy,” *Opt. Express*, **18**, 13, 13 563–13 573, 2010.
- [102] J. S. Dam, I. R. Perch-Nielsen, D. Palima, and J. Glückstad, “Three-dimensional imaging in three-dimensional optical multi-beam micro-manipulation,” *Opt. Express*, **16**, 10, 7244–7250, 2008.
- [103] P. Langevin, “Sur la théorie du mouvement Brownien,” *C. R. Acad. Sci (Paris)*, **146**, 530–533, 1908.
- [104] D. S. Lemons and A. Gythiel, “Paul Langevin’s 1908 paper “On the theory of Brownian motion”,” *Am. J. Phys.*, **65**, 11, 1079–1081, 1997.
- [105] K. Berg-Sørensen and H. Flyvbjerg, “Power spectrum analysis for optical tweezers,” *Rev. Sci. Instrum.*, **75**, 3, 594–612, 2004.
- [106] A. Yao, M. Tassieri, M. Padgett, and J. Cooper, “Microrheology with optical tweezers,” *Lab Chip*, **9**, 17, 2568–2575, 2009.

- [107] I. Tolic-Norrelykke, E. Munteanu, G. Thon, L. B. Oddershede, and K. Berg-Sorensen, “Anomalous diffusion in living yeast cells,” *Phys. Rev. Lett.*, **93**, 7, 078102, 2004.
- [108] M. Tassieri, G. M. Gibson, R. M. L. Evans, A. M. Yao, R. Warren, M. J. Padgett, and J. M. Cooper, “Measuring storage and loss moduli using optical tweezers: Broadband microrheology,” *Phys. Rev. E*, **81**, 2, 026308, 2010.
- [109] D. Preece, R. Warren, R. M. L. Evans, G. M. Gibson, M. J. Padgett, J. M. Cooper, and M. Tassieri, “Optical tweezers: wideband microrheology,” *J. Optics*, **13**, 4, 044022, 2011.
- [110] A. Bishop, T. Nieminen, N. Heckenberg, and H. Rubinsztein-Dunlop, “Optical microrheology using rotating laser-trapped particles,” *Phys. Rev. Lett.*, **92**, 19, 198104, 2004.
- [111] T. T. Perkins, S. R. Quake, D. E. Smith, and S. Chu, “Relaxation of a single DNA molecule observed by optical microscopy,” *Science*, **264**, 5160, 822–826, 1994.
- [112] A. Pralle, E. Florin, E. Stelzer, and J. Hörber, “Local viscosity probed by photonic force microscopy,” *Appl. Phys. A*, **66**, 71–73, 1998.
- [113] D. Palima, A. R. Banas, G. Vizsnyiczai, L. Kelemen, P. Ormos, and J. Glückstad, “Wave-guided optical waveguides,” *Opt. Express*, **20**, 3, 2004–2014, 2012.
- [114] L. Ikin, D. M. Carberry, G. Gibson, M. Padgett, and M. J. Miles, “Assembly and force measurement with SPM-like probes in holographic optical tweezers,” *New J. Phys.*, **11**, 023012, 2009.
- [115] D. M. Carberry, S. H. Simpson, J. A. Grieve, Y. Wang, H. Schafer, M. Steinhart, R. W. Bowman, G. Gibson, M. J. Padgett, S. Hanna, and M. J. Miles, “Calibration of optically trapped nanotools,” *Nanotechnol.*, **21**, 17, 2010.

- [116] D. B. Phillips, D. M. Carberry, S. H. Simpson, H. Schaefer, M. Steinhart, R. W. Bowman, G. M. Gibson, M. J. Padgett, S. Hanna, and M. J. Miles, “Optimizing the optical trapping stiffness of holographically trapped microrods using high-speed video tracking,” *J. Optics*, **13**, 4, 044023, 2011.
- [117] D. B. Phillips, J. A. Grieve, S. N. Olof, S. J. Kocher, R. W. Bowman, M. J. Padgett, M. J. Miles, and D. M. Carberry, “Surface imaging using holographic optical tweezers,” *Nanotechnol.*, **22**, 285503, 2011.
- [118] D. B. Phillips, S. H. Simpson, J. A. Grieve, G. M. Gibson, R. W. Bowman, M. J. Padgett, M. J. Miles, and D. M. Carberry, “Position clamping of optically trapped microscopic non-spherical probes,” *Opt. Express*, **19**, 20 622–20 627, 2011.
- [119] S. H. Simpson and S. Hanna, “Thermal motion of a holographically trapped SPM-like probe,” *Nanotechnol.*, **20**, 39, 395710, 2009.
- [120] S. H. Simpson and S. Hanna, “First-order nonconservative motion of optically trapped nonspherical particles,” *Phys. Rev. E*, **82**, 3, 031141, 2010.
- [121] G. Sinclair, P. Jordan, J. Courtial, M. Padgett, J. Cooper, and Z. Laczik, “Assembly of 3-dimensional structures using programmable holographic optical tweezers,” *Opt. Express*, **12**, 33, 5475–5480, 2004.
- [122] E. Florin, J. Horber, and E. Stelzer, “High-resolution axial and lateral position sensing using two-photon excitation of fluorophores by a continuous-wave Nd:YAG laser,” *Appl. Phys. Lett.*, **69**, 4, 446–448, 1996.
- [123] K. Sasaki, M. Tsukima, and H. Masuhara, “Three-dimensional potential analysis of radiation pressure exerted on a single microparticle,” *Appl. Phys. Lett.*, **71**, 1, 37–39, 1997.

- [124] F. C. Cheong, B. Sun, R. Dreyfus, J. Amato-Grill, K. Xiao, L. Dixon, and D. G. Grier, “Flow visualization and flow cytometry with holographic video microscopy,” *Opt. Express*, **17**, 15, 13 071–13 079, 2009.
- [125] J. Radler and E. Sackmann, “On the measurement of weak repulsive and frictional colloidal forces by reflection interference contrast microscopy,” *Langmuir*, **8**, 3, 848–853, 1992.
- [126] S. A. Alexandrov, T. R. Hillman, T. Gutzler, and D. D. Sampson, “Synthetic aperture Fourier holographic optical microscopy,” *Phys. Rev. Lett.*, **97**, 16, 168102, 2006.
- [127] L. Cavallini, G. Bolognesi, and R. Di Leonardo, “Real-time digital holographic microscopy of multiple and arbitrarily oriented planes,” *Opt. Lett.*, **36**, 17, 3491–3493, 2011.
- [128] J. S. Dam, I. Perch-Nielsen, D. Palima, and J. Glückstad, “Multi-particle three-dimensional coordinate estimation in real-time optical manipulation,” *J. Europ. Opt. Soc. Rap. Public.*, **4**, 09045, 2009.
- [129] C. Pacoret, R. W. Bowman, G. Gibson, S. Haliyo, D. Carberry, A. Bergander, S. Regnier, and M. Padgett, “Touching the microworld with force-feedback optical tweezers,” *Opt. Express*, **17**, 12, 10 259–10 264, 2009.
- [130] C. Gosse and V. Croquette, “Magnetic tweezers: Micromanipulation and force measurement at the molecular level,” *Biophys. J.*, **82**, 6, 3314–3329, 2002.
- [131] A. Bowman and A. Azzalini, “Computational aspects of nonparametric smoothing with illustrations from the sm library,” *Comp. Stat. Data An.*, **42**, 4, 545–560, 2003.
- [132] W. Singer, S. Bernet, N. Hecker, and M. Ritsch-Marte, “Three-dimensional force calibration of optical tweezers,” *J. Mod. Opt.*, **47**, 14-15, 2921–2931, 2000.

- [133] M. Dienerowitz, G. Gibson, F. Dienerowitz, and M. J. Padgett, “Expanding the toolbox for nanoparticle trapping and spectroscopy with holographic optical tweezers,” *J. Optics*, **14**, 4, 045003, 2012.
- [134] S. R. P. Pavani and R. Piestun, “Three dimensional tracking of fluorescent microparticles using a photon-limited double-helix response system,” *Opt. Express*, **16**, 26, 22 048–22 057, 2008.
- [135] T. Asavei, T. A. Nieminen, N. R. Heckenberg, and H. Rubinsztein-Dunlop, “Fabrication of microstructures for optically driven micromachines using two-photon photopolymerization of UV curing resins,” *J. Opt. A*, **11**, 3, 034001, 2009.
- [136] M. Dienerowitz, G. M. Gibson, R. W. Bowman, and M. J. Padgett, “Holographic aberration correction: optimising the stiffness of an optical trap deep in the sample,” *Opt. Express*, **19**, 24 589–24 595, 2011.
- [137] C. Alpmann, R. W. Bowman, M. Woerdemann, M. J. Padgett, and C. Denz, “Mathieu beams as versatile light moulds for 3D micro particle assemblies,” *Opt. Express*, **18**, 25, 26 084–26 091, 2010.
- [138] K. D. Wulff, D. G. Cole, and R. L. Clark, “Servo control of an optical trap,” *Appl. Opt.*, **46**, 22, 4923–4931, 2007.
- [139] A. E. Wallin, H. Ojala, E. Haeggstrom, and R. Tuma, “Stiffer optical tweezers through real-time feedback control,” *Appl. Phys. Lett.*, **92**, 22, 224104, 2008.
- [140] G. Wuite, R. Davenport, A. Rappaport, and C. Bustamante, “An integrated laser trap/flow control video microscope for the study of single biomolecules,” *Biophys. J.*, **79**, 2, 1155–1167, 2000.
- [141] C. O. Mejean, A. W. Schaefer, E. A. Millman, P. Forscher, and E. R. Dufresne, “Multiplexed force measurements on live cells with holographic optical tweezers,” *Opt. Express*, **17**, 8, 6209–6217, 2009.

- [142] T. Li, S. Kheifets, and M. G. Raizen, “MilliKelvin cooling of an optically trapped microsphere in vacuum,” *Nat. Phys.*, **7**, 7, 527–530, 2011.
- [143] M. Reicherter, S. Zwick, T. Haist, C. Kohler, H. Tiziani, and W. Osten, “Fast digital hologram generation and adaptive force measurement in liquid-crystal-display-based holographic tweezers,” *Appl. Opt.*, **45**, 5, 888–896, 2006.
- [144] B. Platt and R. Shack, “History and principles of Shack–Hartmann wavefront sensing,” *J. Refractive Surgery*, **17**, 5, S573–S577, 2001.
- [145] M. J. Booth, M. Neil, R. Juskaitis, and T. Wilson, “Adaptive aberration correction in a confocal microscope,” *Proc. Natl. Acad. Sci. U. S. A.*, **99**, 9, 5788–5792, 2002.
- [146] E. Fernandez, I. Iglesias, and P. Artal, “Closed-loop adaptive optics in the human eye,” *Opt. Lett.*, **26**, 10, 746–748, 2001.
- [147] S. Chamot, C. Dainty, and S. Esposito, “Adaptive optics for ophthalmic applications using a pyramid wavefront sensor,” *Opt. Express*, **14**, 2, 518–526, 2006.
- [148] J. M. Girkin, S. Poland, and A. J. Wright, “Adaptive optics for deeper imaging of biological samples,” *Curr. Opin. Biotech.*, **20**, 1, 106–110, 2009.
- [149] P. Rodrigo, R. Eriksen, V. Daria, and J. Glückstad, “Shack–Hartmann multiple-beam optical tweezers,” *Opt. Express*, **11**, 3, 208–214, 2003.
- [150] I. M. Vellekoop and A. P. Mosk, “Focusing coherent light through opaque strongly scattering media,” *Opt. Lett.*, **32**, 16, 2309–2311, 2007.

- [151] A. Jesacher, A. Schwaighofer, S. Fürhapter, C. Maurer, S. Bernet, and M. Ritsch-Marte, “Wavefront correction of spatial light modulators using an optical vortex image,” *Opt. Express*, **15**, 5801–5808, 2007.
- [152] C. Lopez-Quesada, J. Andilla, and E. Martin-Badosa, “Correction of aberration in holographic optical tweezers using a Shack–Hartmann sensor,” *Appl. Opt.*, **48**, 6, 1084–1090, 2009.
- [153] <http://www.physics.gla.ac.uk/Optics/projects/tweezers/software/>
- [154] L. Seifert, J. Liesener, and H. Tiziani, “The adaptive Shack–Hartmann sensor,” *Opt. Commun.*, **216**, 313–319, 2002.
- [155] L. Seifert, H. Tiziani, and W. Osten, “Wavefront reconstruction with the adaptive Shack–Hartmann sensor.” *Opt. Commun.*, **245**, 255–269, 2005.
- [156] T. Haist, J. Hafner, M. Warber, and W. Osten, “Scene-based wavefront correction with spatial light modulators,” *Proc. SPIE*, **7064**, M640, 2008.
- [157] A. Jesacher, S. Furhapter, S. Bernet, and M. Ritsch-Marte, “Diffractive optical tweezers in the Fresnel regime,” *Opt. Express*, **12**, 10, 2243–2250, 2004.
- [158] X. Wang, B. Wang, J. Pouch, F. Miranda, J. Anderson, and P. Bos, “Performance evaluation of a liquid-crystal-on-silicon spatial light modulator,” *Opt. Eng.*, **43**, 11, 2769–2774, 2004.
- [159] E. Martin-Badosa, M. Montes-Usategui, A. Carnicer, J. Andilla, E. Pleguezuelos, and I. Juvells, “Design strategies for optimizing holographic optical tweezers set-ups,” *J. Opt. A*, **9**, 8, S267–S277, 2007.
- [160] D. G. Smith and J. E. Greivenkamp, “Generalized method for sorting Shack–Hartmann spot patterns using local similarity,” *Appl. Opt.*, **47**, 25, 4548–4554, 2008.

- [161] J. Kirk and A. Jones, “Phase-only complex-valued spatial filter,” *J. Opt. Soc. Am.*, **61**, 8, 1023–1028, 1971.
- [162] J. Leach, M. R. Dennis, J. Courtial, and M. Padgett, “Vortex knots in light,” *New J. Phys.*, **7**, 1, 55, 2005.
- [163] T. Cizmar, V. Kollarova, X. Tsampoula, F. Gunn-Moore, W. Sibbett, Z. Bouchal, and K. Dholakia, “Generation of multiple Bessel beams for a biophotonics workstation,” *Opt. Express*, **16**, 18, 14 024–14 035, 2008.
- [164] E. McLeod and C. B. Arnold, “Subwavelength direct-write nanopatterning using optically trapped microspheres,” *Nat. Nanotechnol.*, **3**, 413–417, 2008.
- [165] P. Galajda and P. Ormos, “Complex micromachines produced and driven by light,” *Appl. Phys. Lett.*, **78**, 2, 249–251, 2001.
- [166] T. Asavei, V. L. Y. Loke, T. A. Nieminen, N. R. Heckenberg, and H. Rubinsztein-Dunlop, “Optical paddle-wheel,” in *Proc. SPIE*, K. Dholakia and G. C. Spalding, Eds., **7400**, 1, 740020, 2009.
- [167] K. Dholakia and T. Cizmar, “Shaping the future of manipulation,” *Nat. Photon.*, **5**, 6, 335–342, 2011.
- [168] P. J. Rodrigo, L. Kelemen, D. Palima, C. A. Alonzo, P. Ormos, and J. Glückstad, “Optical microassembly platform for constructing reconfigurable microenvironments for biomedical studies,” *Opt. Express*, **17**, 8, 6578–6583, 2009.
- [169] A. Constable, J. Kim, J. Mervis, F. Zarinetchi, and M. Prentiss, “Demonstration of a fiberoptic light-force trap,” *Opt. Lett.*, **18**, 21, 1867–1869, 1993.
- [170] A. Jonášš, P. Zemánek, and E. Florin, “Single-beam trapping in front of reflective surfaces,” *Opt. Lett.*, **26**, 19, 1466–1468, 2001.

- [171] M. Woerdemann, K. Berghoff, and C. Denz, “Dynamic multiple-beam counter-propagating optical traps using optical phase-conjugation,” *Opt. Express*, **18**, 21, 22 348–22 357, 2010.
- [172] I. Perch-Nielsen, P. Rodrigo, and J. Glückstad, “Real-time interactive 3D manipulation of particles viewed in two orthogonal observation planes,” *Opt. Express*, **13**, 8, 2852–2857, 2005.
- [173] H. Sehgal, T. Aggarwal, and M. V. Salapaka, “High bandwidth force estimation for optical tweezers,” *Appl. Phys. Lett.*, **94**, 15, 153114, 2009.
- [174] G. Thalhammer, R. Steiger, M. Meinschad, M. Hill, S. Bernet, and M. Ritsch-Marte, “Combined acoustic and optical trapping,” *Biomed. Opt. Express*, **2**, 10, 2859–2870, 2011.
- [175] J. A. Grieve, A. Ulcinas, S. Subramanian, G. Gibson, M. Padgett, D. M. Carberry, and M. J. Miles, “Hands-on with optical tweezers: a multitouch interface for holographic optical trapping,” *Opt. Express*, **17**, 5, 3595–3602, 2009.
- [176] S. C. Chapin, V. Germain, and E. R. Dufresne, “Automated trapping, assembly, and sorting with holographic optical tweezers,” *Opt. Express*, **14**, 26, 13 095–13 100, 2006.
- [177] P. J. Rodrigo, L. Kelemen, C. A. Alonzo, I. R. Perch-Nielsen, J. S. Dam, P. Ormos, and J. Glückstad, “2D optical manipulation and assembly of shape complementary planar microstructures,” *Opt. Express*, **15**, 14, 9009–9014, 2007.
- [178] A. Berthoz, *The brain’s sense of movement*. Barnes & Noble, 2000.
- [179] G. Whyte, G. Gibson, J. Leach, M. Padgett, D. Robert, and M. Miles, “An optical trapped microhand for manipulating micron-sized objects,” *Opt. Express*, **14**, 25, 12 497–12 502, 2006.

- [180] E. van West, A. Yamamoto, and T. Higuchi, “The concept of ”haptic tweezer”, a non-contact object handling system using levitation techniques and haptics,” *Mechatronics*, **17**, 7, 345–356, 2007.
- [181] C. Basdogan, A. Kiraz, I. Bukusoglu, A. Varol, and S. Doğanay, “Haptic guidance for improved task performance in steering microparticles with optical tweezers,” *Opt. Express*, **15**, 18, 11 616–11 621, 2007.
- [182] I. Bukusoglu, C. Basdogan, A. Kiraz, and A. Kurt, “Haptic manipulation of microspheres using optical tweezers under the guidance of artificial force fields,” *Presence-Teleoperators and Virtual Environments*, **17**, 4, 344–364, 2008.
- [183] F. Arai, M. Ogawa, and T. Fukuda, “Indirect manipulation and bilateral control of the microbe by the laser manipulated microtools,” *Intelligent Robots and Systems, 2000. (IROS 2000). Proceedings. 2000 IEEE/RSJ International Conference on*, **1**, 665–670 vol.1, 2000.
- [184] K. Onda and F. Arai, “Multi-beam bilateral teleoperation of holographic optical tweezers,” *Opt. Express*, **20**, 4, 3633–3641, 2012.
- [185] A. Bolopion, B. Cagneau, D. Haliyo, and S. Régnier, “Analysis of stability and transparency for nanoscale force feedback in bilateral coupling,” *J. Micro Nano Mechatron.*, **4**, 4, 145–158, 2009.
- [186] C. Pacoret, A. Bergander, and S. Regnier, “Haptic feedback of piconewton interactions with optical tweezers,” in *Lecture Notes in Computer Science*, **6192**, 333–338, 2010.
- [187] S. Keen, J. Leach, G. Gibson, and M. Padgett, “Comparison of a high-speed camera and a quadrant detector for measuring displacements in optical tweezers,” *J. Opt. A*, **9**, 8, S264–S266, 2007.
- [188] G. Gibson, D. M. Carberry, G. Whyte, J. Leach, J. Courtial, J. C. Jackson, D. Robert, M. Miles, and M. Padgett, “Holographic assembly workstation for optical manipulation,” *J. Opt. A*, **10**, 4, 044009, 2008.

- [189] M. Friese, A. Truscott, H. Rubinsztein-Dunlop, and N. Heckenberg, “Three-dimensional imaging with optical tweezers,” *Appl. Opt.*, **38**, 31, 6597–6603, 1999.
- [190] J. Leach, H. Mushfique, S. Keen, R. Di Leonardo, G. Ruocco, J. M. Cooper, and M. J. Padgett, “Comparison of Faxen’s correction for a microsphere translating or rotating near a surface,” *Phys. Rev. E*, **79**, 2, 026301, 2009.
- [191] J. Israelachvili and H. Wennerstrom, “Role of hydration and water structure in biological and colloidal interactions,” *Nature*, **379**, 6562, 219–225, 1996.
- [192] T. Cail and M. Hochella, “Experimentally derived sticking efficiencies of microparticles using atomic force microscopy,” *Environ. Sci. Technol.*, **39**, 4, 1011–1017, 2005.
- [193] R. W. Bowman, G. Gibson, D. Carberry, L. Picco, M. Miles, and M. J. Padgett, “iTweezers: optical micromanipulation controlled by an Apple iPad,” *J. Optics*, **13**, 4, 044002, 2011.
- [194] S. Lamont, R. W. Bowman, M. Rath, J. Williamson, R. Murray-Smith, and M. J. Padgett, “Touching the micron: tactile interactions with an optical tweezer,” in *Mobile HCI*, in press, 2012.
- [195] R. D. Leonardo, S. Keen, J. Leach, C. D. Saunter, G. D. Love, G. Ruocco, and M. Padgett, “Eigenmodes of a hydrodynamically coupled micron-size multiple-particle ring,” *Phys. Rev. E*, **76**, 6, 061402, 2007.
- [196] Z. Ni, C. Pacoret, R. Benosman, S. Ieng, and S. Regnier, “Asynchronous event-based high speed vision for microparticle tracking,” *J. Microscopy*, **245**, 3, 236–244, 2012.
- [197] C. D. Saunter, M. D. Perng, G. D. Love, and R. A. Quinlan, “Stochastically determined directed movement explains the dominant small-scale

- mitochondrial movements within non-neuronal tissue culture cells,” *FEBS Letters*, **583**, 8, 1267–1273, 2009.
- [198] C. Maurer, A. Jesacher, S. Bernet, and M. Ritsch-Marte, “Phase contrast microscopy with full numerical aperture illumination,” *Opt. Express*, **16**, 24, 19 821–19 829, 2008.
- [199] V. R. Daria, C. Stricker, R. W. Bowman, S. Redman, and H.-A. Bachor, “Arbitrary multisite two-photon excitation in four dimensions,” *Appl. Phys. Lett.*, **95**, 9, 093701, 2009.
- [200] P. Marsh, D. Burns, and J. M. Girkin, “Practical implementation of adaptive optics in multiphoton microscopy,” *Opt. Express*, **11**, 10, 1123–1130, 2003.
- [201] <http://www.gla.ac.uk/businessandindustry/easyaccessip/>
- [202] Y. J. Jeong, T. W. Lim, Y. Son, D.-Y. Yang, H.-J. Kong, and K.-S. Lee, “Proportional enlargement of movement by using an optically driven multi-link system with an elastic joint,” *Opt. Express*, **18**, 13, 13 745–13 753, 2010.
- [203] D. Phillips, S. Simpson, J. Grieve, R. W. Bowman, G. Gibson, M. Padgett, J. Rarity, S. Hanna, M. Miles, and D. Carberry, “Force sensing with a shaped dielectric micro-tool,” *Europhys. Lett.*, **99**, 5, 58004, 2012.